Nuclear Science
NEA/NSC/R(2019)5
February 2020
www.oecd-nea.org

Coupled Neutronic/Thermal-Fluid Benchmark of the MHTGR-350 MW Core Design: Results for Phase I Exercise 1

BETTER POLICIES FOR BETTER LIVES

NUCLEAR ENERGY AGENCY

Nuclear Energy Agency

NEA/NSC/R(2019)5

Unclassified **English text only**

3 March 2020

NUCLEAR ENERGY AGENCY
NUCLEAR SCIENCE COMMITTEE

Coupled Neutronic/Thermal-Fluid Benchmark of the MHTGR-350 MW Core Design: Results for Phase I Exercise 1

This document is available as PDF only.

JT03458400

ORGANISATION FOR ECONOMIC CO-OPERATION AND DEVELOPMENT

The OECD is a unique forum where the governments of 36 democracies work together to address the economic, social and environmental challenges of globalisation. The OECD is also at the forefront of efforts to understand and to help governments respond to new developments and concerns, such as corporate governance, the information economy and the challenges of an ageing population. The Organisation provides a setting where governments can compare policy experiences, seek answers to common problems, identify good practice and work to co-ordinate domestic and international policies.

The OECD member countries are: Australia, Austria, Belgium, Canada, Chile, the Czech Republic, Denmark, Estonia, Finland, France, Germany, Greece, Hungary, Iceland, Ireland, Israel, Italy, Japan, Korea, Latvia, Lithuania, Luxembourg, Mexico, the Netherlands, New Zealand, Norway, Poland, Portugal, the Slovak Republic, Slovenia, Spain, Sweden, Switzerland, Turkey, the United Kingdom and the United States. The European Commission takes part in the work of the OECD.

OECD Publishing disseminates widely the results of the Organisation’s statistics gathering and research on economic, social and environmental issues, as well as the conventions, guidelines and standards agreed by its members.

NUCLEAR ENERGY AGENCY

The OECD Nuclear Energy Agency (NEA) was established on 1 February 1958. Current NEA membership consists of 33 countries: Argentina, Australia, Austria, Belgium, Canada, the Czech Republic, Denmark, Finland, France, Germany, Greece, Hungary, Iceland, Ireland, Italy, Japan, Korea, Luxembourg, Mexico, the Netherlands, Norway, Poland, Portugal, Romania, Russia, the Slovak Republic, Slovenia, Spain, Sweden, Switzerland, Turkey, the United Kingdom and the United States. The European Commission and the International Atomic Energy Agency also take part in the work of the Agency.

The mission of the NEA is:

- to assist its member countries in maintaining and further developing, through international co-operation, the scientific, technological and legal bases required for a safe, environmentally sound and economical use of nuclear energy for peaceful purposes;
- to provide authoritative assessments and to forge common understandings on key issues as input to government decisions on nuclear energy policy and to broader OECD analyses in areas such as energy and the sustainable development of low-carbon economies.

Specific areas of competence of the NEA include the safety and regulation of nuclear activities, radioactive waste management and decommissioning, radiological protection, nuclear science, economic and technical analyses of the nuclear fuel cycle, nuclear law and liability, and public information. The NEA Data Bank provides nuclear data and computer program services for participating countries.

Foreword

Under the auspices of the NEA Nuclear Science Committee (NSC), the Working Party on Scientific Issues of Reactor Systems (WPRS) has been established to study the physics of present and future nuclear power systems. The Generation IV International Forum, has highlighted helium-cooled very high temperature gas reactors as a key technology with the potential to improve the competiveness of nuclear energy. Developing tools and methods to support this technology is seen as a priority by the membership of the NEA.

Accurate modelling and simulation tools for neutronics calculations are a key element needed to design high temperature gas-cooled reactors. Uncertainties in modelling and simulation can have significant safety and economic implications.

This report presents the results from code-to-code comparisons for a prismatic modular high-temperature gas-cooled reactor 350-MW design for steady-state neutron transport calculations. Integral parameters as well as power and flux distributions are provided. Differences between solutions from diffusion and transport operators are analysed. Effects of control rod homogenisation between full block and one-sixth block are discussed.

Table of contents

List of figures

List of tables

List of abbreviations and acronyms

APD	Axial power distribution (power density)
CR	Control rod
EOEC	End of equilibrium cycle
FEM	Finite element method
GRS	Gesellschaft für Anlagen- und Reaktorsicherheit
HTR	High-temperature reactor
HZDR	Helmholtz-Zentrum Dresden-Rossendorf
INL	Idaho National Laboratory (United States)
KAERI	Korea Atomic Energy Research Institute
MG	Multi-group
MHTGR	Modular high-temperature gas-cooled reactor
NEA	Nuclear Energy Agency
NEM	Nodal expansion method
PBMR	Pebble-bed modular reactor
PCM	Per cent mille (1/1000 of a per cent of the reactivity)
PMR	Prismatic modular reactor
RPD	Radial power distribution (power density)
RSD	Relative standard deviation
SD	Standard deviation
SNU	Seoul National University (Korea)
SPN	Simplified spherical harmonics
UMICH	University of Michigan (United States)
UNIST	Ulsan National Institute of Science and Technology (Korea)

1. Introduction

The prismatic modular reactor (PMR) is one of several high-temperature reactor (HTR) design concepts that have existed for decades. Several prismatic units have operated in the world (Dragon, Fort Saint Vrain and Peach Bottom) and one unit is still in operation – the High Temperature Test Reactor (HTTR) – in Japan. The deterministic neutronics, thermal fluids, and transient analysis tools and methods available to design and analyse PMRs have, in many cases, lagged behind the state of the art compared to other reactor technologies. This delay is driving the testing of existing methods for high-temperature gas-cooled reactors, as well as the development of more accurate and efficient tools to analyse the neutronics and thermal-fluid behaviour for the design and safety evaluations of the PMR. In addition to the development of new methods, the exercise includes the definition of an appropriate benchmark to perform code comparisons of such new methods.

Benchmark exercises provide some of the best avenues for better understanding current analysis tools. A very good example was the pebble-bed modular reactor (PBMR) coupled neutronics/thermal hydraulics transient benchmark for the PBMR-400 core design 0, which served as the foundation for this report. The purpose of this exercise is to identify significant differences between neutronics models used in determining key integral parameters and between distributions in prismatic HTRs. An important issue in the prismatic neutronics HTR community is the treatment of control rods (CRs) in full core modelling and simulation. Two spatial homogenisations of the CRs are included in the present benchmark.

The reference design is based on the modular high-temperature gas-cooled reactor (MHTGR) 350-MW 0 core design developed in the 1980s at General Atomics. This annular core configuration was selected, along with the average power density of 5.9 MW/m^3, to achieve maximum power rating and still permit passive core heat removal while maintaining the silicon carbide temperature below ~1 600°C during a conduction cool-down event.

The benchmark specification employs a simplified model of the reactor design. The axial and radial core layouts of this simplified model are presented in Figures 1 and 2. The active core consists of hexagonal graphite fuel elements containing blind holes for fuel compacts and full-length channels for helium coolant flow. The fuel elements are stacked to form columns (10 fuel elements per column) that rest on support structures. The active core columns form a three-row annulus with columns of hexagonal graphite reflector elements in the inner and outer regions. Thirty reflector columns contain channels for CRs, and 12 columns in the core also contain channels for the reserve shutdown material. In the active core region the standard blocks are red and the CR blocks are orange. The replaceable reflectors are shown in grey and the permanent reflectors in green. The yellow dashed lines depict the limit of the solution domain for the neutron transport problem.

Figure 1: Axial core layout (neutronic boundary shown in yellow)

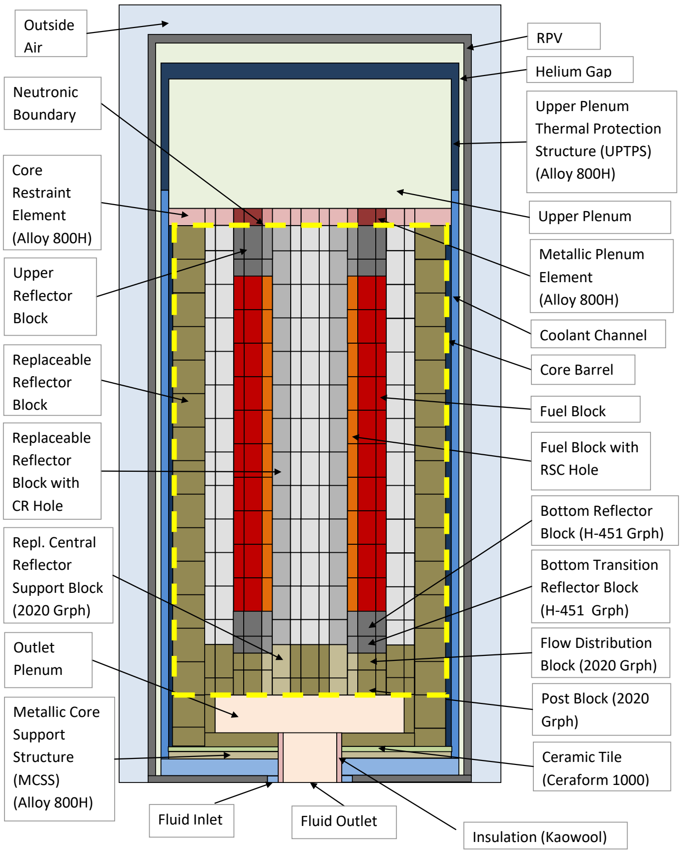

Source: OECD/NEA, 2020.

Figure 2: Radial core layout (neutronic boundary shown in yellow)

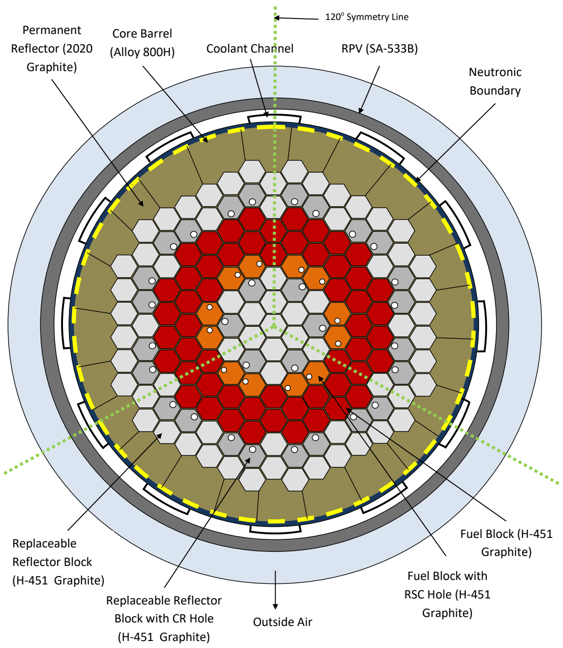

Source: OECD/NEA, 2020.

2. Description of Phase I Exercise 1

The benchmark employs a three-dimensional one-third symmetric representation of the core. The cross-sections for the model were developed with DRAGON-4 0 using fine group libraries based on the ENDF/B-VII.r0 data set. General Atomics provided the end of equilibrium cycle (EOEC) core number densities. The active core is comprised of 22 radial and 10 axial regions (physical blocks). There are separate cross-sections for each of the 220 active core regions, 11 reflector regions and 1 CR region. The power generated is assumed at 200 MeV per fission event.

It should be noted that, traditionally, equivalence parameters – either super homogenisation or discontinuity factors – are provided for this type of calculations in light water reactors to correct for the homogenisation error. The development of appropriate equivalence parameters for this core would entail the use of larger spatial domains or full core reference transport calculations. Since the cross-sections originate from single block lattice calculations, no attempt was made to preserve the reaction rates in the fuel blocks. It is well established that lattice fuel block calculations for HTRs with low-enriched uranium produce cross-sections that lead to larger errors in regions near the reflectors and, in this reactor design, a significant number of fuel blocks are located next to the reflectors. Instead, the preferred way to alleviate some of the error in the cross-sections is to allow better spectrum information to be transferred in the full core calculations through the use of a large number of coarse energy groups, for example with 26 groups in this case. The two spatial homogenisations of the CRs are shown in Figure 3. The first approach (Figure 3(b)) is to homogenise the CR entirely with the rest of the fuel block, whereas in the second approach (Figure 3(c)), the CR is homogenised over a one-sixth region of the block. The homogenisation of the CR is important, and ideally, it should be homogenised in isolation from fuel to minimise errors in the computation of the absorption and fission reaction rates, especially for depletion calculations.

Figure 3: Homogenisation of the CR (homogenisation region with yellow highlight)

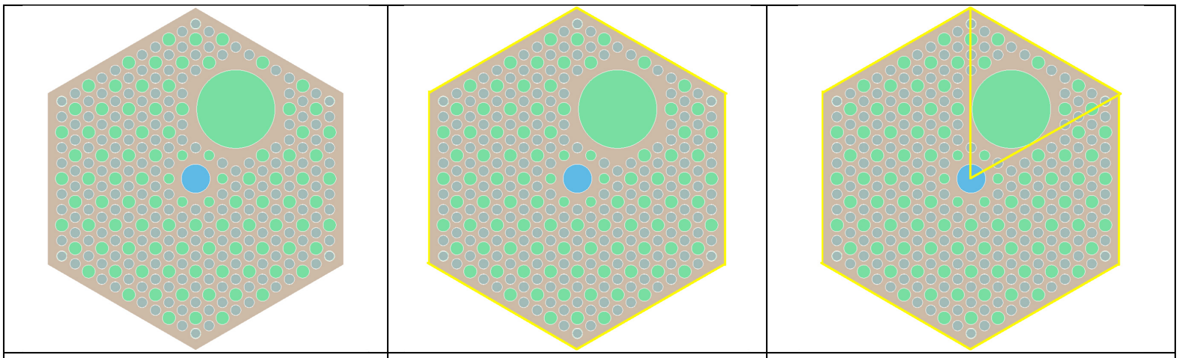

(a) Heterogeneous model (lattice)

(b) Full homogenisation model

(c) One-sixth homogenisation model

Source: OECD/NEA, 2020.

The fuel loading pattern for this core is included in Figure 4, which will aid in the understanding of the various power and flux distributions discussed in this report. Since the core number densities used in the cross-section preparation were obtained for an EOEC core, the locations labelled "A" (red) correspond to once-burned fuel, whereas twice-burned fuel is in "B" (blue) locations.

Figure 4: Loading pattern

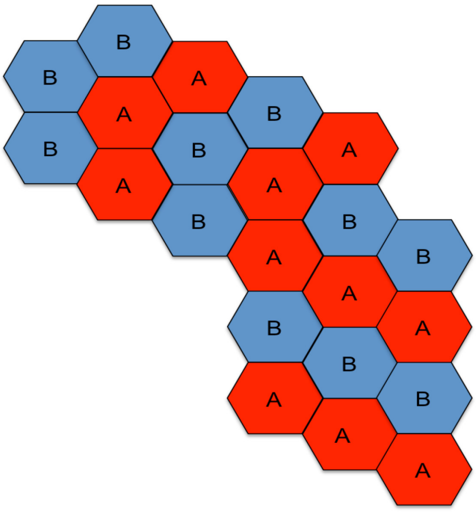

Source: OECD/NEA, 2020.

3. Participants and computer codes

Seven participants and solutions from nine computer codes were submitted for this portion of the benchmark. The list of participants and computer codes are shown in Table 1.

Table 1: List of participants and transport codes used

Organisation label	Organisation	Codes used in calculations	CR Homogenisation	Method	Country
INL	Idaho National Laboratory	INSTANT	Full, one-sixth	Hybrid finite element method (FEM) P_N transport	US
		Rattlesnake	Full, one-sixth	FEM diffusion	
UMICH	University of Michigan	PARCS	Full	Nodal expansion method (NEM) diffusion	US
KAERI	Korea Atomic Energy Research Institute	CAPP	Full, one-sixth	FEM diffusion	Korea
SNU	Seoul National University	McCARD	Full, one-sixth	Multi-group (MG) Monte Carlo transport	Korea
UNIST	Ulsan National Institute of Science and Technology	MCS	Full, one-sixth	MG Monte Carlo transport	Korea
HZDR	Helmholtz-Zentrum Dresden-Rossendorf	DYN3D	Full	Nodal simplified P_N transport	Germany
GRS	Gesellschaft für Anlagen- und Reaktorsicherheit	DIF3D	Full, one-sixth	Finite volume diffusion	Germany
		PARCS	Full	NEM diffusion	

Source: OECD/NEA, 2020.

Some of the comparisons in this work are between diffusion and transport solvers, where the transport solution is used as a reference. The results from the simplified spherical harmonics (SPN) method are not consistent with the rest of the transport solvers and are not included in the generation of an average transport reference solution. The reason for this is currently unknown, but the SPN solutions might suffer from modelling inconsistencies or convergence problems. The SPN equations are an asymptotic approximation to the transport equation and should be convergent for optically thick media as long as the problem is: 1) close to diffusive; or 2) locally one-dimensional 0. It is possible that the combination of large migration length, small active core regions and the two-dimensional radial nature of the core in this HTR design render the SPN assumption invalid. Therefore, the transport reference solution is solely based on the results from the INSTANT-P3, McCARD and MCS codes. The results labelled “diffusion” include the SPN values.

The NEM code DYN3D includes two solutions. In the HEXNEM1 approach the flux is expanded in two terms: 1) the specific solution of the inhomogeneous equation with orthogonal polynomial expansions; and 2) the general solution to the homogeneous equation with exponential expansions. The HEXNEM2 solver, in addition, includes the corner point balance exponential expansion terms. Another NEM code, PARCS, includes two different formulations. The TPEN method is formulated for hexagons, whereas the TRIPEN method is for triangles. They both include a corner point balance. It should be noted that the results from PARCS (TRIPEN) for the one-sixth homogenisation of the CR were not considered in the results since the calculation was determined to be an outlier.

4. Analysis method

The mean value (μ) was calculated for various parameters of interest. The associated standard deviation (SD) and the relative SD (RSD) of the calculated parameters were also determined according to the following formulas where N is the number of participants' solutions:

$$\mu = \frac{1}{N}\sum_{i=1}^{N} x_i$$

$$SD = \sqrt{\frac{1}{N}\sum_{i=1}^{N}(x_i - \mu)^2}$$

$$RSD = 100\frac{SD}{\mu}$$

Axial and radial averaging of solutions was computed using appropriate weights to take into account regions with different volumes. The weights were normalised to 1.

$$\mu = \sum_{i=1}^{I} w_i x_i$$

$$\sum_{i=1}^{I} w_i = 1$$

The RSD indicates the degree of consistency between the results provided by participants: a small RSD for a given parameter indicates consistency between the various codes and data used, whereas a large RSD indicates a poor agreement.

For this benchmark, it was assumed that a good agreement between participants' results has been obtained when the RSD is less than the maximum shown in Table 2. Conversely, if the quantities under comparison (e.g. eigenvalue power or flux) have an RSD larger than the ones shown in Table 2, it was considered to indicate a poor agreement between participants' results. It is noted that a low RSD does not mean that all the participants calculated the correct value; rather that they calculated a similar value. A "reference" result was not calculated for this problem, instead the mean values are used as the comparison basis. The statistical limitations inherent in the determination of the mean and variance values for such a small data set are recognised.

Table 2: Maximum RSD for various parameters

Parameter	**Maximum RSD (%)**
k_{eff}	0.1
CR worth	2.0
Axial offset	2.5
Axially averaged power distribution	2.0
Radially averaged power distribution	2.0

Source: OECD/NEA, 2020.

The definition of CR worth, $\Delta\rho_{CR}$, used in the benchmark is:

$$\Delta\rho_{CR} = \frac{k_{out} - k_{in}}{k_{out}k_{in}}$$

where,

k_{out}= eigenvalue with CR out

k_{in}= eigenvalue with CR in.

The axial offset is defined as:

$$AO = \frac{P_{top} - P_{bottom}}{P_{top} + P_{bottom}}$$

where,

P_{top} = total power produced in the top half of the core

P_{bottom}= total power produced in the bottom half of the core.

The cross-section data used in the calculations consists of 26 energy groups to better capture the reflector effects, which dominate the neutron physics in this core design. In the analysis of the data, the 26 groups are condensed into three energy ranges as shown in Table 3.

Table 3: Energy boundaries

Group name	Group number	Energy range (eV)	
		Upper	Lower
Fast	1-4	1.96E+07	9.47E+04
Epithermal	5-15	9.47E+04	4.93
Thermal	16-26	4.93	1.10E-04

Source: OECD/NEA, 2020.

5. Numerical results for the full control rod homogenisation

A comparison of key integral parameters from the various participants is shown in Figures 5-7 with the statistical mean value ±1 SD. The integral parameters include the fundamental mode eigenvalue, CR bank worth and axial power offset. Two distinct groupings can be observed in the data between the diffusion and transport solvers. The mean values and SDs are included in Table 4. Overall, there is good agreement in the fundamental mode eigenvalue among participants. The combined SD is less than 100 pcm, but the difference between the two equations being solved should be noted. The transport solutions show a smaller spread of values, with a SD of 6.4 pcm, whereas the diffusion solutions yield a SD of 42 pcm. The mean value for the transport solvers is 191 pcm higher than diffusion solvers. This can be attributed to differences that arise from the use of the diffusion coefficient versus the P_1 scattering matrix in the various solvers. This behaviour can be observed in the two results from the INSTANT solver. The cross-sections for the P_1 case were adjusted to yield diffusion-like solutions by modifying the total cross-section and the P_0 within group scattering. Conversely, the P_3 solution used the P_1 scattering matrix and produces a solution consistent with the MG Monte Carlo codes.

The calculations of the CR bank worth display a similar clustering for the transport versus diffusion solvers. The transport solvers compute a worth that is 28 pcm higher than diffusion solvers. The RSD for the transport and diffusion solvers are both below 0.4%, but when the statistics are combined it leads to an RSD of 1.5%. There exists a lot more variability in the axial offset calculation. The diffusion solutions exhibit an RSD of 2.2%, whereas the transport solvers are within 1.5%. There appear to be a few outliers in the diffusion solution with axial offsets near 0.172 and the INSTANT-P3 calculation is 3% lower than the other transport solvers. The rest of the solvers are consistent near 0.165.

Figure 5: k_{eff} comparison — full

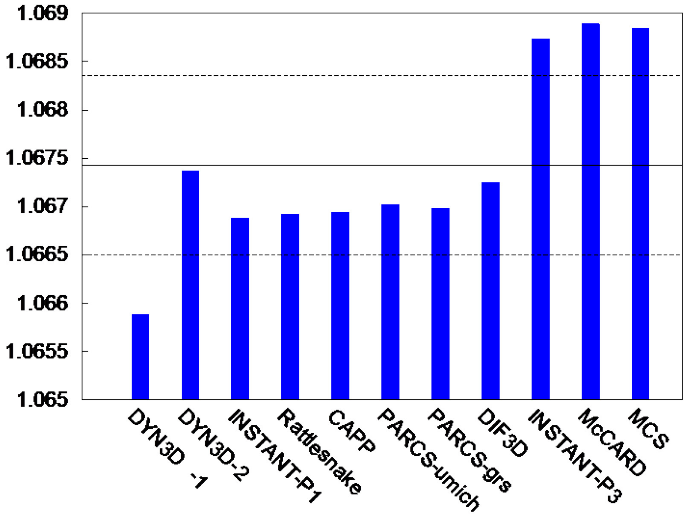

Source: OECD/NEA, 2020.

Figure 6: CR worth comparison [pcm] — full

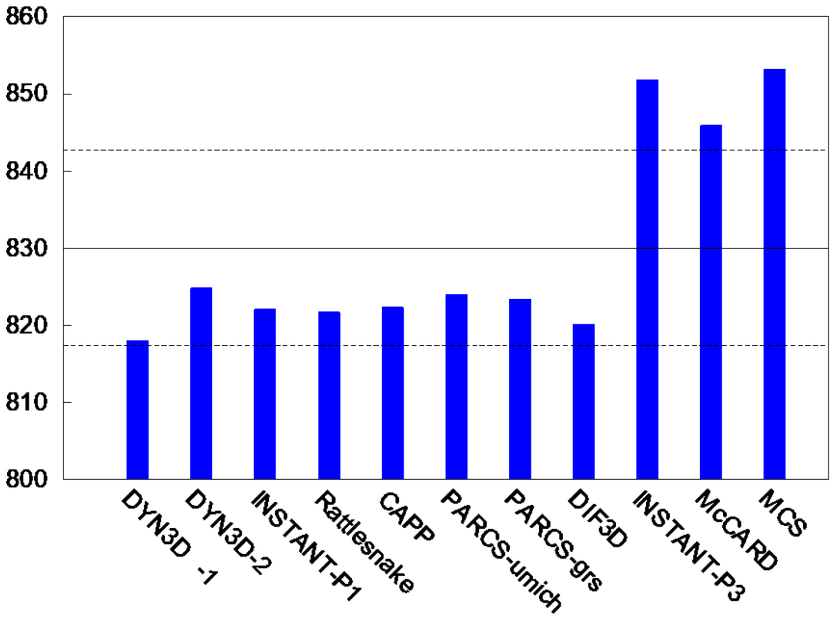

Source: OECD/NEA, 2020.

Figure 7. Axial offset comparison [%] — full

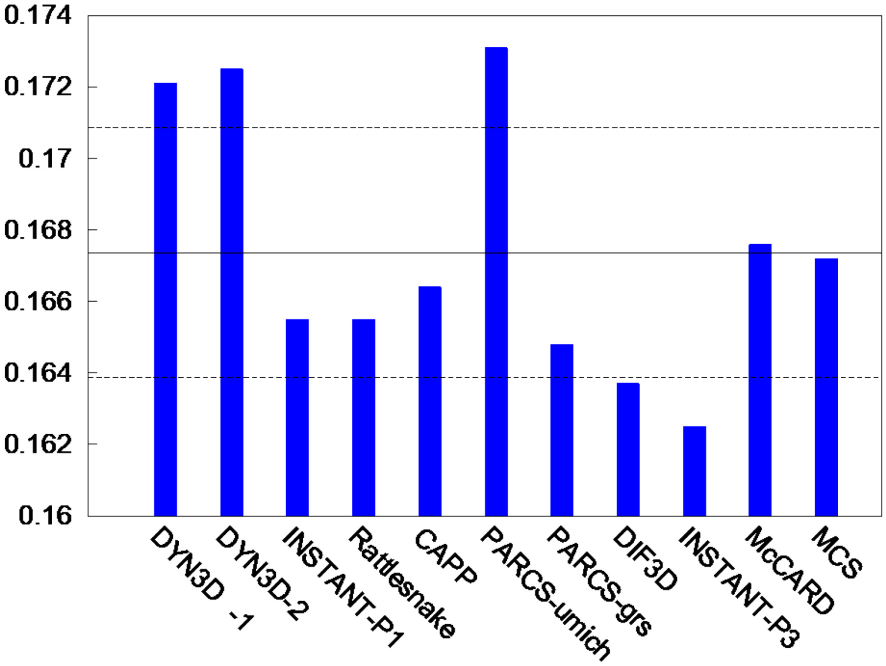

Source: OECD/NEA, 2020.

Table 4: Mean and SD for global parameters — full

Parameter	k_{eff}	CR Worth (pcm)	Axial offset
Mean (diffusion solvers)	1.06691	822.1	0.168
SD (diffusion solvers)	4.19E-4	2.05	3.66E-3
RSD (diffusion solvers)	3.93E-2	0.250	2.18
Mean (transport solvers)	1.06882	850.3	0.166
SD (transport solvers)	6.43E-5	3.20	2.34E-3
RSD (transport solvers)	6.02E-3	0.376	1.41
Mean (all solvers)	1.06743	829.8	0.167
SD (all solvers)	9.26E-4	12.8	3.49E-3
RSD (all solvers)	8.67E-2	1.54	2.08

Source: OECD/NEA, 2020.

The mean and RSD values of the radially averaged axial power distribution (APD) are shown in Figure 8. The top peaked distribution for this core is consistent with the axial offset results. The RSD is highest near the top and bottom reflectors with a maximum of 1.4% near the bottom. The solutions show good agreement through most of the active core region within 0.5%. The per cent difference among the results using the average APD from the transport solution as a reference is plotted in Annex A, Figure A.1. These results show that the diffusion solutions tend to under-predict the power near the axial fuel-reflector interface. The transport solutions remain within 1.0% of the mean value, but the diffusion solutions have a lot more variability. This can arise from discrepancies in the modelling, solution method, but it can also stem from poor convergence of the solution. The diffusion solvers that rely on FEM discretisation (INSTANT-P1, Rattlesnake, and CAPP) display similar behaviour, whereas the other diffusion methods are more scattered.

The mean and RSD values of the axially averaged radial power distribution (RPD) are shown in Figure 9. Two main factors affect the shape of the power: 1) the loading pattern (Figure 4); and 2) the proximity to reflectors. As expected, once-burned locations near the reflectors exhibit the highest power densities. These locations also have the largest magnitude of the RSD, but are within 1.1% of the mean value. When compared to the transport solutions, the diffusion solvers tend to over-predict the power in the ring near the inner reflector region and under-predict the power in the outer ring by the replaceable reflector, as depicted in Annex A, Figure A.2. Complete power distributions for diffusion and transport solvers are provided in Annex A, Figure A.3 and Figure A.4. A maximum power density of 9.99 MW/m^3 occurs in the seventh axial level (5 m from the bottom of the active core) near the central reflectors for the diffusion solutions. The maximum power density value for the transport solvers is located in the same block with a value of 9.71 MW/m^3.

The radially averaged flux distribution and RSD for the fast, epithermal and thermal energy ranges are shown in Figure 10. The thermal flux in the active core for this EOEC MHTGR-350 is in the order of 4×10^{13} n/cm^2/sec and is three and six times larger in magnitude than the epithermal and fast fluxes, respectively. The flux shape tends to flatten as the neutron energy is decreased since large neutron migration lengths characterise this core and neutrons will spatially distribute in the lower energy groups. The RSD for the fast group is highest near the bottom reflector, which is consistent with the RSD in the power shape from Figure 8, since fast neutrons emerge directly from fission sites, even though the deviation is higher for the flux with a peak value near 2.4%. The epithermal flux includes two regions that have high deviation, the bottom of the core (2.0%) and the region near the power peak (1.8%). The thermal flux has the largest values of the RSD (2.55%) near the thermal peak, 5 to 6 m from the bottom of the active core.

The mean value and RSD of the axially averaged neutron flux distributions are included in Figure 11 through Figure 13. These values are axially averaged over the layers in the active core region only. The flux values shown contain the radial reflector regions. The fast flux magnitude in Figure 11 rapidly decreases, by a factor of 3 to 4, in the first reflector ring as fast neutrons from the active core encounter reflector regions. The magnitude drops further another order of magnitude on each subsequent reflector ring as one moves further away from the source of fast neutrons to the core boundary. The RSD for the fast flux remains within 2.5% of the mean in the active core region, but quickly increases for each subsequent reflector ring to ~6% and ~10% for the first two reflector rings. Larger uncertainties are observed in the permanent reflector with values near 20% and a maximum of 37%. This can be attributed to differences in methods and modelling. Diffusion tends to have a poor representation of the flux near a void boundary compared to transport. The variation in the diffusion (Annex A, Figure A.5) and transport (Annex A, Figure A.6) solutions are provided for comparison. There are significant differences in the diffusion solutions in the reflector regions, whereas the transport solvers show better agreement, except for a few points in the permanent reflector.

The epithermal flux distribution in Figure 12 has a similar shape to the fast flux but with a peak that is slightly broader (i.e. encompasses parts of the first ring of reflectors, after which it quickly diminishes). The RSD for epithermal fluxes remain within 2% of the mean in the active core region, but increases for each subsequent reflector ring to ~3.0% and ~8% for the first two reflector rings. In the permanent reflector the RSD values are near 12% and a maximum of almost 16.5%. The RSD values in the transport solutions remain moderately flat and increase in the permanent reflector region with a maximum of 10.74% (Annex A, Figure A.8). Conversely, the RSD values for the diffusion solutions (Annex A, Figure A.7) show better agreement in the active core region, but they disagree in the reactor regions with a maximum value of 18.15% in the permanent reflector.

Figure 8: Radially averaged APD — full

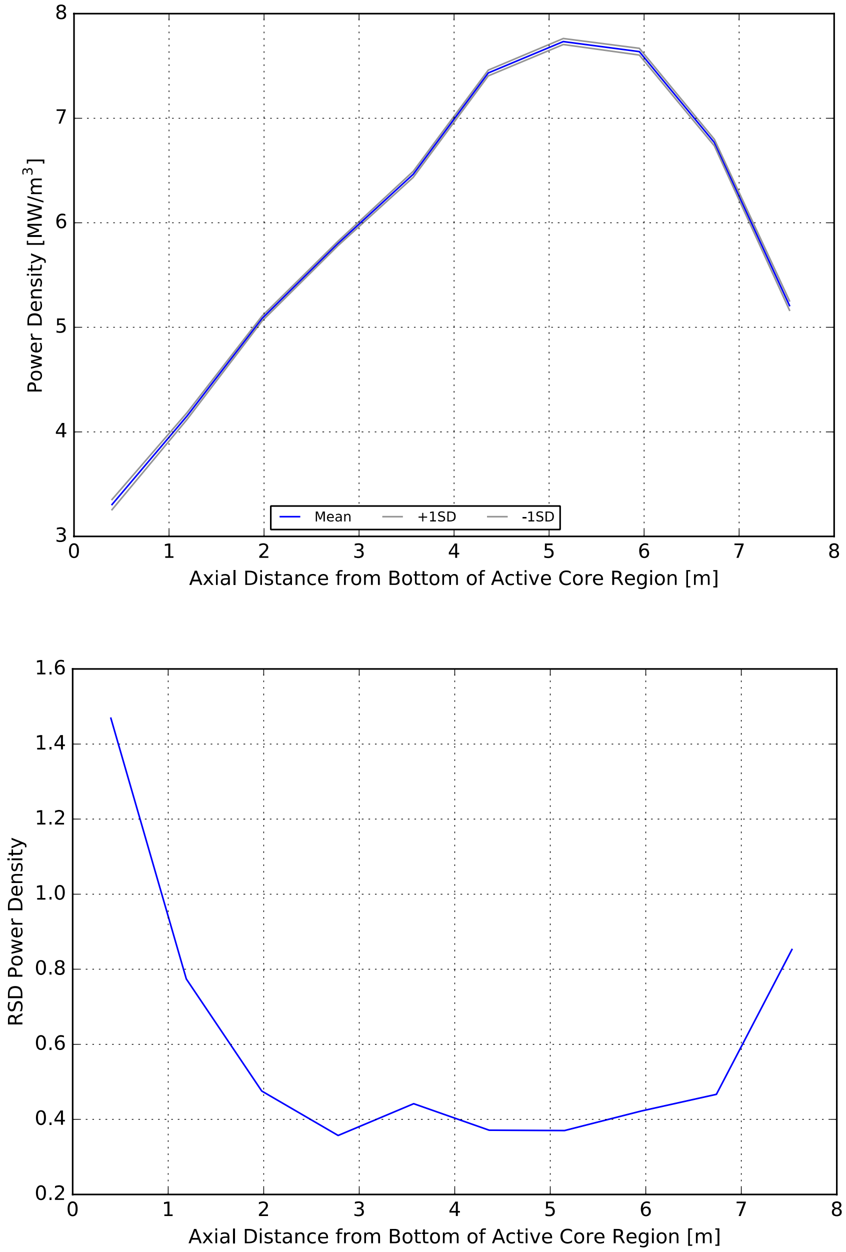

Source: OECD/NEA, 2020.

Figure 9: Mean value and RSD of the axially averaged RPD — full

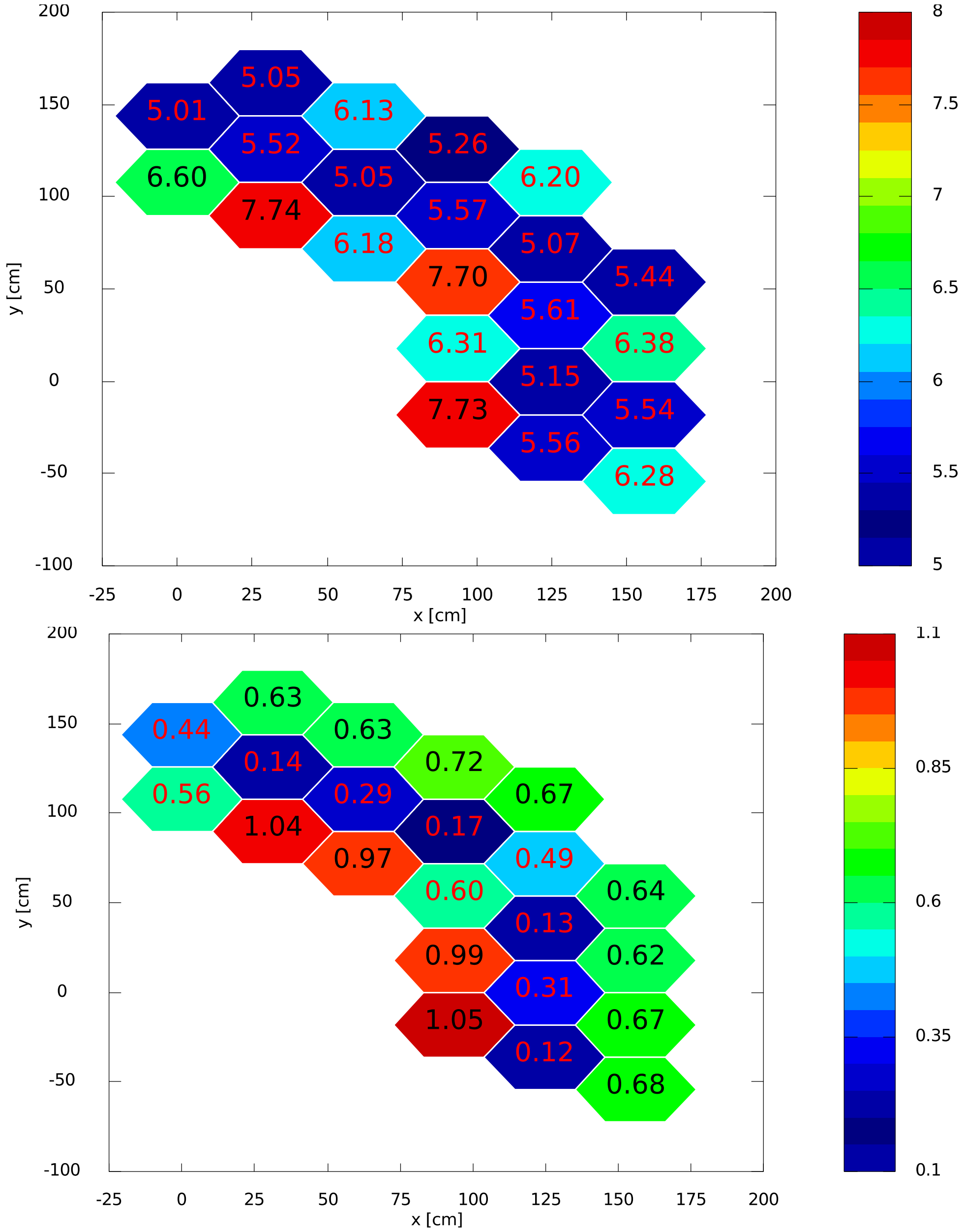

Source: OECD/NEA, 2020.

Finally, the thermal flux distribution (Figure 13) is characterised by a high peak in the central reflector region with a magnitude of 1.5 × 1014 n/cm2/sec. This magnitude decreases to ~4.0 × 1013 n/cm2/sec in the active core region, as thermal neutrons encounter fuel, and another, smaller peak in the replaceable reflector region. After this last region, the thermal flux remains relatively flat into the permanent reflector. The RSD for thermal fluxes exhibits a different behaviour than the other energy ranges, where the values remain within 3% of the mean in the active core region, with 4.3% in the central reflector, but they remain within 2.5% in the exterior replaceable reflector. In the permanent reflector the RSD values are near 4% with a maximum of 4.89%. The transport solutions show good agreement with a maximum RSD of 2.02% (Annex A,

Figure A.10), which occurs in the active core regions. The diffusion solutions, on the other hand, remain in good agreement within 2.7% in most regions, except for the permanent reflector with differences in the 4.6% range with a maximum of 5.42% (Annex A, Figure A.9).

Figure 10: Mean value and RSD of the radially averaged fast, epithermal, and thermal flux distribution — full

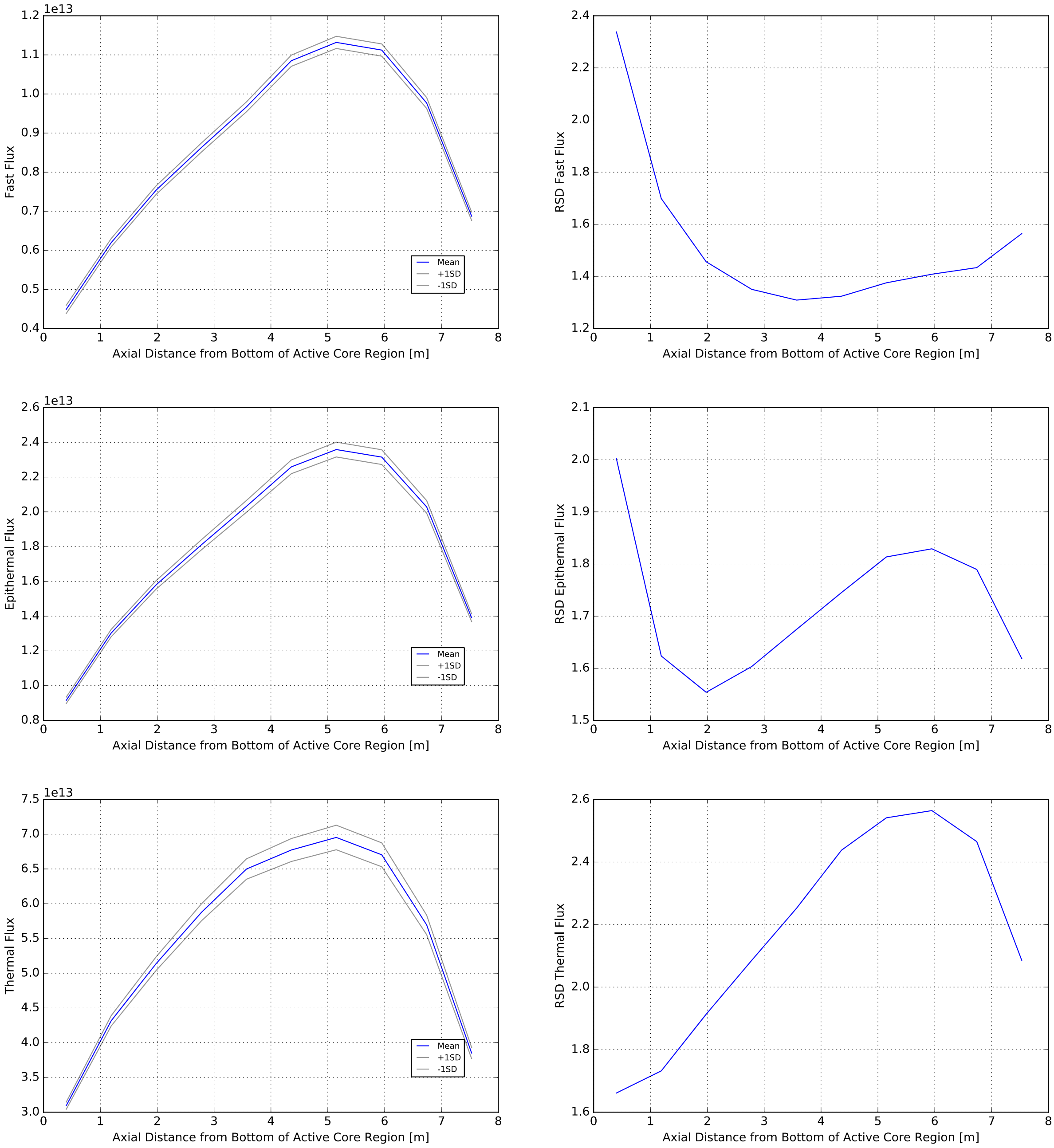

Source: OECD/NEA, 2020.

Figure 11: Mean value and RSD of the axially averaged (active core region) radial fast flux distribution from all solutions — full

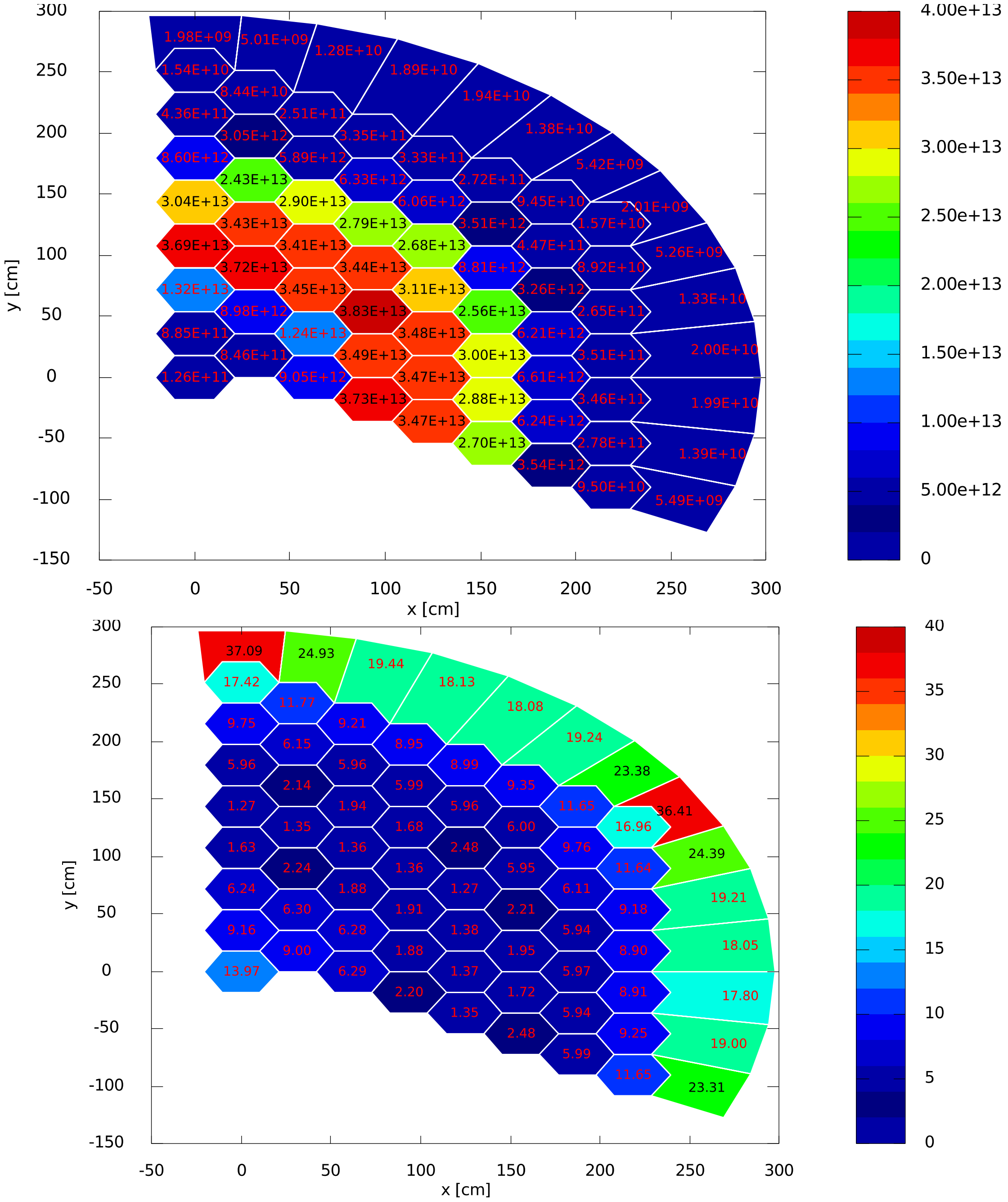

Source: OECD/NEA, 2020.

Figure 12: Mean value and RSD for the axially averaged (active core region) radial epithermal flux distribution from all solutions — full

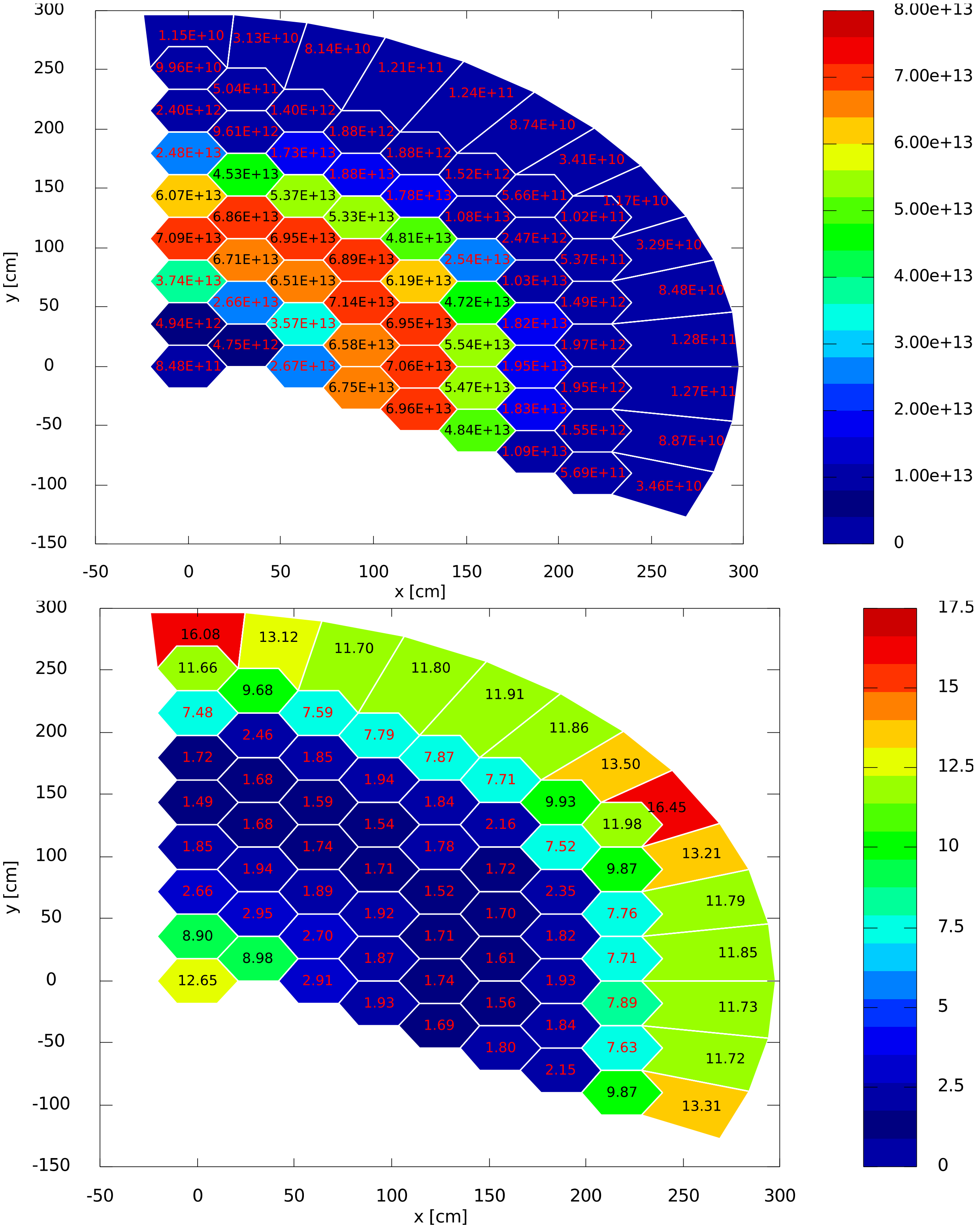

Source: OECD/NEA, 2020.

Figure 13: Mean value and RSD for the axially averaged (active core region) radial thermal flux distribution from all solutions — full

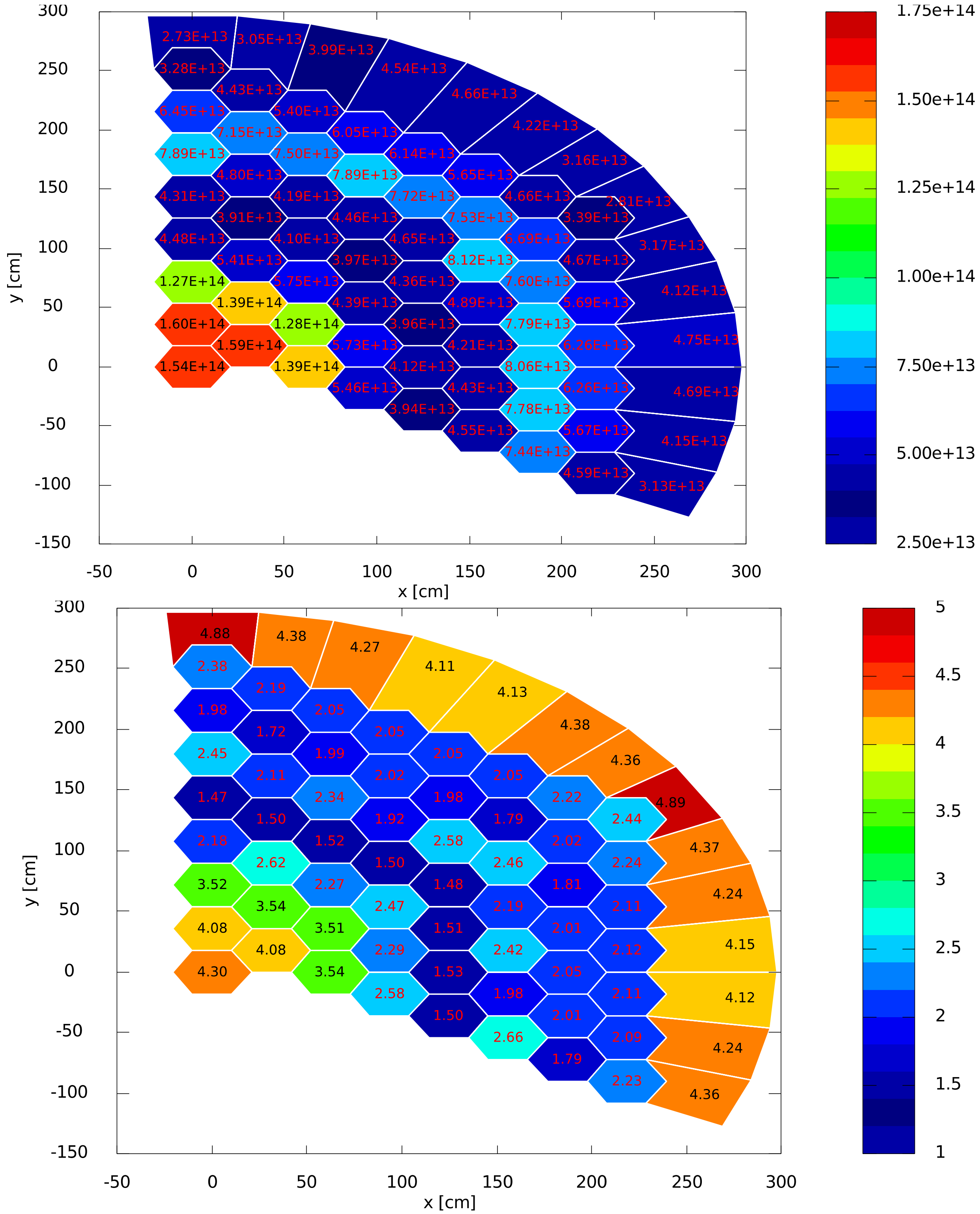

Source: OECD/NEA, 2020.

6. Numerical results for the one-sixth block control rod homogenisation

The quality of the solutions for the one-sixth block homogenisation needs to be examined before conducting a meaningful comparison to the full block homogenisation. Therefore, a similar analysis to that included in the previous section is performed herein, but with a reduced number of solutions, since only five participants submitted results with this homogenisation.

A comparison of key integral parameters from the various participants is shown in Figure 14 through Figure 16 with the statistical mean value ±1 SD. The statistics compiled from the submittals are included in Table 5. The two distinct groupings can be observed again in the eigenvalue data. The mean value for the transport solvers is 184 pcm higher than diffusion, very similar to the results with the fully homogenised CR. The SDs for transport and diffusion solutions are very similar, near 12 pcm. When these statistics are combined, the SD is still within 100 pcm of the mean value.

The mean value for the CR worth is 1 108 pcm. The difference in the CR worth predicted by transport and diffusion is within 30 pcm, which is similar to the 28 pcm observed in the previous section. The RSD for diffusion, at ~1%, is twice that of the transport solvers and leads to a combined value of 1.64%. This value is also consistent with the full homogenisation.

The axial offset is lower for this homogenisation with a mean of 0.148 and an RSD of 1.85%. This RSD value is similar to the value for the full homogenisation. There are disagreements in the transport solutions; specifically, the McCARD calculation appears to over-predict the axial offset compared to the other transport solvers by 5%.

Figure 14: Eigenvalue comparison — 1/6 block

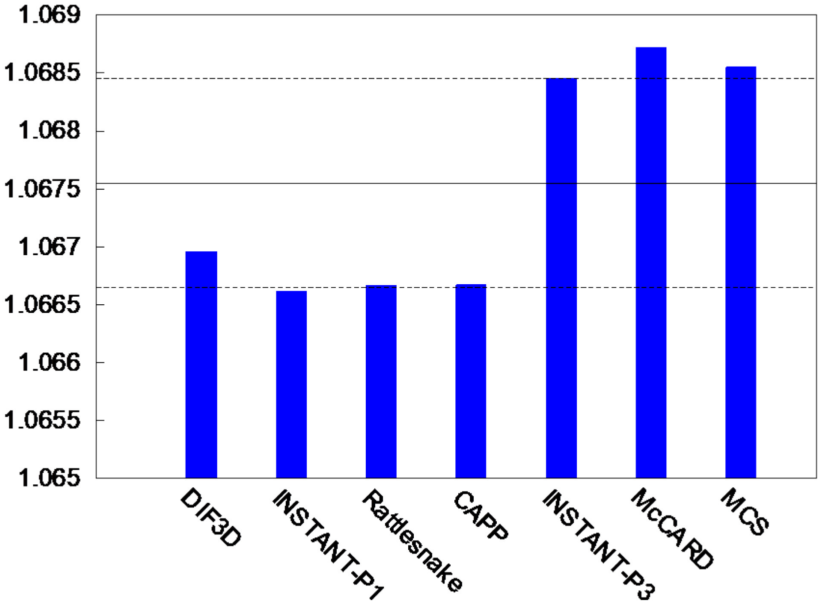

Source: OECD/NEA, 2020.

Figure 15: CR worth comparison [pcm] — 1/6 block

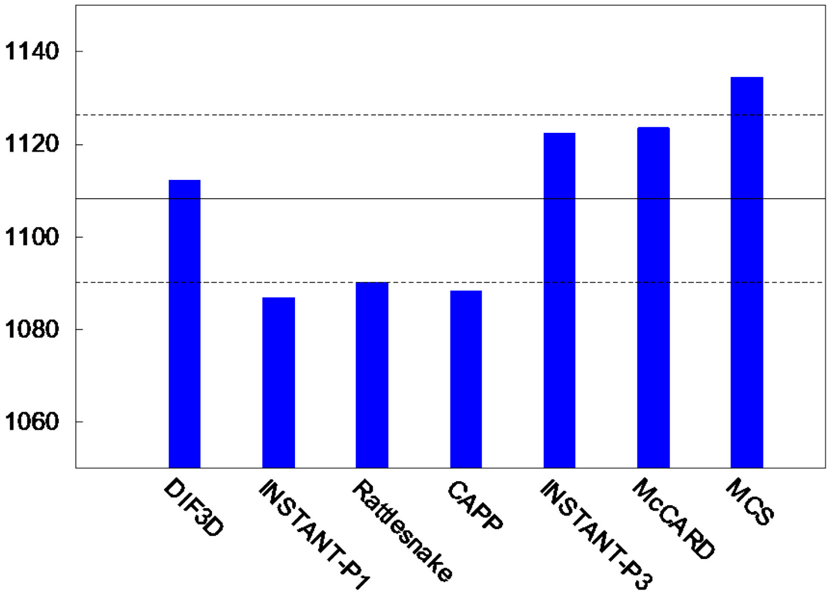

Source: OECD/NEA, 2020.

Figure 16: Axial offset comparison [%] — 1/6 block

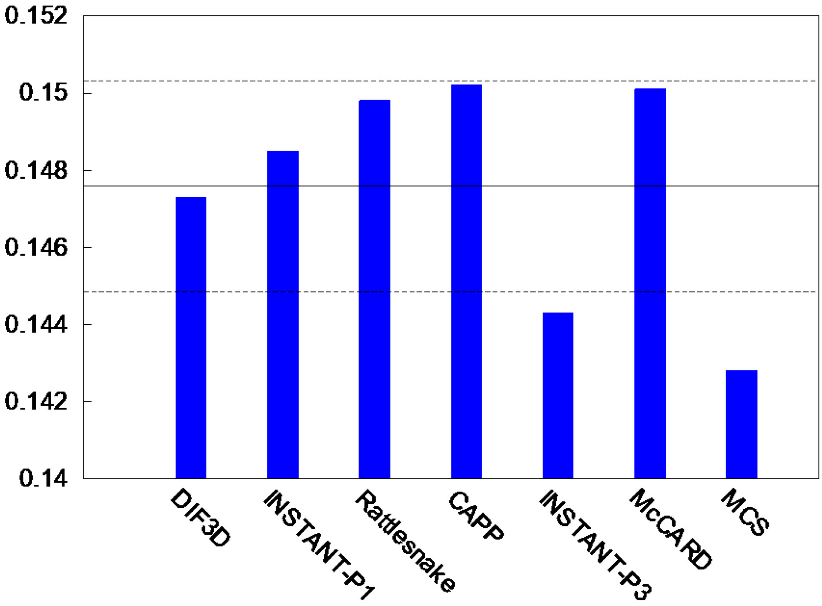

Source: OECD/NEA, 2020.

Table 5: Mean and SD for global parameters — 1/6 block

Parameter	**k_{eff}**	**CR worth (pcm)**	**Axial offset**
Mean (diffusion solvers)	1.06673	1 094.4	0.149
SD (diffusion solvers)	1.36E-4	10.3	1.13E-3
RSD (diffusion solvers)	1.27E-2	0.937	0.757
Mean (transport solvers)	1.06857	1 126.8	0.146
SD (transport solvers)	1.10E-4	5.49	3.14E-3
RSD (transport solvers)	1.03E-2	0.487	2.16
Mean (all solvers)	1.06752	1 108.3	0.148
SD (all solvers)	9.22E-4	18.2	2.73E-3
RSD (all solvers)	8.64E-2	1.64	1.85

Source: OECD/NEA, 2020.

The APD is included in Figure 17 and the RSD agrees well with that obtained for the full homogenisation of the CR. The comparisons between transport and diffusion solutions are also consistent with the other homogenisation and are shown in Annex B, Figure B.1.

Slightly higher disagreement, 0.1 to 0.2% higher, is observed for the RSD for the axially averaged RPD in Figure 18. The comparisons between transport and diffusion solutions in Annex B, Figure B.2, are consistent with the full homogenisation and show this small increase in the deviation. Power distributions at each axial level are provided for the average diffusion and transport solutions in Annex B, Figure B.3 and Figure B.4, respectively. These show higher values of the power in the upper core region.

The radially averaged flux distributions in Figure 19 show a very similar behaviour to those calculated in the previous section. Overall the axially averaged neutron flux distributions in Figures 20 through 22 show better agreement than with the full homogenisation of the CR except for the fast fluxes, which result in RSD values 0.5% higher in the active core region and 2-3% in the other regions. These are a direct result from high deviations in the diffusion solutions shown in Annex B, Figure B.5. The transport solutions in Annex B, Figure B.6, have a much better agreement. The epithermal flux results indicate improvements of the RSD in the reflector regions between 6 and 9% and the active core region remaining within 2.11%. These again can be attributed to the transport solutions. The diffusion and transport solutions and RSDs are included in Annex B, Figure B.7 and Figure B.8. Finally, the thermal flux RSD is the best obtained in the analysis and has values within 2.1% everywhere. The diffusion solutions are within 4.67% RSD (Annex B, Figure B.9), whereas the transport solutions are within 2.06% (Annex B, Figure B.10).

Besides the modest increase in the fast flux in some reflector regions one can conclude that comparisons of the full and one-sixth CR homogenisation can lead to useful conclusions, which is the topic discussed in the next section.

Figure 17: Radially averaged APD — 1/6 block

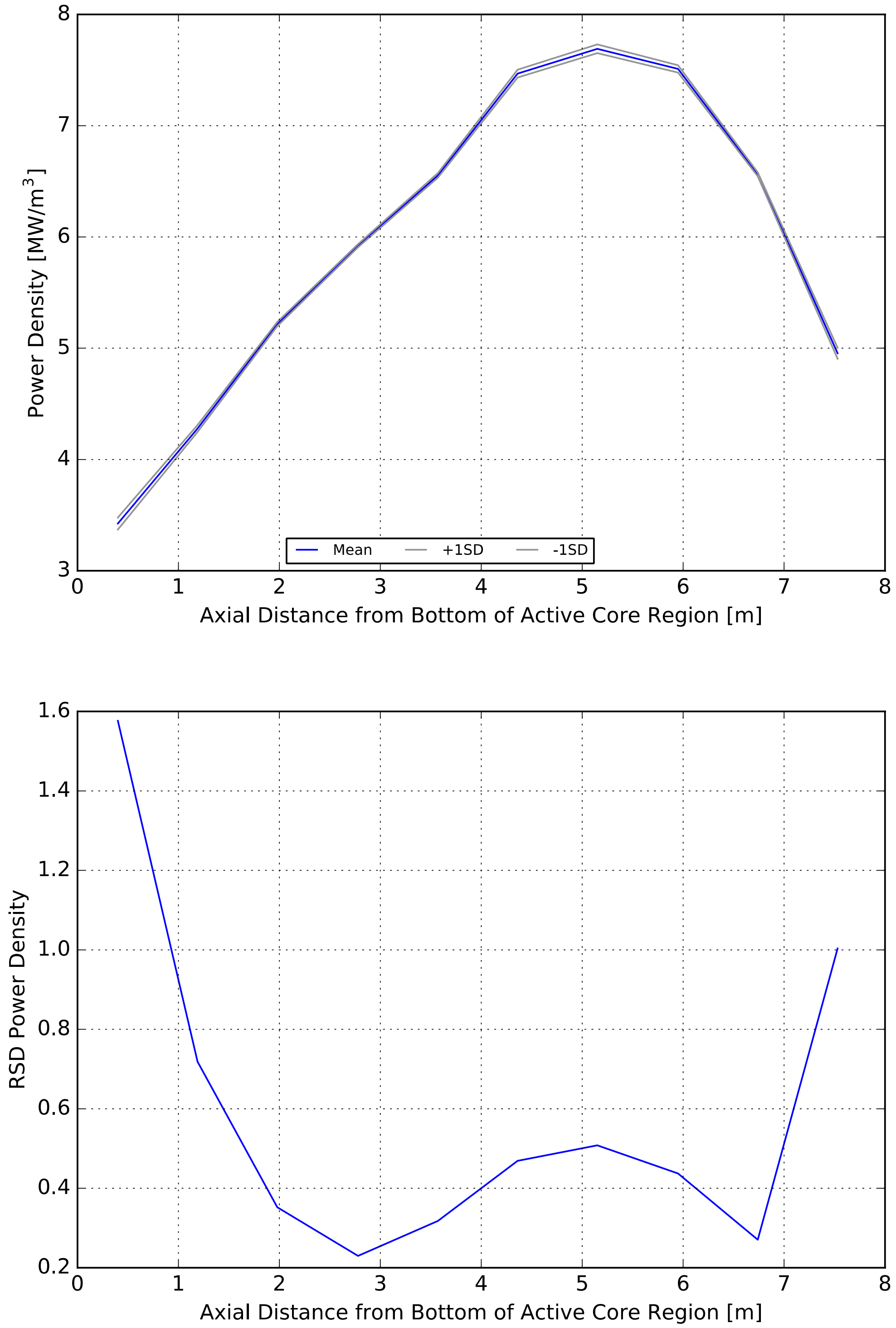

Source: OECD/NEA, 2020.

Figure 18: Mean value and RSD of the axially averaged RPD — 1/6 block

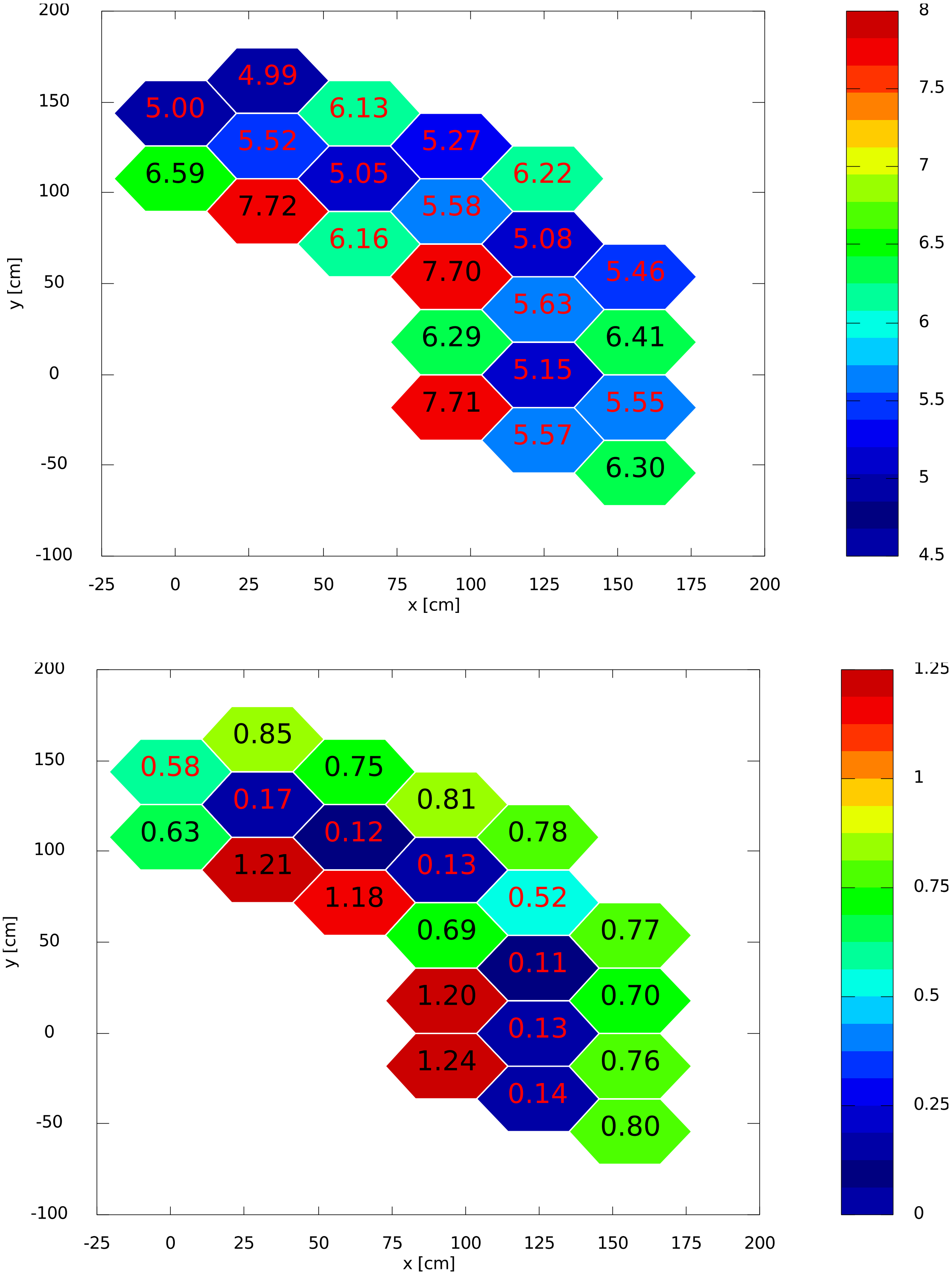

Source: OECD/NEA, 2020.

Figure 19: Mean value and RSD of the radially averaged fast, epithermal, and thermal flux distribution — 1/6 block

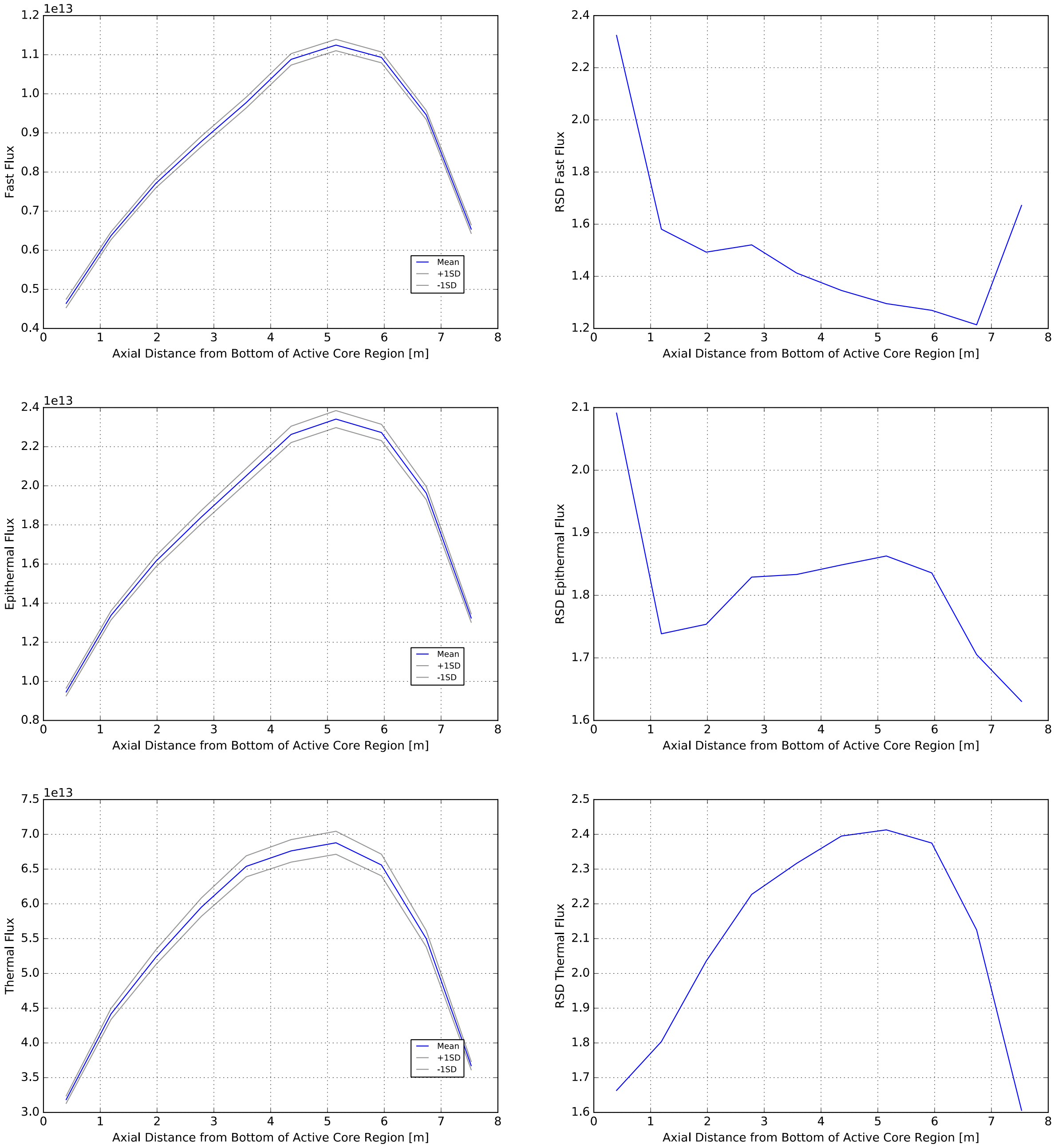

Source: OECD/NEA, 2020.

Figure 20: Mean value and RSD of the axially averaged (active core region) radial fast flux distribution from all solutions — 1/6 block

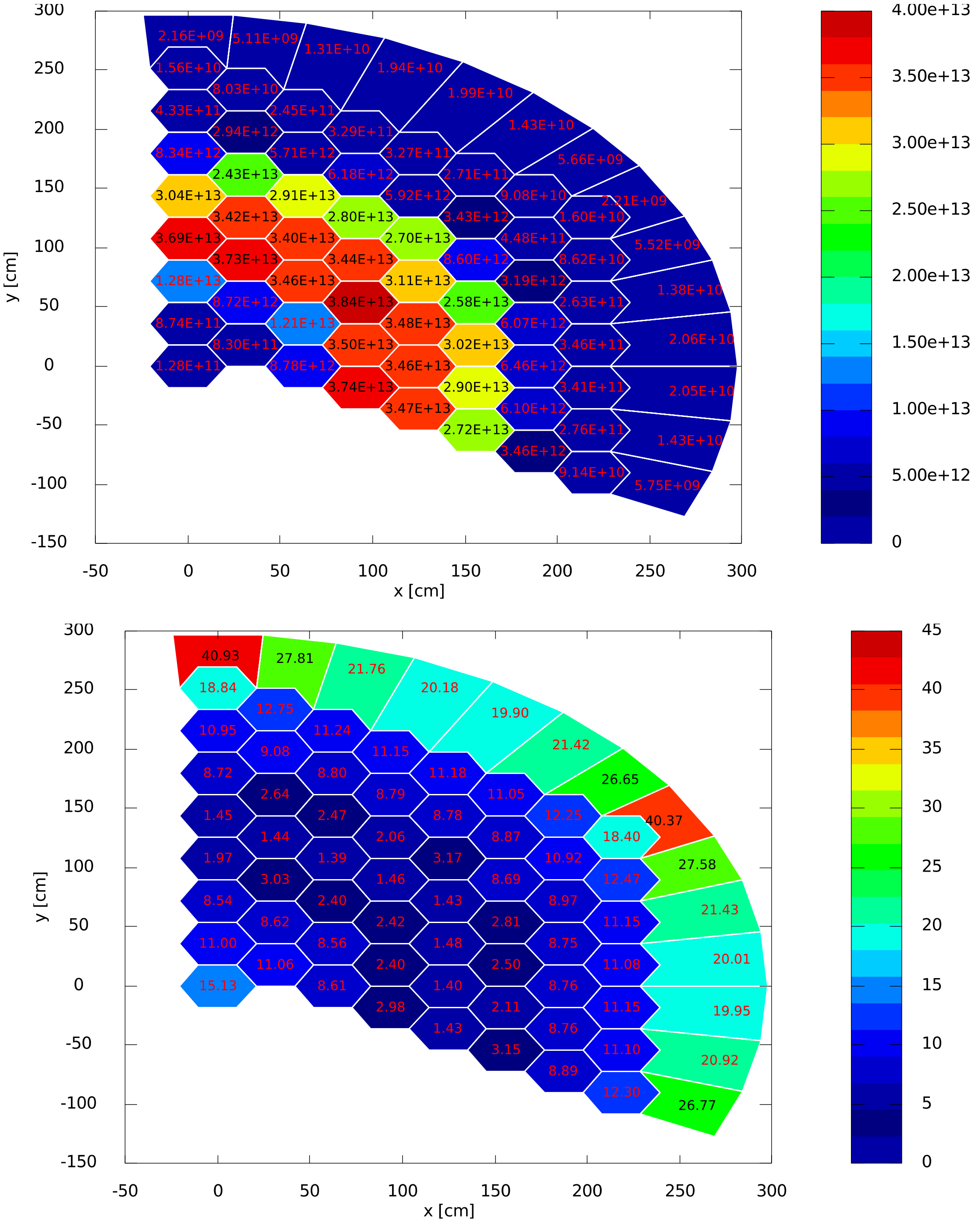

Source: OECD/NEA, 2020.

Figure 21: Mean value and RSD for the axially averaged (active core region) radial epithermal flux distribution from all solutions — 1/6 block

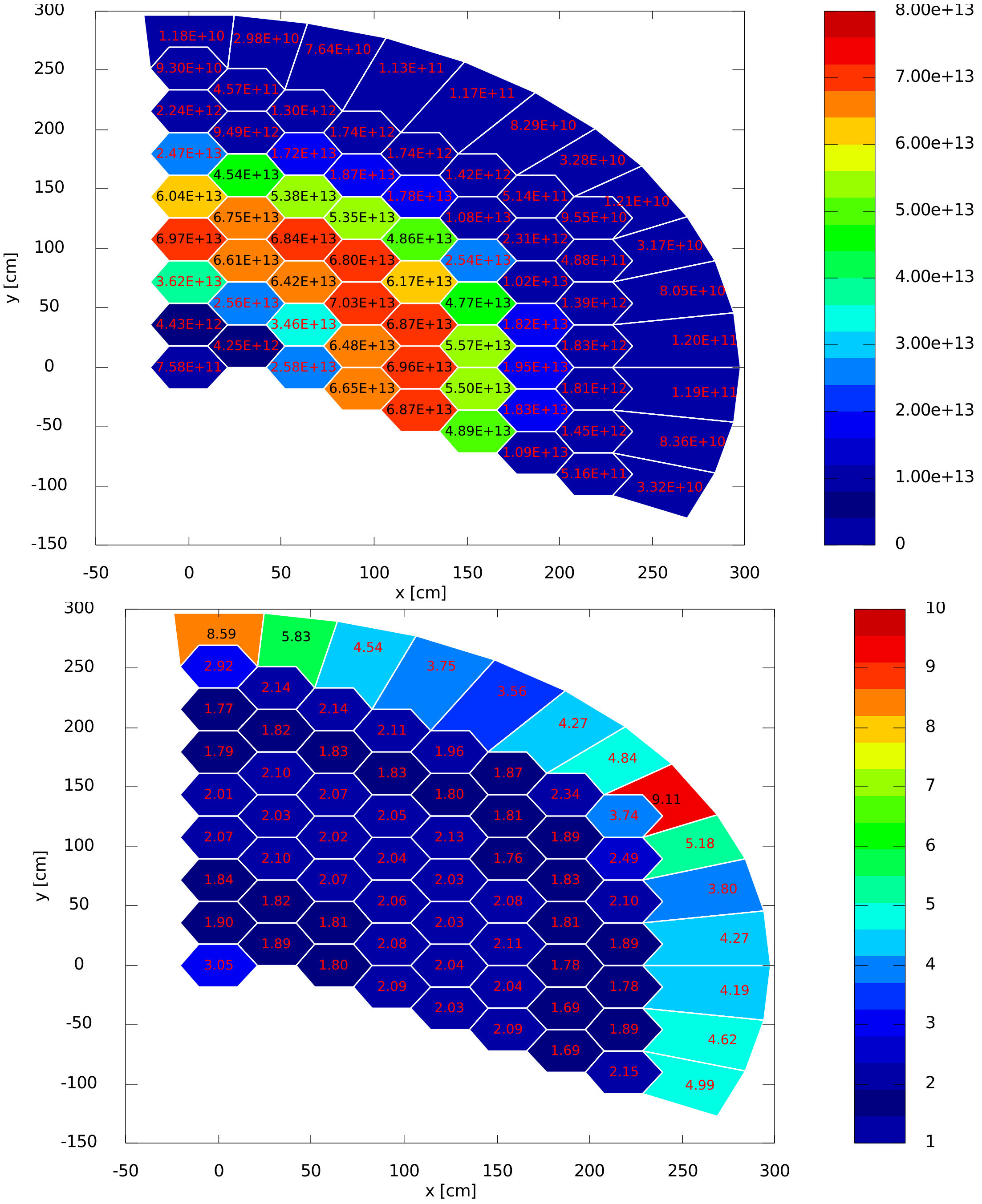

Source: OECD/NEA, 2020.

Figure 22: Mean value and RSD for the axially averaged (active core region) radial thermal flux distribution from all solutions — 1/6 block

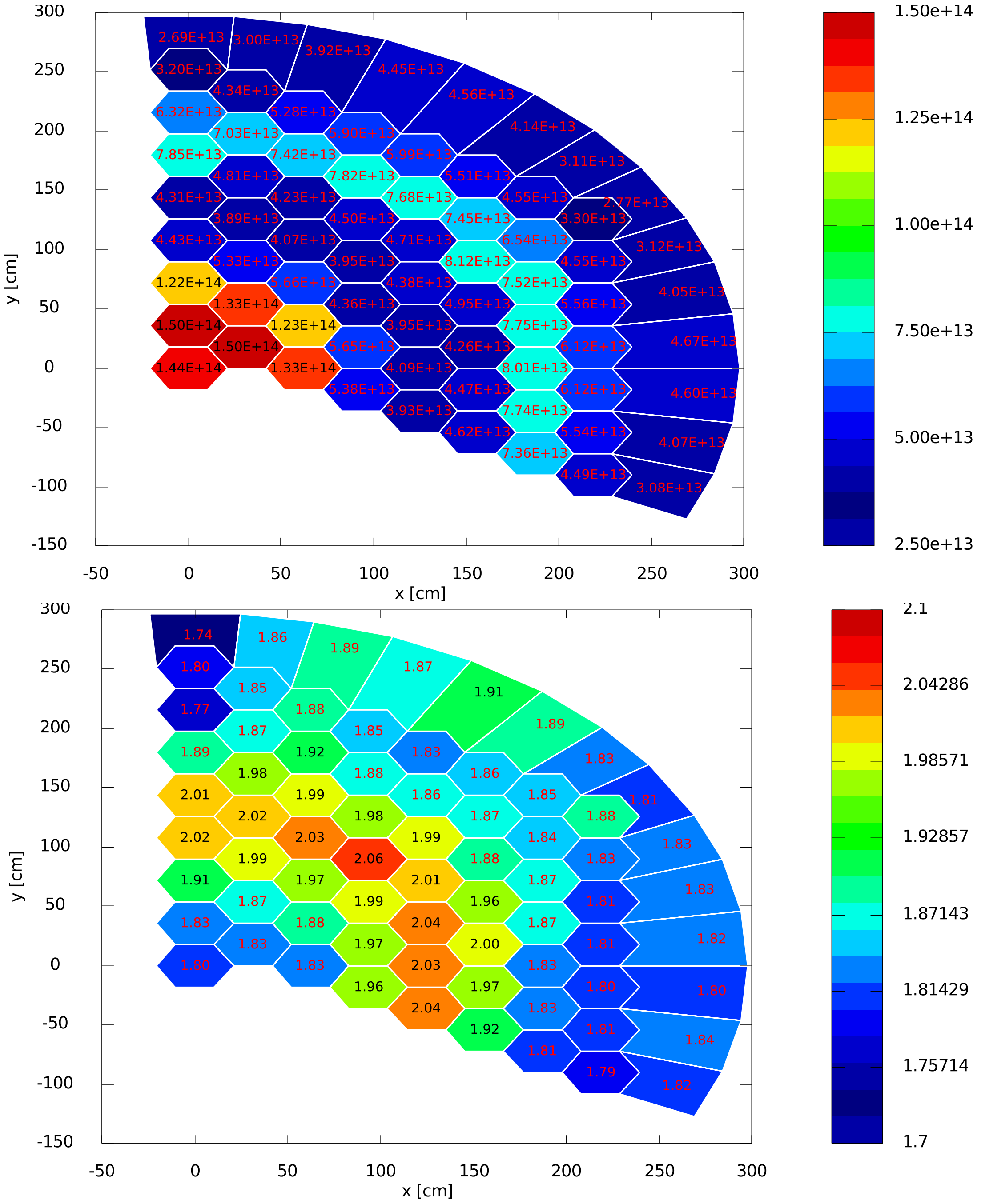

Source: OECD/NEA, 2020.

7. Comparison between the two control rod homogenisations

The eigenvalue calculation appears to be somewhat insensitive to the CR homogenisation with a difference of 25 pcm for the transport solvers and 18 pcm for diffusion. But this is mainly due to the fact that the control rods are shallowly inserted. The calculation of the CR worth shows a significant difference of 274 pcm. The worth of the rods is higher with the one-sixth homogenisation, which implies that the fully homogenised model under-predicts the absorption in the CR when fully inserted. It is important to consider again that no equivalence technique is used to preserve the reaction rates from the lattice physics calculations.

The value of the axial offset decreases by 12% with the one-sixth homogenisation, which is consistent with the conclusions from the CR worth calculation since the one-sixth block homogenised CR has larger effect on the top of the core, thus forcing more power to the bottom portion of the core.

The effect on the radially averaged power distribution can be observed in Figure 23. The full homogenisation produces more power on the top of the core with an over-prediction of 5% on the top layer and an under-prediction of 3% at the bottom of the active core. This can be significantly worse if the reactor is operated with deeply inserted CRs, which is the case in the MHTGR-350 design, where the CRs are slowly withdrawn through the core's equilibrium cycle.

Figure 23: CR homogenisation effect on the radially averaged APD

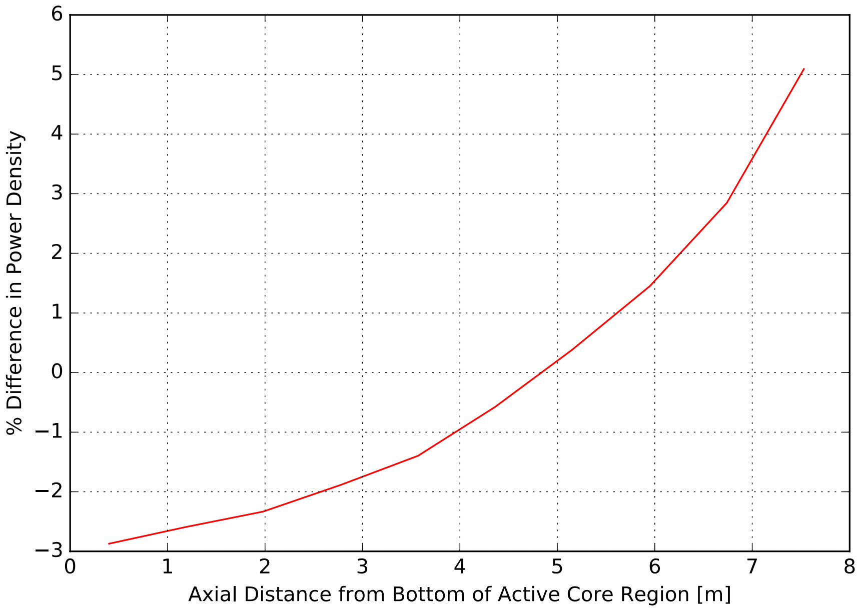

Source: OECD/NEA, 2020.

The axially averaged RPD in Figure 24 indicates an over-prediction in the power close to the CR of 1.39%. A few RPDs at various axial levels in the core are provided in Figure 25 to determine the impact of the homogenisation. The maximum per cent difference in the power distribution is 23.97% for the fuel block next to the CR (~7.5 m of the active core). The minimum value of -3.62% occurs at the bottom (0.4 m of the active core), but the position of the block could be affected by the difference in the power statistics between the two homogenisations. At the level just below the CR (z = 6.74 m) the per cent difference is approximately 5%, and at 5.95 m, the effect of the CR is negligible. This is corroborated in Figure 23 where the per cent relative difference is closer to zero.

Figure 24: CR homogenisation effect on the axially averaged RPD (per cent difference with one-sixth as reference)

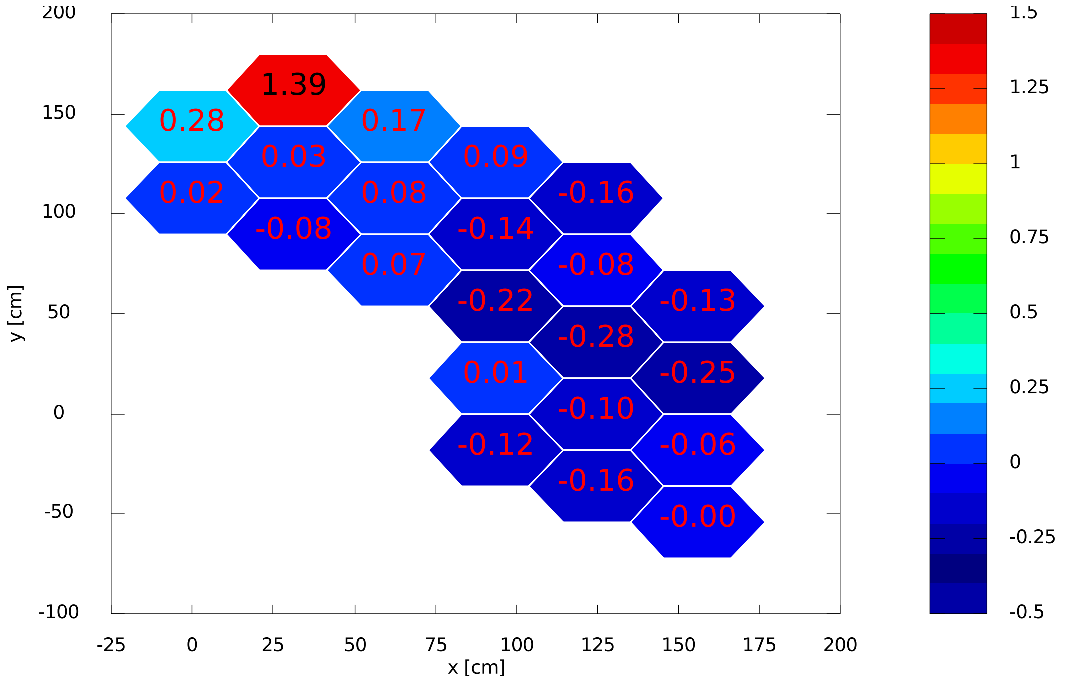

Source: OECD/NEA, 2020.

The CR homogenisation effect on the radially averaged flux distribution is included in Figure 26 and is consistent in all energy ranges with over-predictions of 5% on the top of the core and under-prediction of 3% at the bottom. The axially averaged flux distribution in Figure 27 show minimal difference, which is mainly due to cancellation from the integration operation. Detailed differences for the flux distributions at different axial levels are included in Annex C, Figure C.1 through Figure C.3. These confirm that the flux differences in the upper regions of the core are substantial with errors in the 10 to 50% range. The thermal flux difference in the fuel block where maximum power difference occurs has a value of 22%, which is consistent with the 23.97% difference in power. The thermal flux difference in the CR block adjacent to this fuel block is 18.7%. The radial distribution in the plane just above the core (8.12 m) was provided to show the homogenisation effects in the reflector region. The thermal flux difference in the rodded CR block in this plane is 48.31%.

Figure 25: CR homogenisation effect on the power distribution at various axial levels (per cent difference with one-sixth as reference)

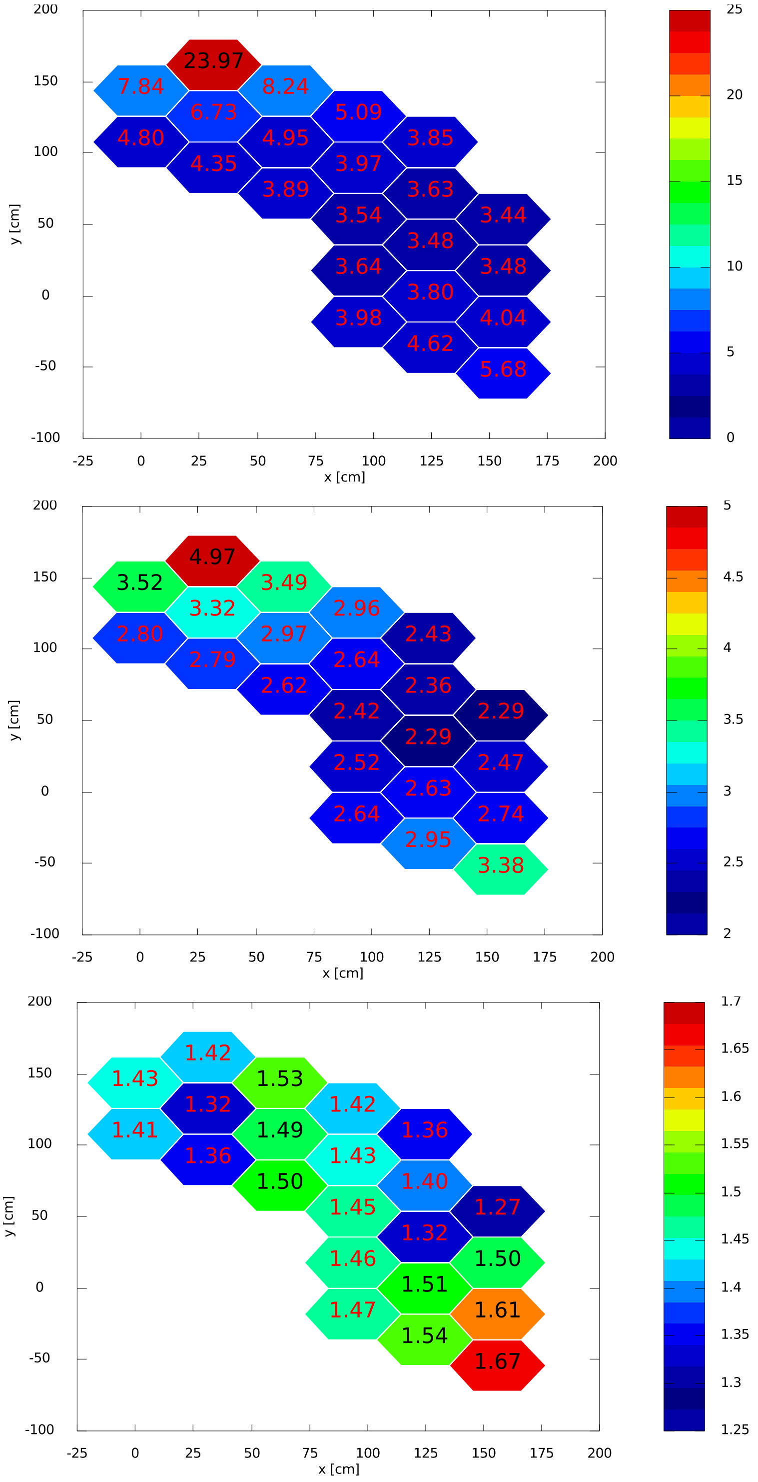

z = 7.53 m

z = 6.74 m

z = 5.95 m

z = 0.4 m

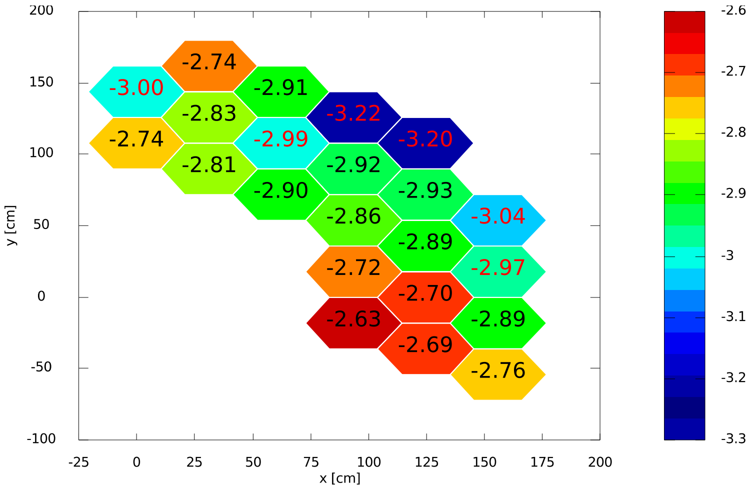

Source: OECD/NEA, 2020.

Figure 26: CR homogenisation effect on the radially averaged fast, epithermal and thermal flux distribution

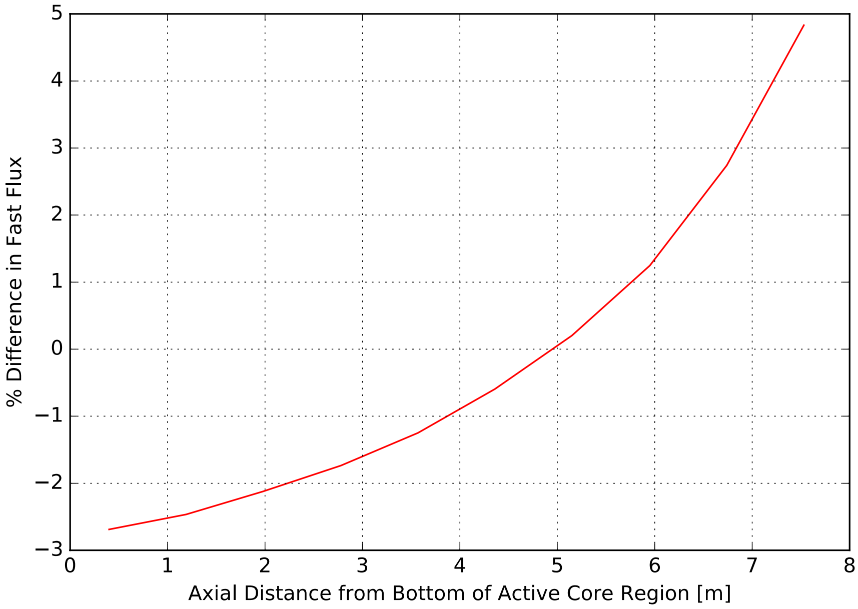

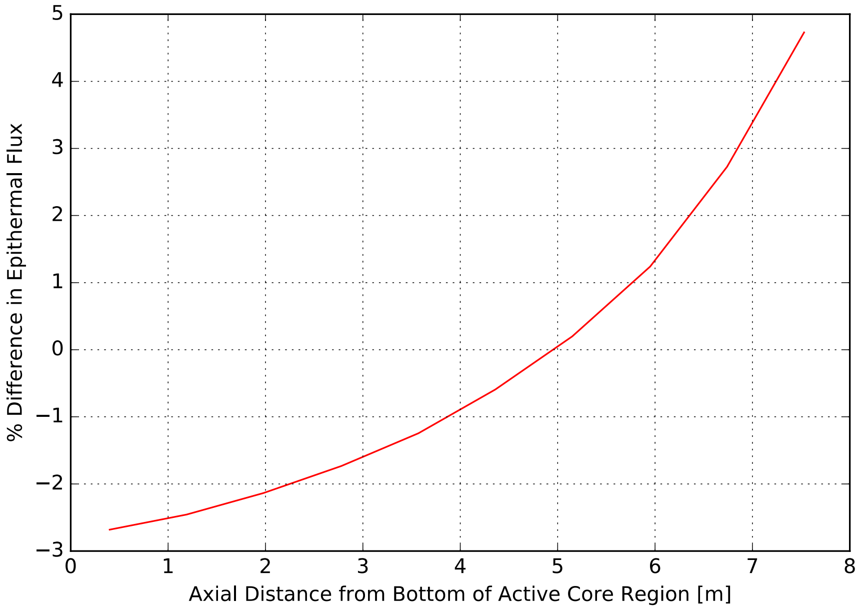

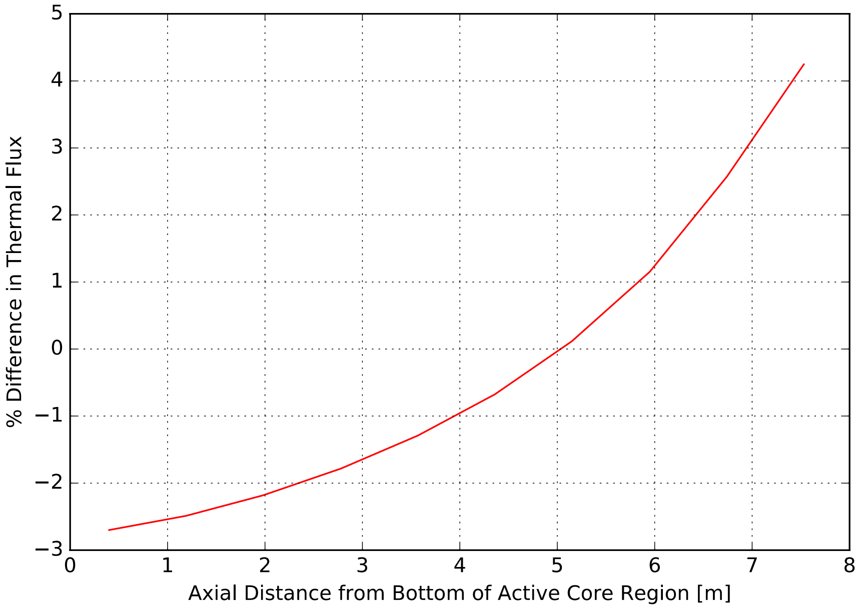

Source: OECD/NEA, 2020.

Figure 27: CR homogenisation effect on the axially averaged fast, epithermal and thermal flux distribution

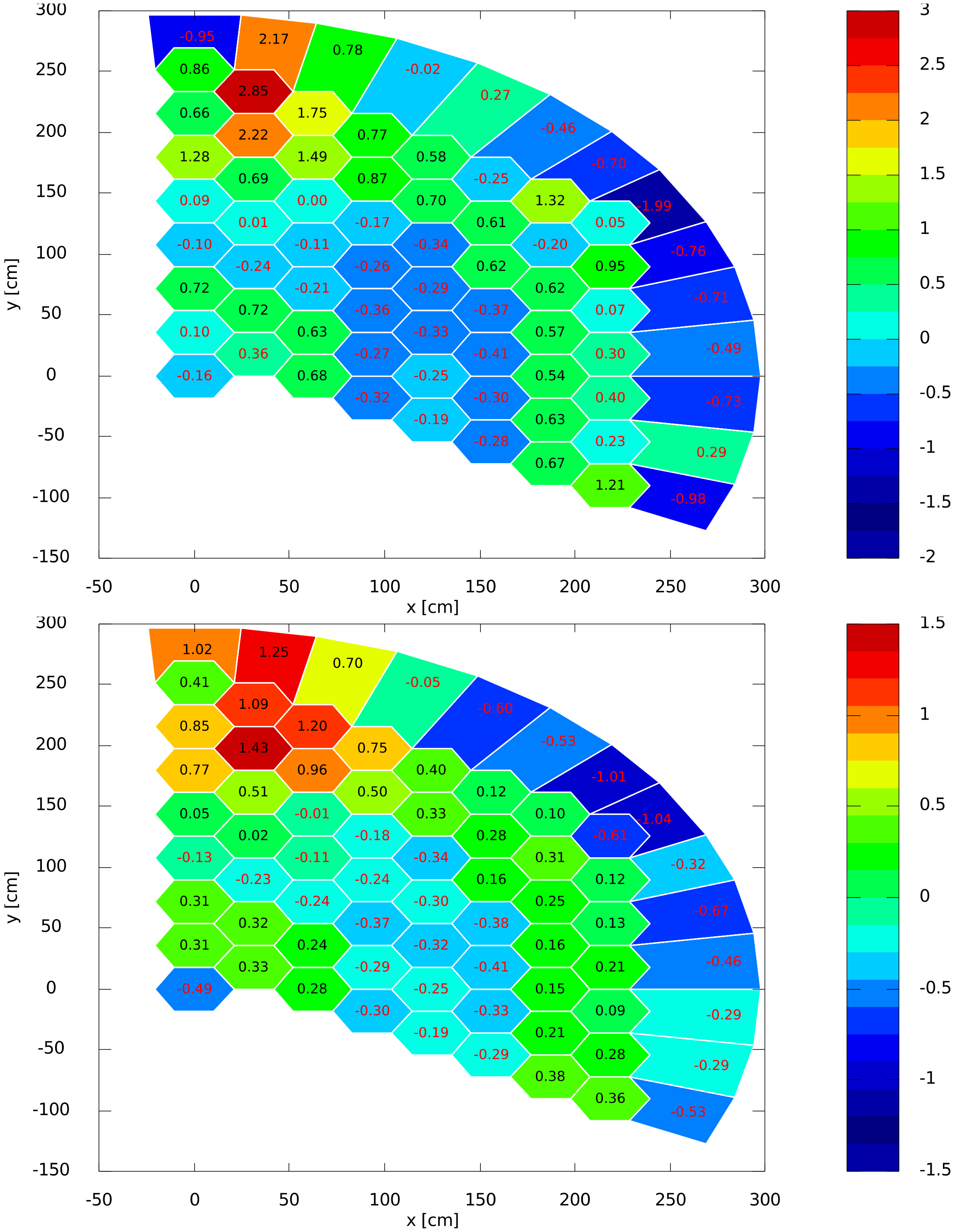

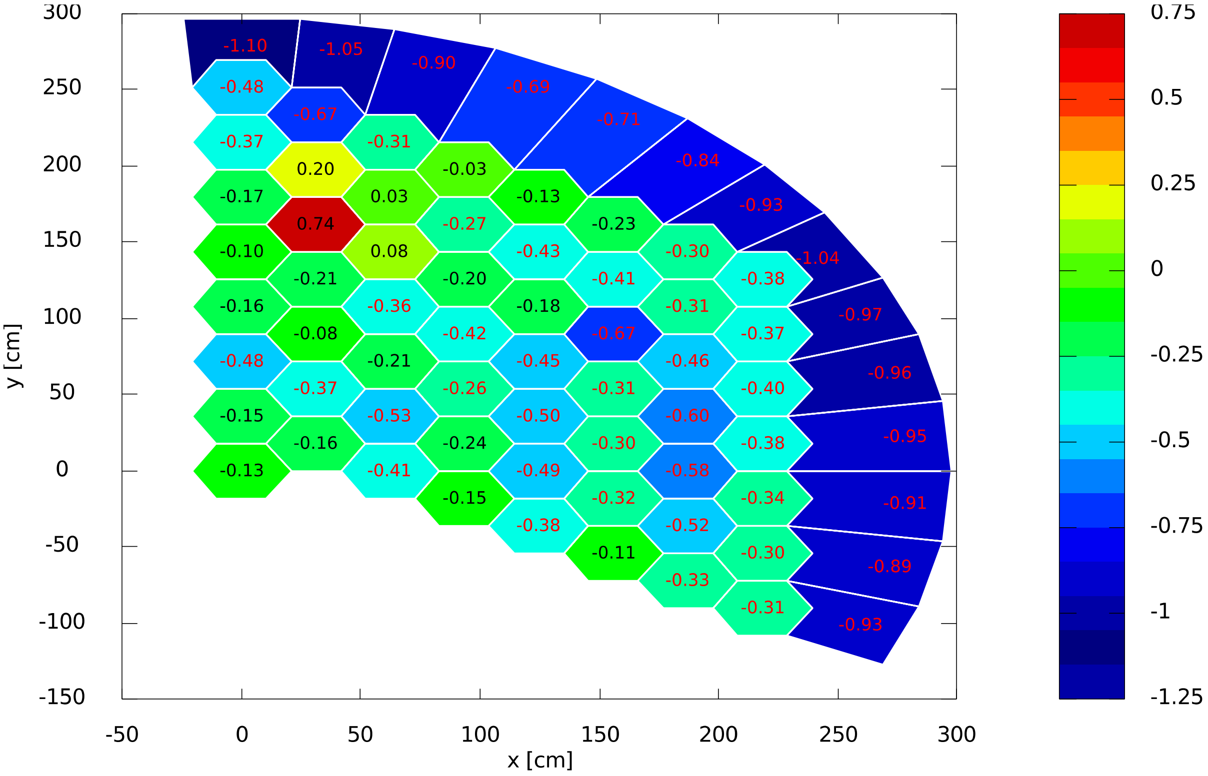

Source: OECD/NEA, 2020.

8. Conclusions

Overall, the results from these exercises show good agreement among the various models. The conclusions from this exercise are:

- The transport solvers produce eigenvalues that are ~190 pcm above the diffusion solutions for both homogenisations.
- When diffusion and transport eigenvalues are evaluated together the standard deviation (SD) is within 100 pcm of the mean.
- The type of control rod (CR) homogenisation used does not have a large effect on the eigenvalue due to the shallow insertion of the CR bank in this configuration.
- Transport solvers calculate a CR worth that is 30 pcm above that of the diffusion estimate. The relative standard deviation (RSD) in the calculation of the CR worth is less than 1% for the independent solver groups, diffusion and transport, but the combined statistical values are within 1.7%.
- The worth of the CR is very sensitive to the CR homogenisation, with 275 pcm higher CR worth using the one-sixth CR homogenisation.
- The CR homogenisation has a significant effect on the power distribution. The full homogenisation over-predicts the radially averaged power on the top of the core by 5% and under-predicts the power at the bottom of the core by -2.6%. The radial power distributions (RPDs) show a maximum difference of 23.97% between the two CR homogenisations at the top level of the active core region.
- The CR homogenisation produces thermal flux differences of 22% in the active core.

References

[1] NEA (2013), *PBMR Coupled Neutronic/Thermal Hydraulics Transient Benchmark: The PBMR-400 Core Design*, NEA/NSC/DOC(2013)10.

[2] Neylan, A.J., D.V. Graf, A.C. Millunzi (1988), "The modular high temperature gas-cooled reactor (MHTGR) in the U.S", *Nuc. Eng. & Des.,* Vol. 109, pp. 99–105.

[3] Marleau, G., A. Hébert, and R. Roy (2010), *A User Guide for Dragon Version 4, Technical Report IGE–294,* École Polytechnique de Montréal.

[4] McClarren, R G. (2011), *Theoretical Aspects of the Simplified PN Equations, Transport Theory and Statistical Physics*, 39:73–109, 2011, ISSN: 0041-1450 print/1532-2424, DOI: 10.1080/00411450.2010.535088.

Bibliography

"Nuclear Reactor Analysis", J. J. Duderstadt, L. J. Hamilton, 1 ed., John Wiley & Sons, 1976.

"Physics of High-Temperature Reactors", Luigi Massimo, 1st ed., Pergamon Press Oxford, 1976.

Annex A: Supporting plots for cases with fully homogenised control rod

Figure A.1: Per cent difference in the radially averaged APD from the various solutions versus the average APD from the transport solvers (fully homogenised CR)

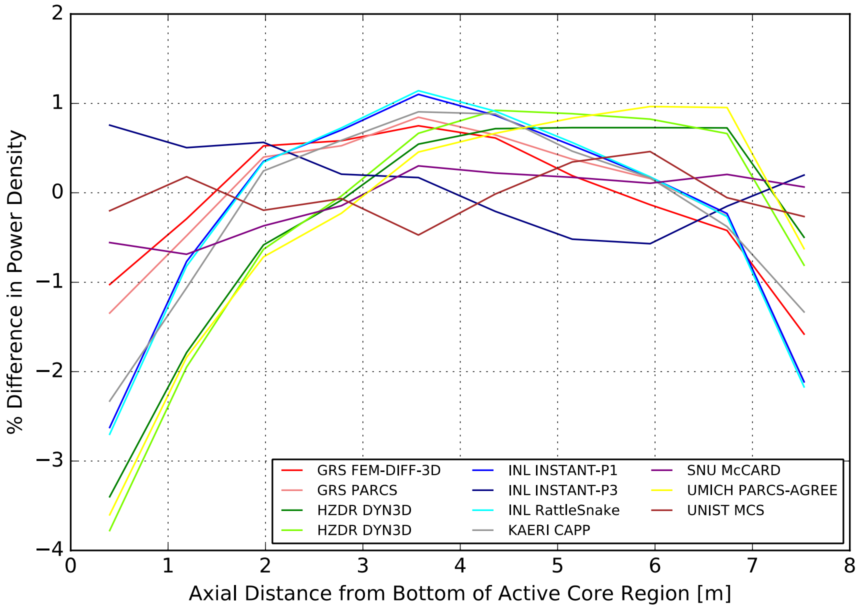

Source: OECD/NEA, 2020.

Figure A.2: Per cent difference in the axially averaged RPD from diffusion versus transport (fully homogenised CR)

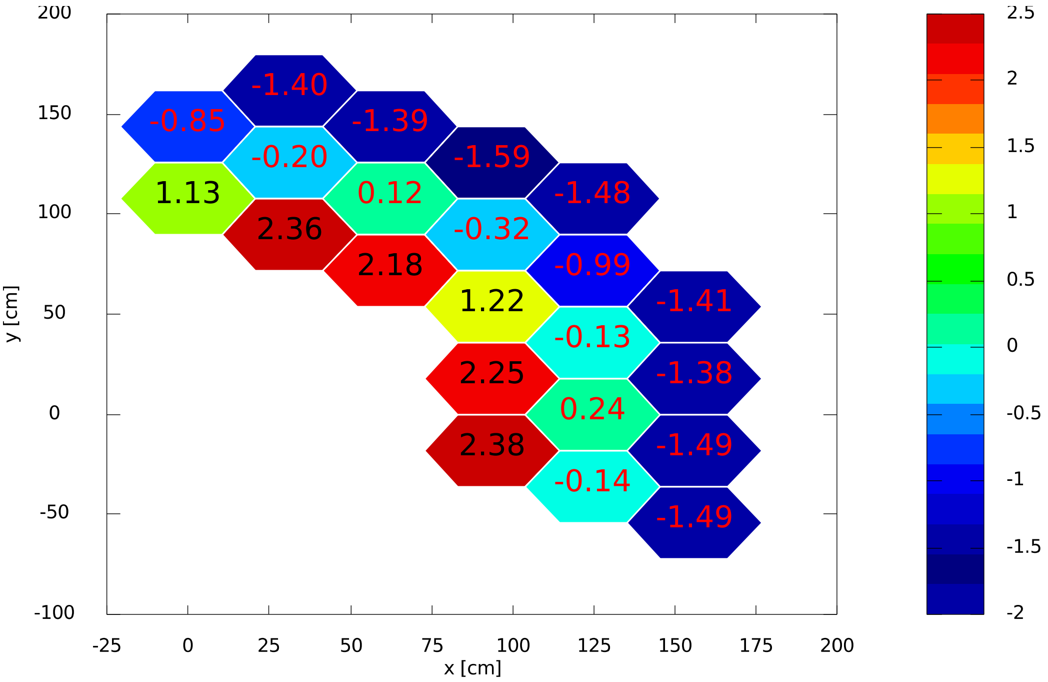

Source: OECD/NEA, 2020.

Figure A.3: Power distribution for the diffusion solvers (left to right starting at level 1)

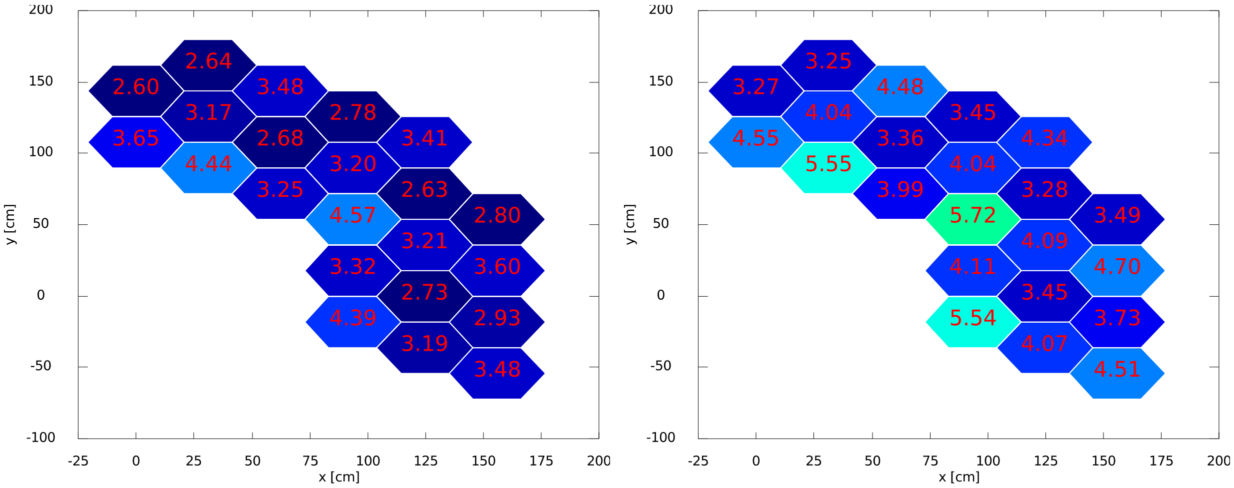

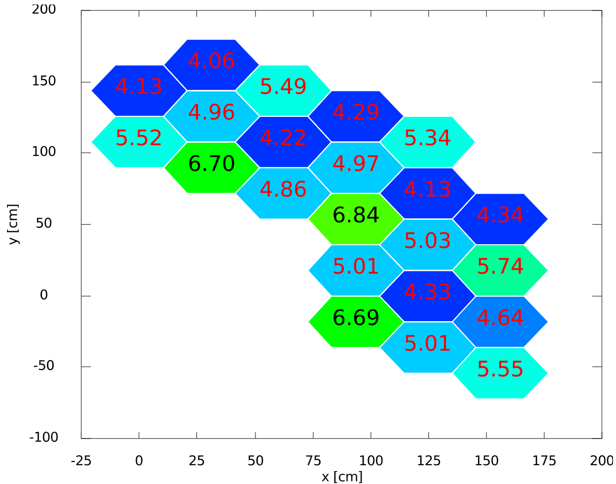
200
150
100
50
0
-50
-100
y [cm]
4.06
4.13
5.49
4.96
4.29
5.52
4.22
5.34
6.70
4.97
4.86
4.13
6.84
4.34
5.03
5.01
5.74
4.33
6.69
4.64
5.01
5.55
-25
0
25
50
75
100
125
150
175
200
x [cm]

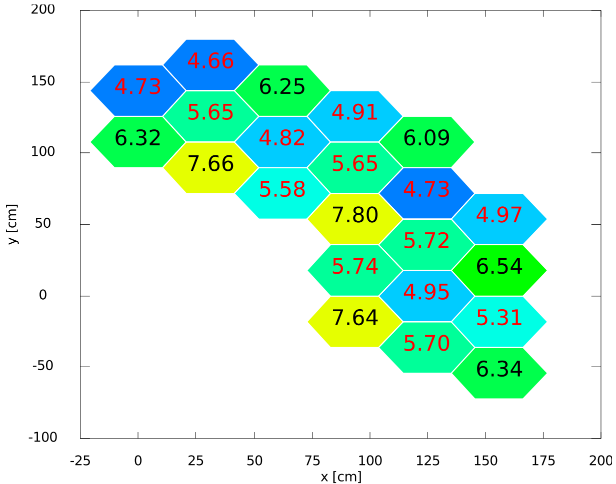
200
150
100
50
0
-50
-100
y [cm]
4.66
4.73
6.25
5.65
4.91
6.32
4.82
6.09
7.66
5.65
5.58
4.73
7.80
4.97
5.72
5.74
6.54
4.95
7.64
5.31
5.70
6.34
-25
0
25
50
75
100
125
150
175
200
x [cm]

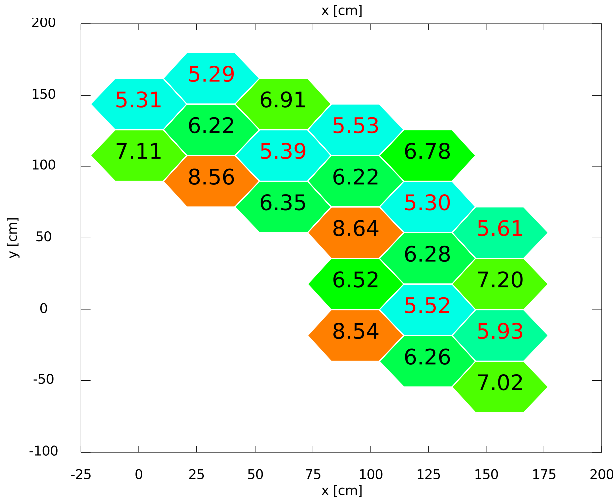
200
150
100
50
0
-50
-100
y [cm]
5.29
5.31
6.91
6.22
5.53
7.11
5.39
6.78
8.56
6.22
6.35
5.30
8.64
5.61
6.28
6.52
7.20
5.52
8.54
5.93
6.26
7.02
-25
0
25
50
75
100
125
150
175
200
x [cm]

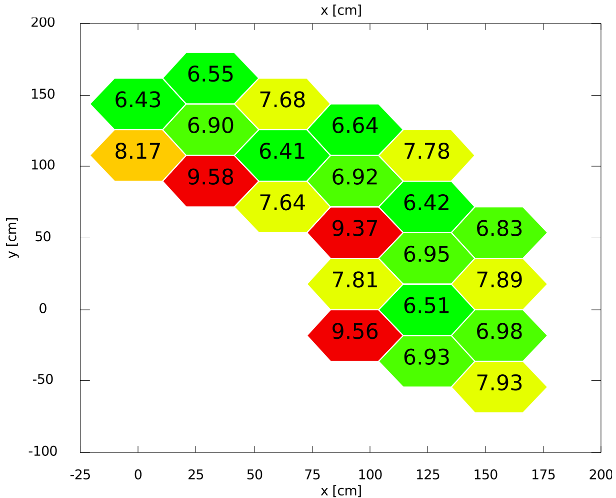
200
150
100
50
0
-50
-100
y [cm]
6.55
6.43
7.68
6.90
6.64
8.17
6.41
7.78
9.58
6.92
7.64
6.42
9.37
6.83
6.95
7.81
7.89
6.51
9.56
6.98
6.93
7.93
-25
0
25
50
75
100
125
150
175
200
x [cm]

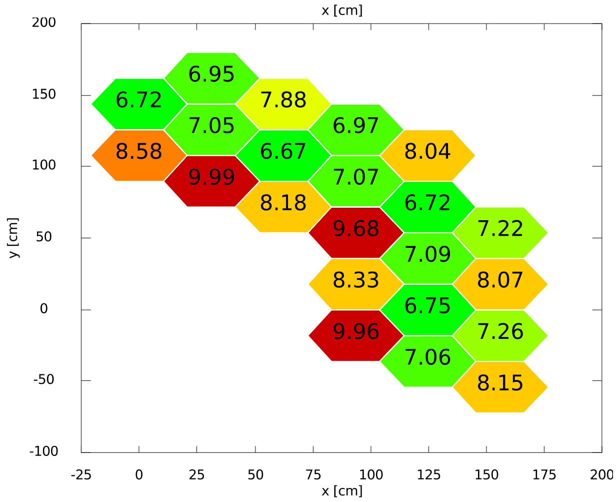
200
150
100
50
0
-50
-100
y [cm]
6.95
6.72
7.88
7.05
6.97
8.58
6.67
8.04
9.99
7.07
8.18
6.72
9.68
7.22
7.09
8.33
8.07
6.75
9.96
7.26
7.06
8.15
-25
0
25
50
75
100
125
150
175
200
x [cm]

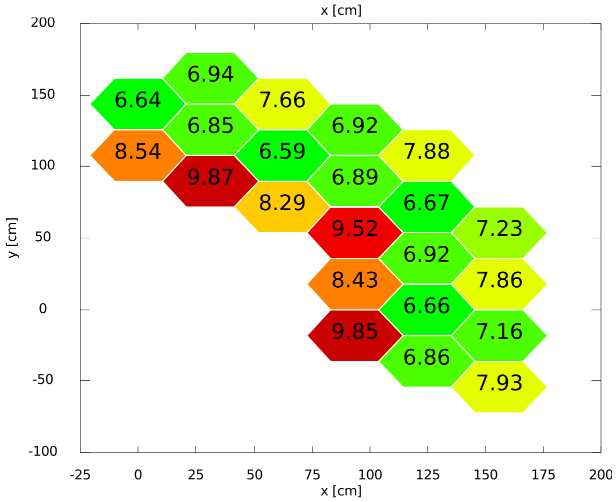
200
150
100
50
0
-50
-100
y [cm]
6.94
6.64
7.66
6.85
6.92
8.54
6.59
7.88
9.87
6.89
8.29
6.67
9.52
7.23
6.92
8.43
7.86
6.66
9.85
7.16
6.86
7.93
-25
0
25
50
75
100
125
150
175
200
x [cm]

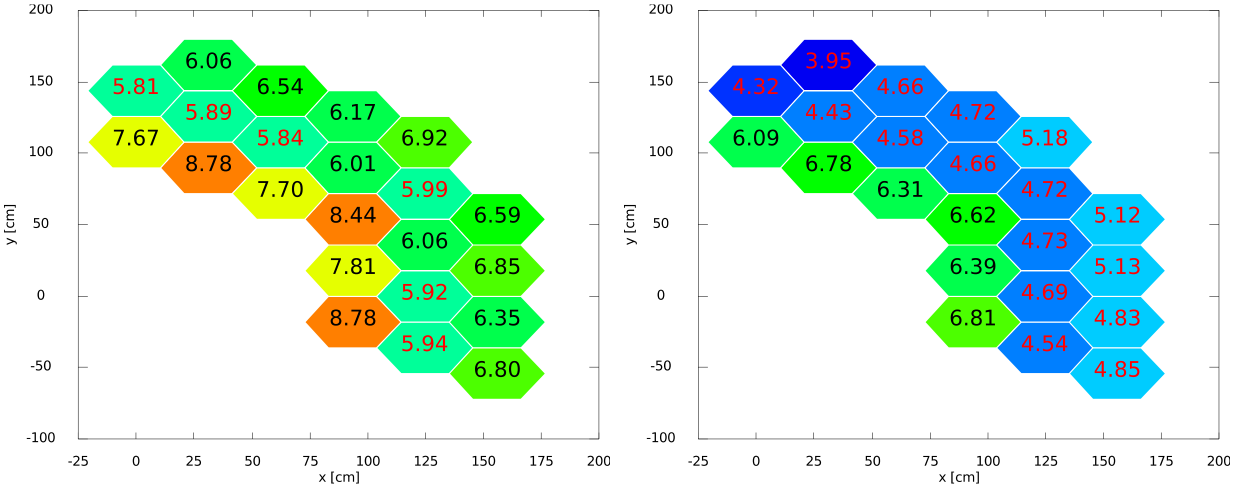

Source: OECD/NEA, 2020.

Figure A.4: Power distribution for the transport solvers (left to right starting at level 1)

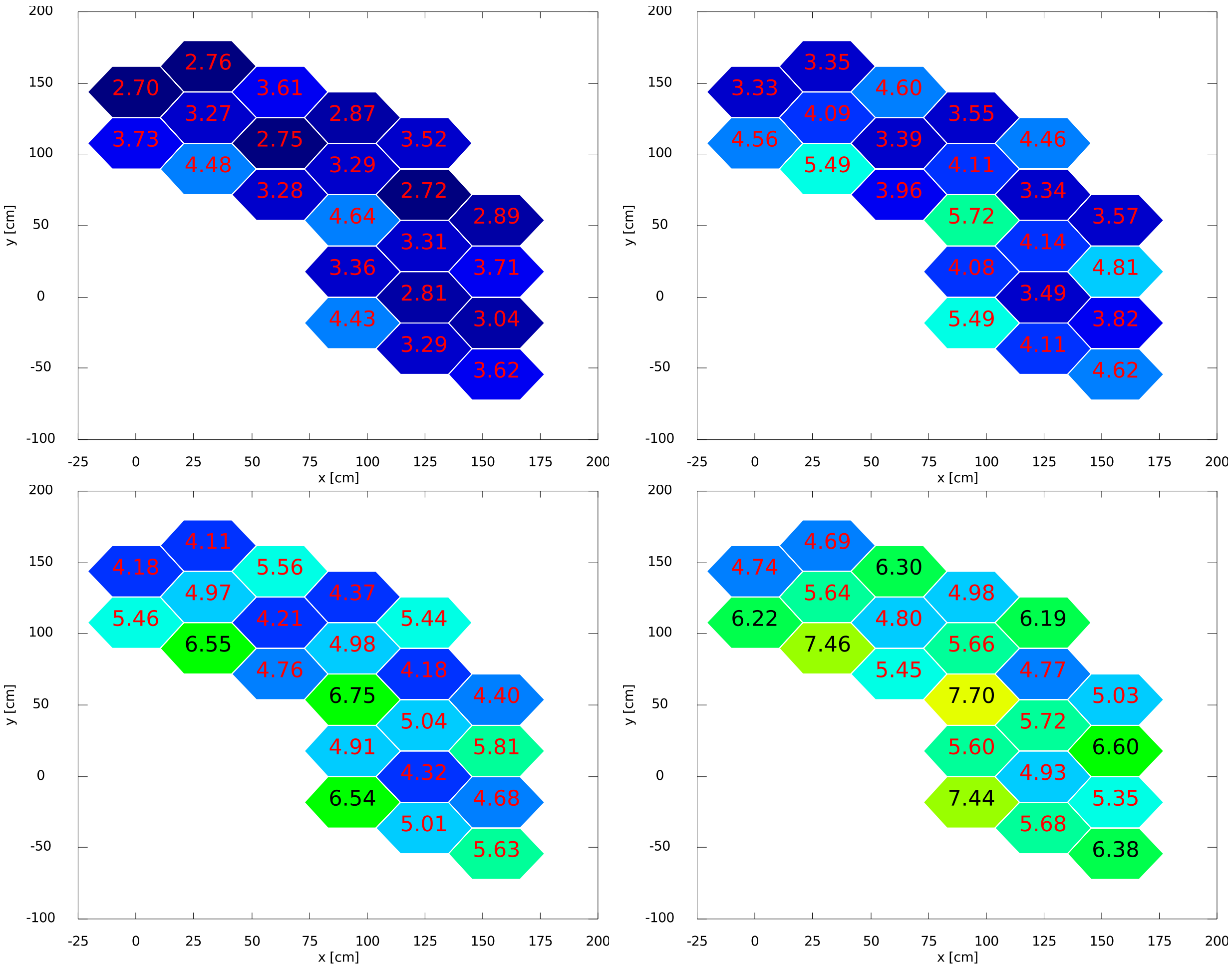

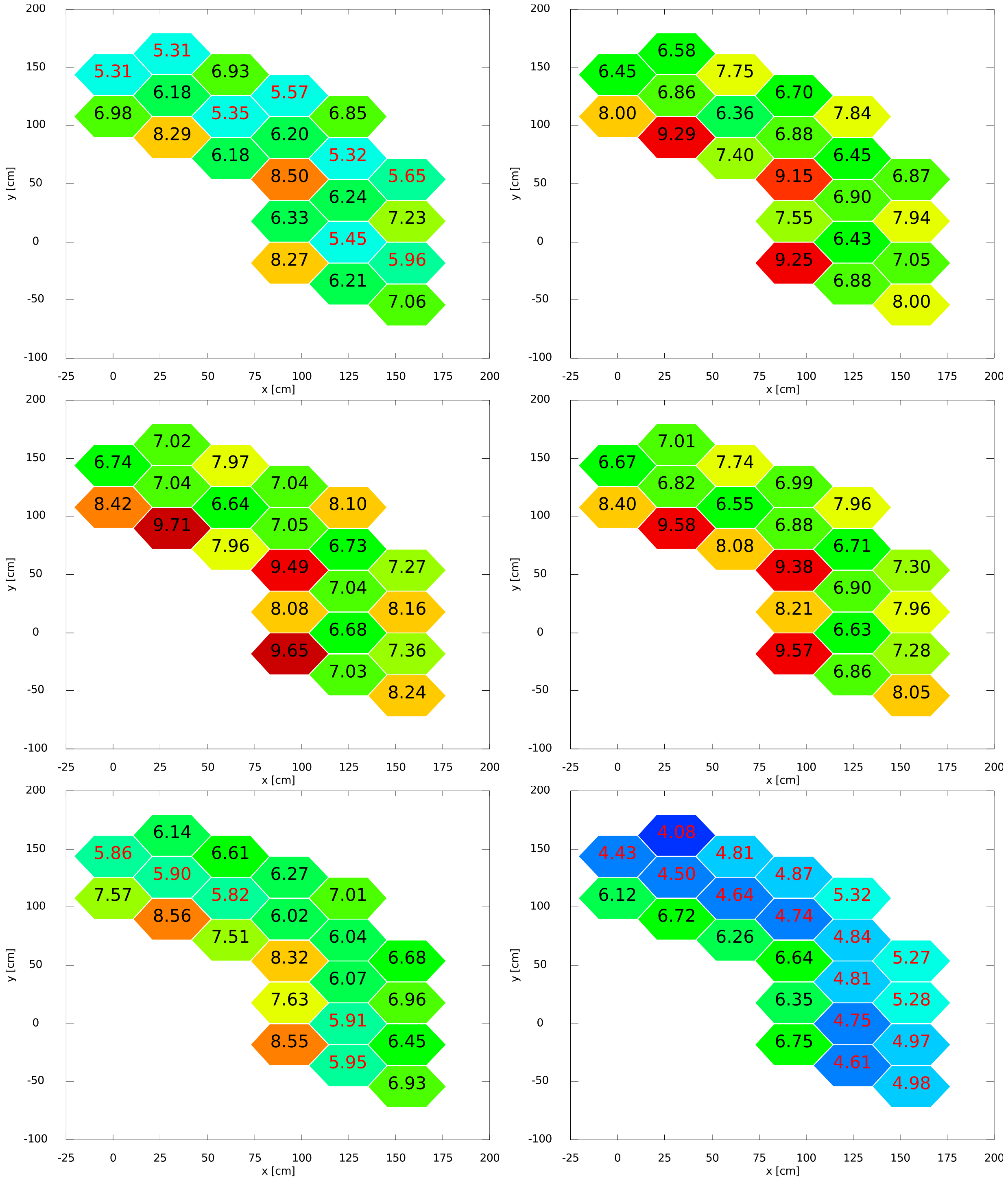

Source: OECD/NEA, 2020.

Figure A.5: Mean value and RSD for the axially averaged (active core region) fast flux−diffusion solutions

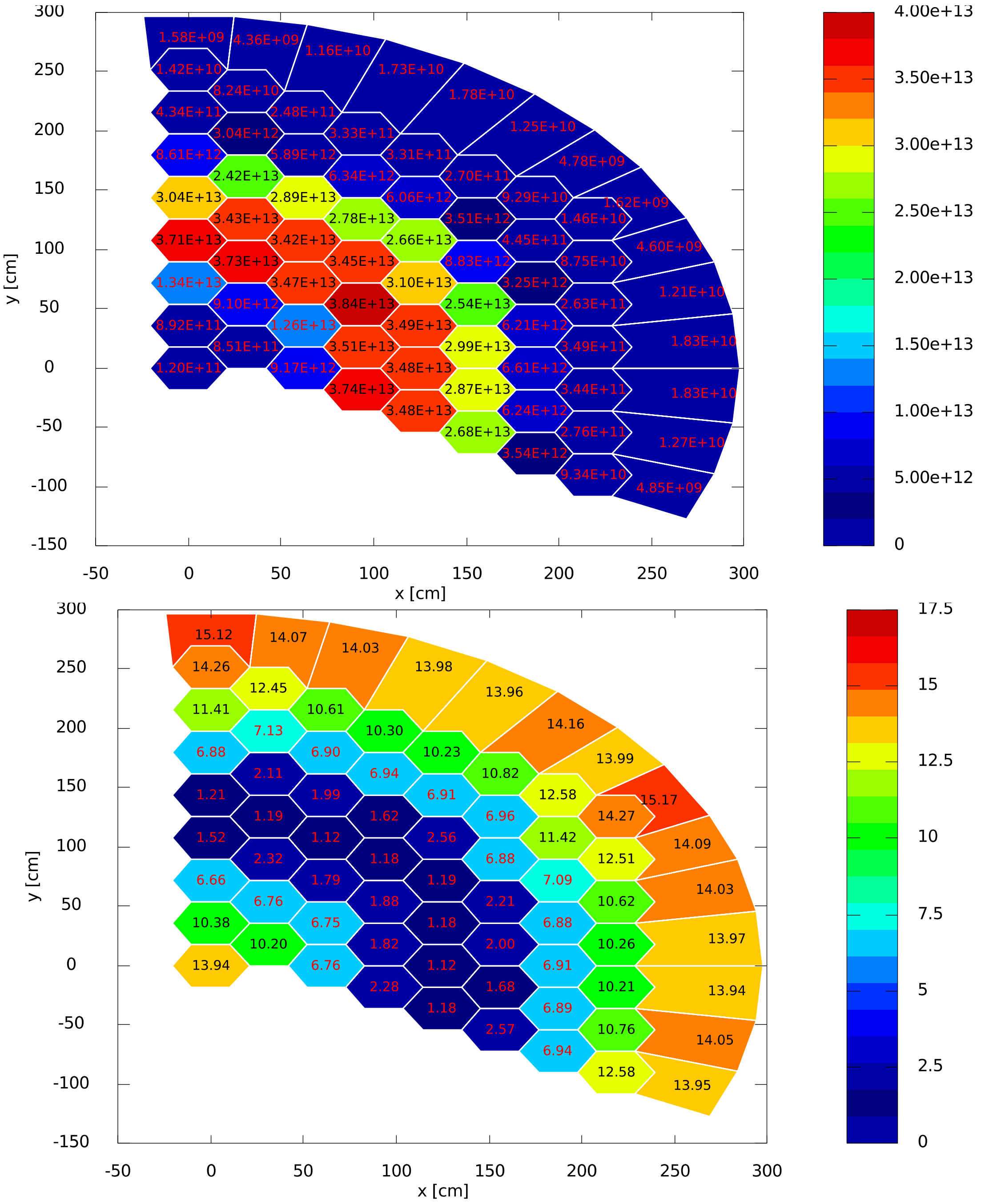

Source: OECD/NEA, 2020.

Figure A.6: Mean value and RSD for the axially averaged (active core region) fast flux–transport solutions

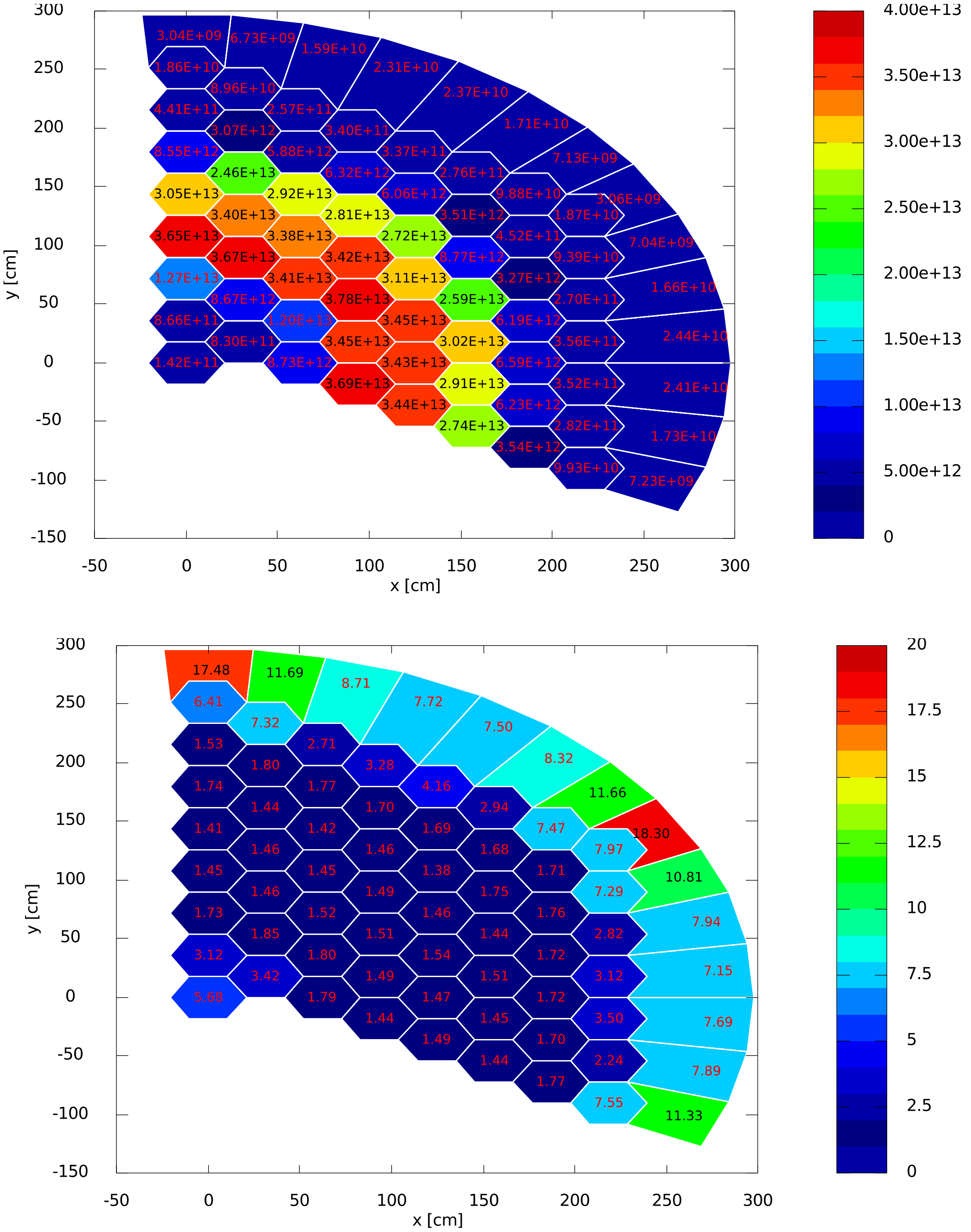

Source: OECD/NEA, 2020.

Figure A.7: Mean value and RSD for the axially averaged (active core region) epithermal flux−diffusion solutions

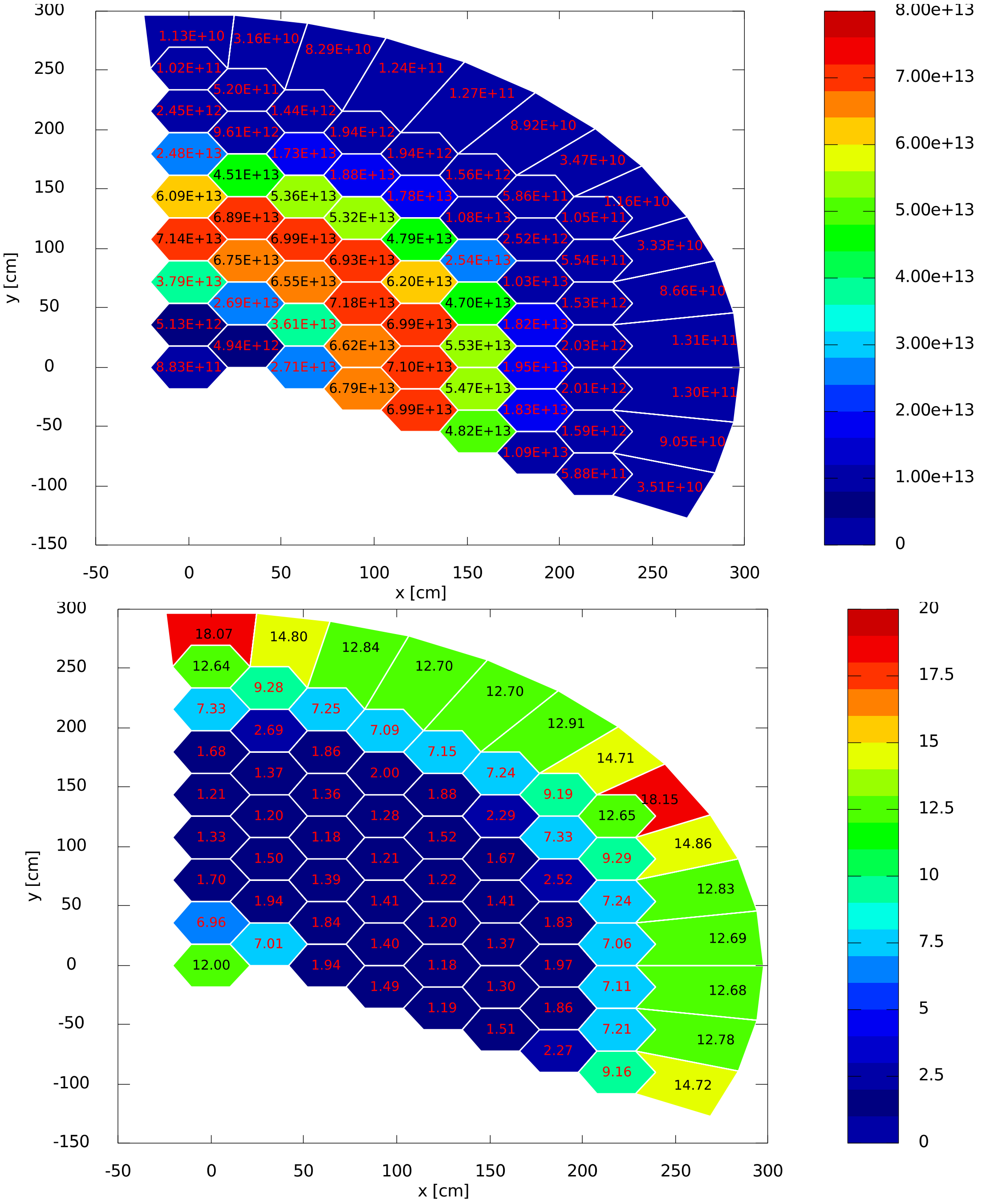

Source: OECD/NEA, 2020.

Figure A.8: Mean value and RSD for the axially averaged (active core region) epithermal flux–transport solutions

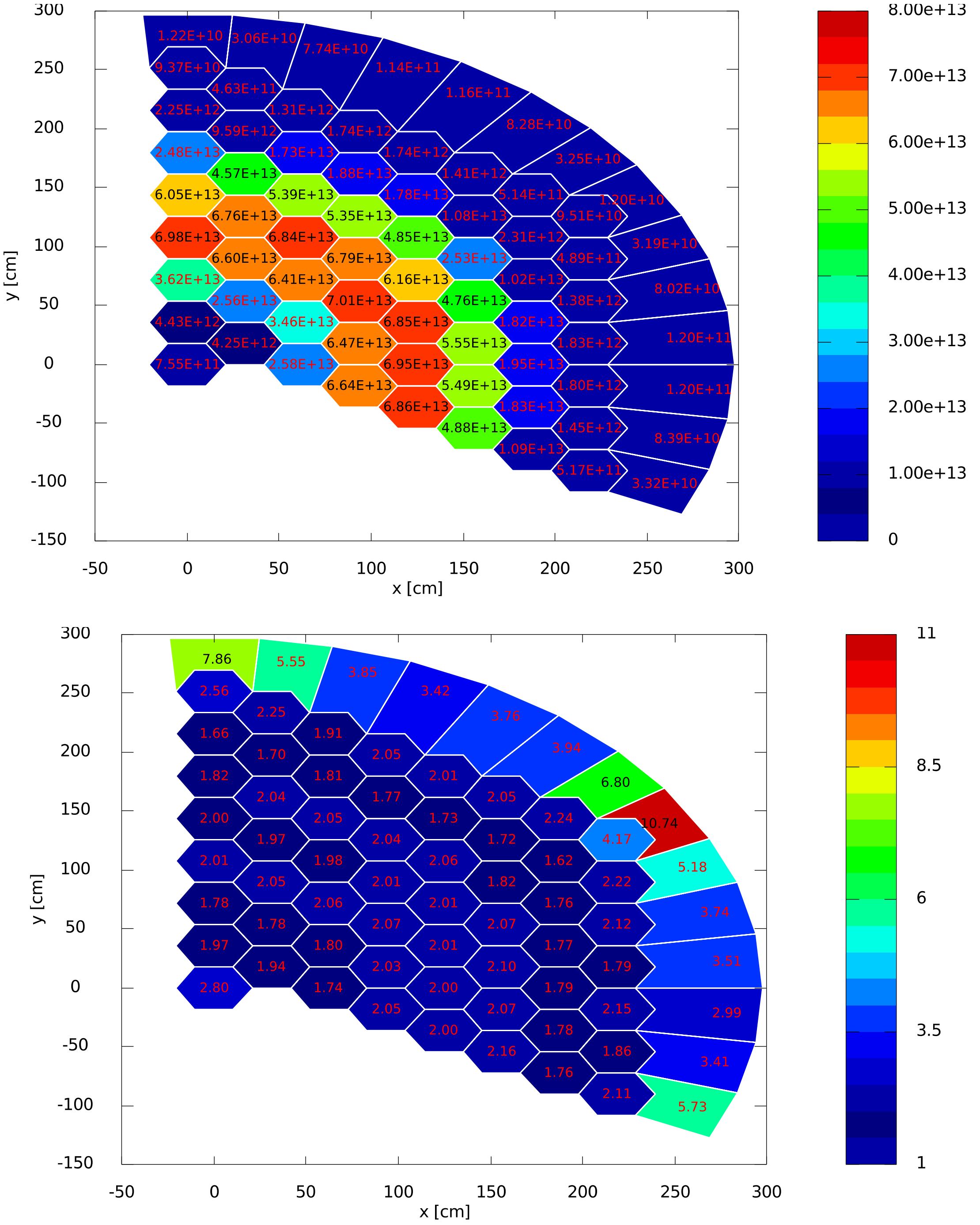

Source: OECD/NEA, 2020.

Figure A.9: Mean value and RSD for the axially averaged (active core region) thermal flux−diffusion solutions

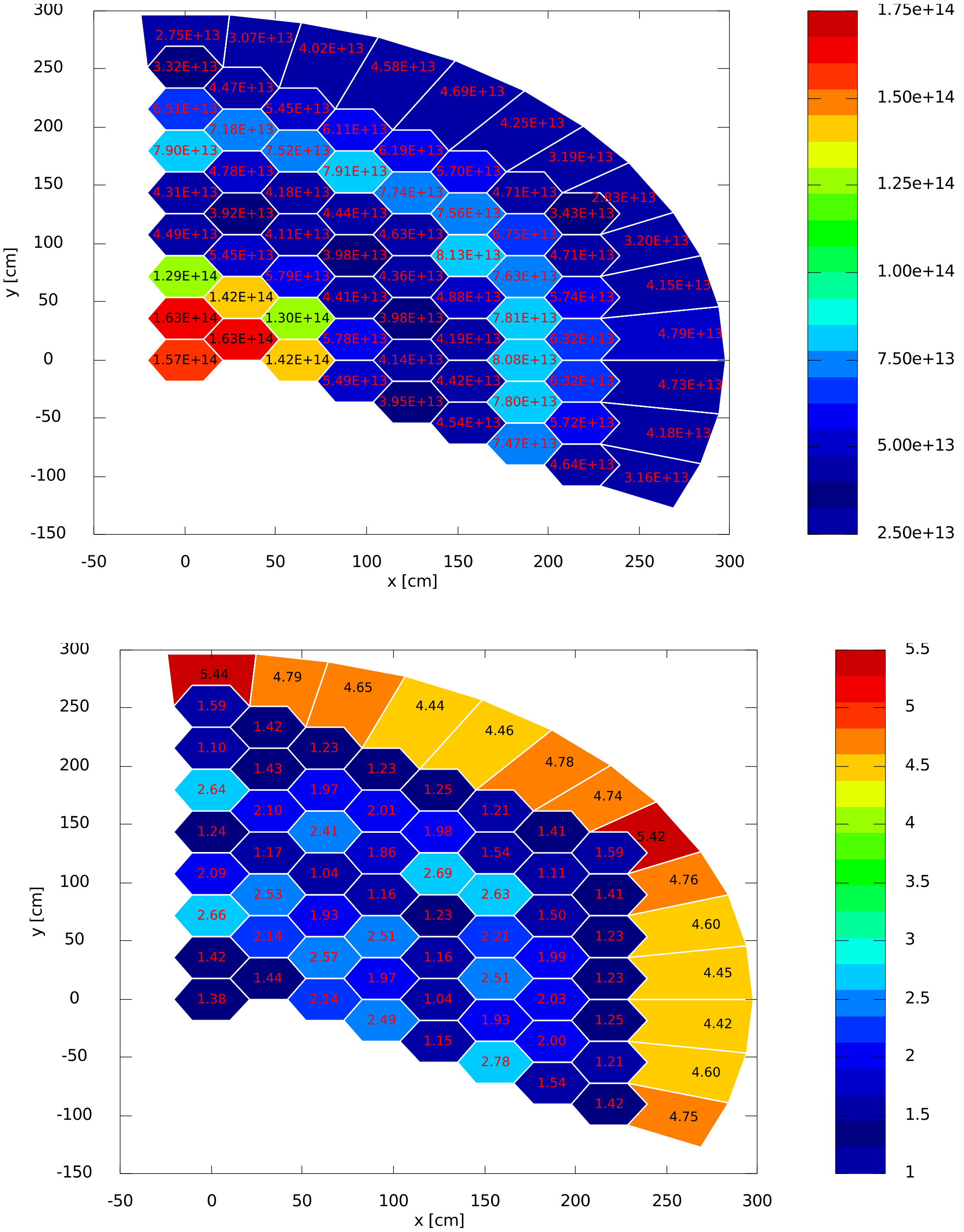

Source: OECD/NEA, 2020.

Figure A.10: Mean value and RSD for the axially averaged (active core region) thermal flux–transport solutions

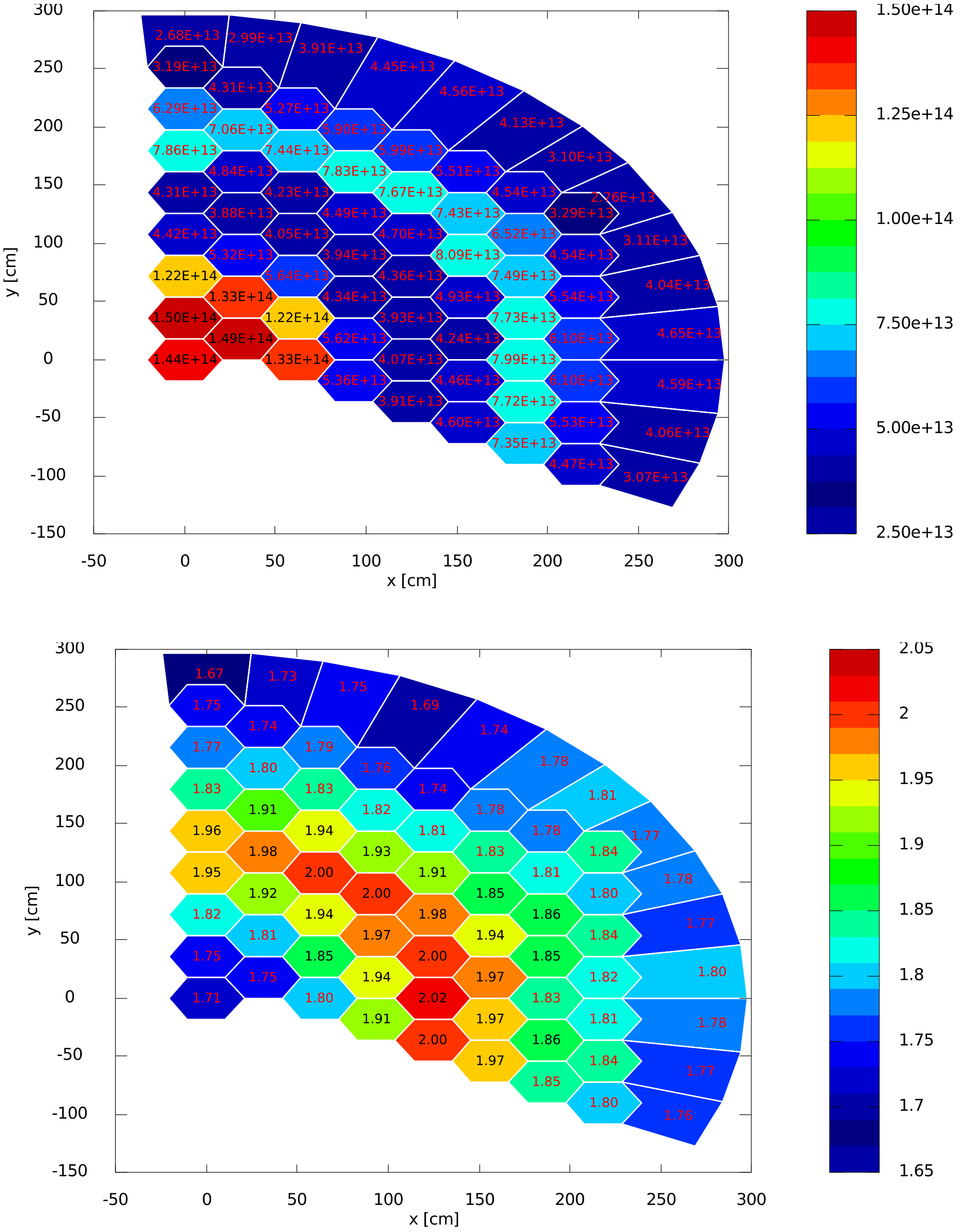

Source: OECD/NEA, 2020.

Annex B: Supporting plots for the one-sixth block control rod homogenisation

Figure B.1: Per cent difference in the radially averaged APD from the various solutions versus the average APD from the transport solvers (one-sixth block homogenised CR)

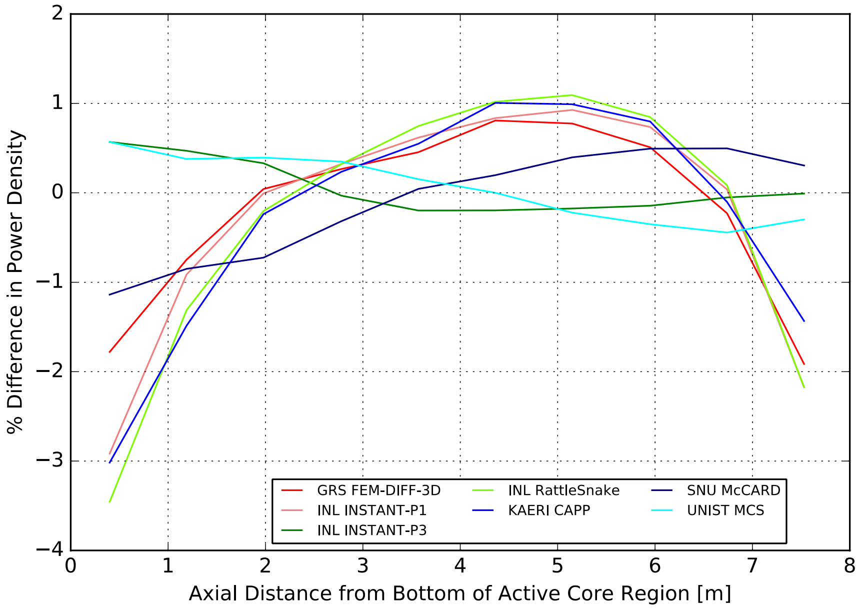

Source: OECD/NEA, 2020.

Figure B.2: Per cent difference in the axially averaged RPD from diffusion versus transport (one-sixth block homogenised CR)

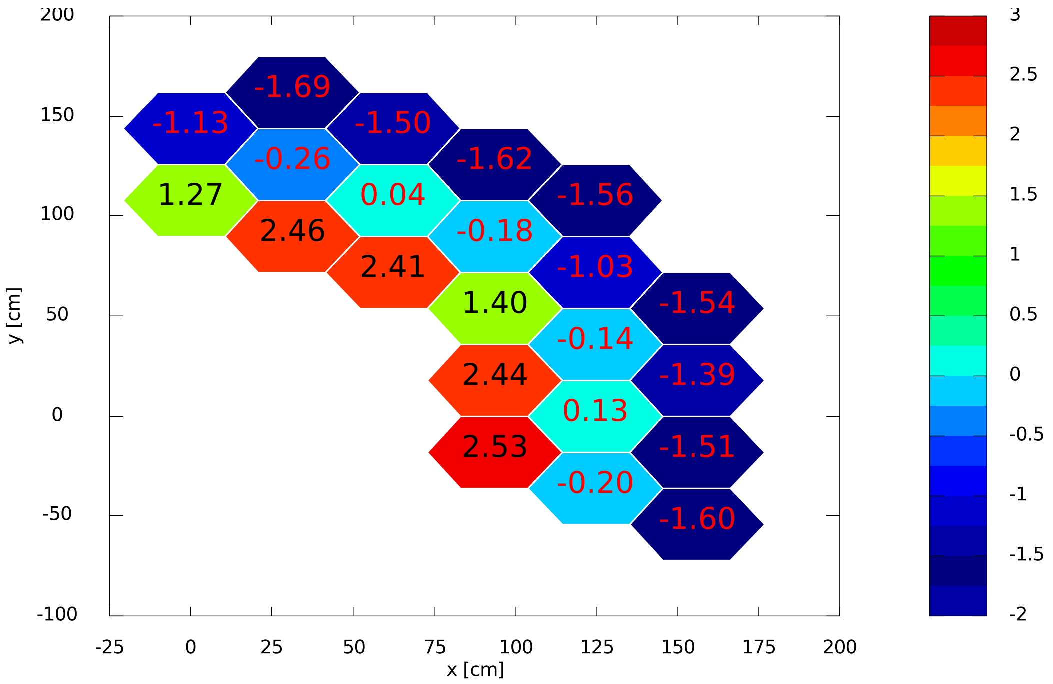

Source: OECD/NEA, 2020.

Figure B.3: Power distribution for the diffusion solvers (left to right starting at level 1)

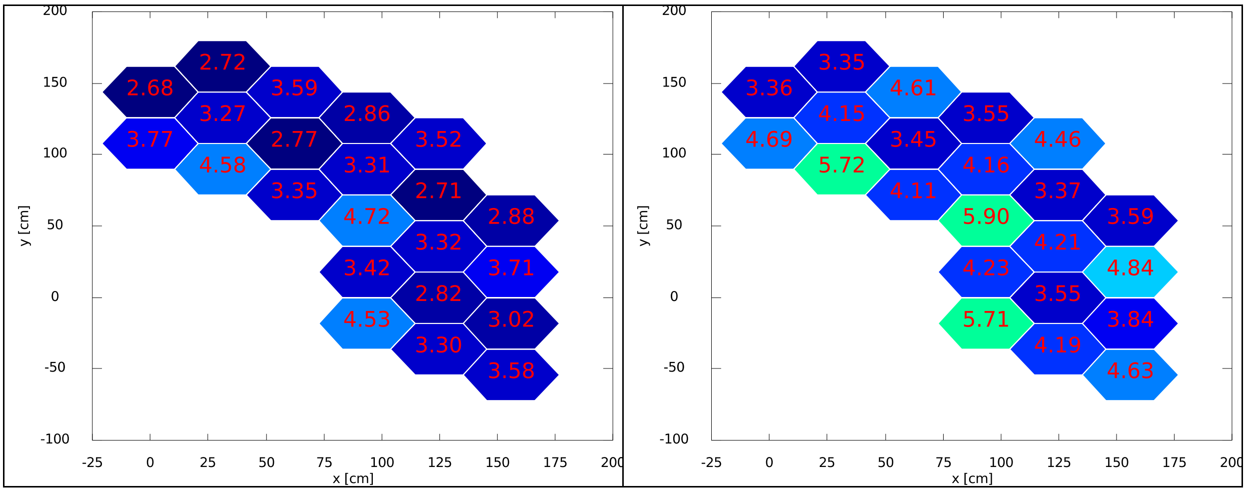

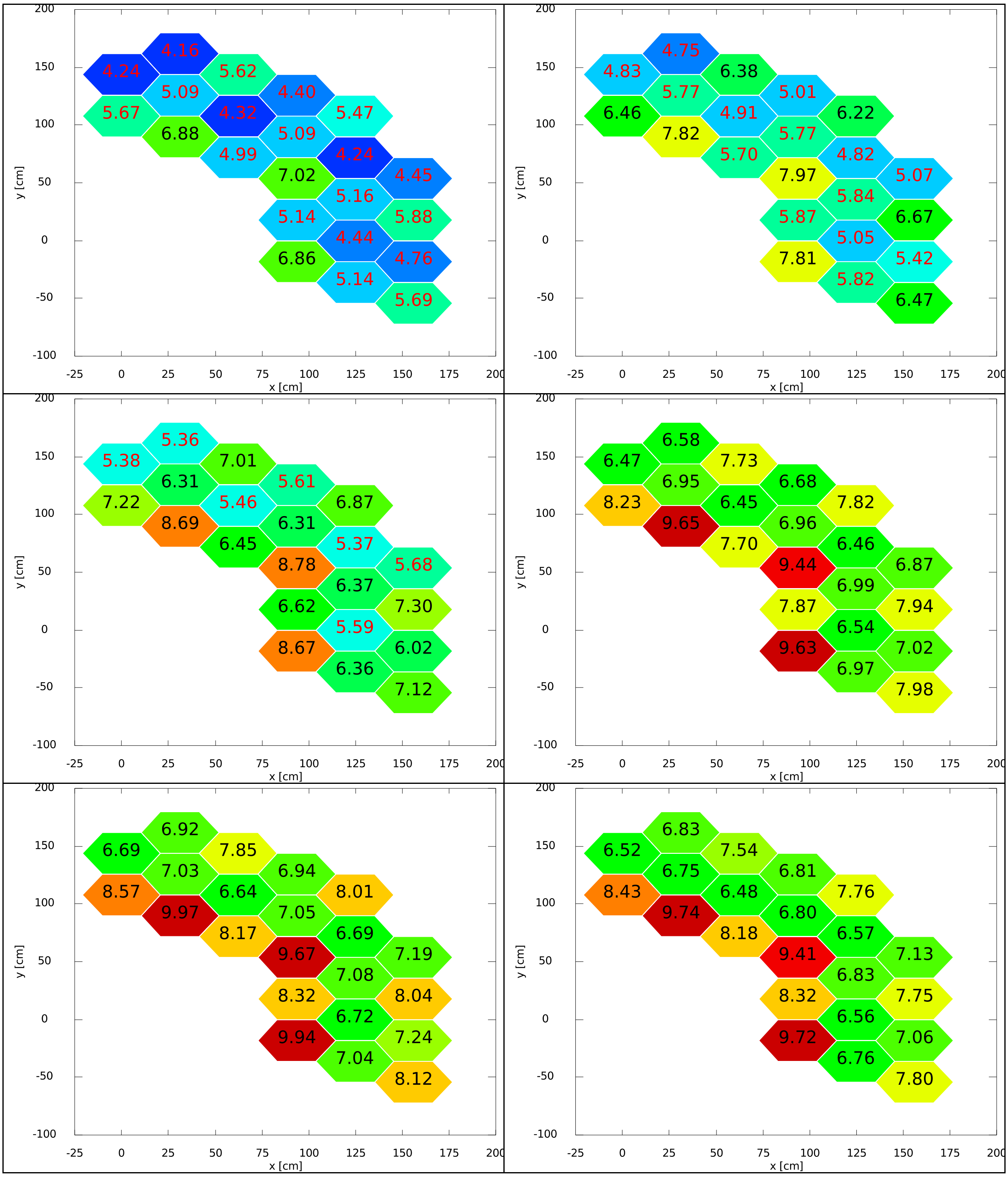
y [cm]
x [cm]
200
150
100
50
0
-50
-100
-25
0
25
50
75
100
125
150
175
200
4.16 4.24 5.62 5.09 4.40 5.67 4.32 5.47 6.88 5.09 4.99 4.24 7.02 4.45 5.16 5.14 5.88 4.44 6.86 4.76 5.14 5.69
4.75 4.83 6.38 5.77 5.01 6.46 4.91 6.22 7.82 5.77 5.70 4.82 7.97 5.07 5.84 5.87 6.67 5.05 7.81 5.42 5.82 6.47
5.36 5.38 7.01 6.31 5.61 7.22 5.46 6.87 8.69 6.31 6.45 5.37 8.78 5.68 6.37 6.62 7.30 5.59 8.67 6.02 6.36 7.12
6.58 6.47 7.73 6.95 6.68 8.23 6.45 7.82 9.65 6.96 7.70 6.46 9.44 6.87 6.99 7.87 7.94 6.54 9.63 7.02 6.97 7.98
6.92 6.69 7.85 7.03 6.94 8.57 6.64 8.01 9.97 7.05 8.17 6.69 9.67 7.19 7.08 8.32 8.04 6.72 9.94 7.24 7.04 8.12
6.83 6.52 7.54 6.75 6.81 8.43 6.48 7.76 9.74 6.80 8.18 6.57 9.41 7.13 6.83 8.32 7.75 6.56 9.72 7.06 6.76 7.80

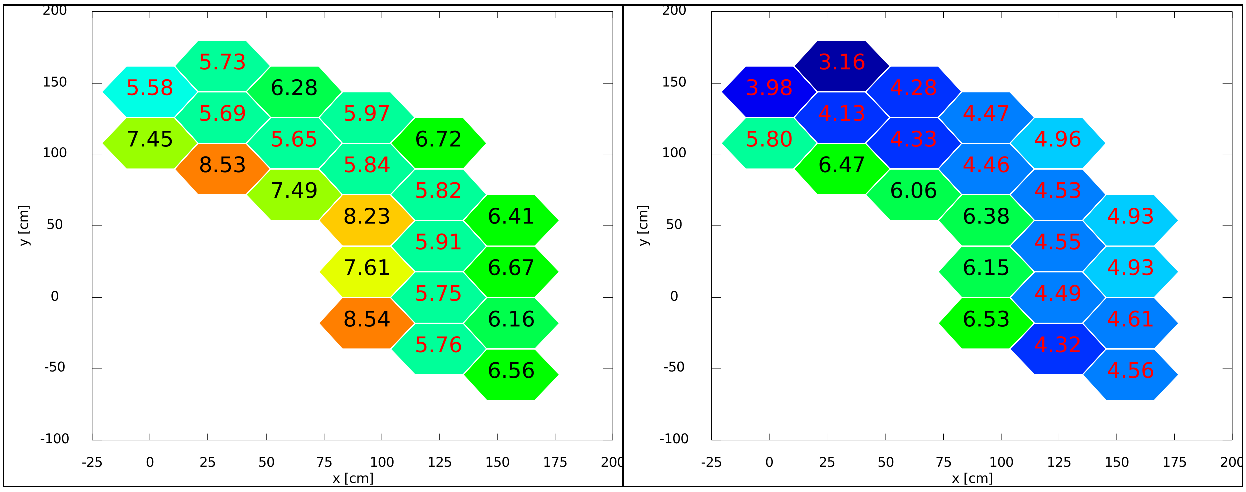

Source: OECD/NEA, 2020.

Figure B.4: Power distribution for the transport solvers (left to right starting at level 1)

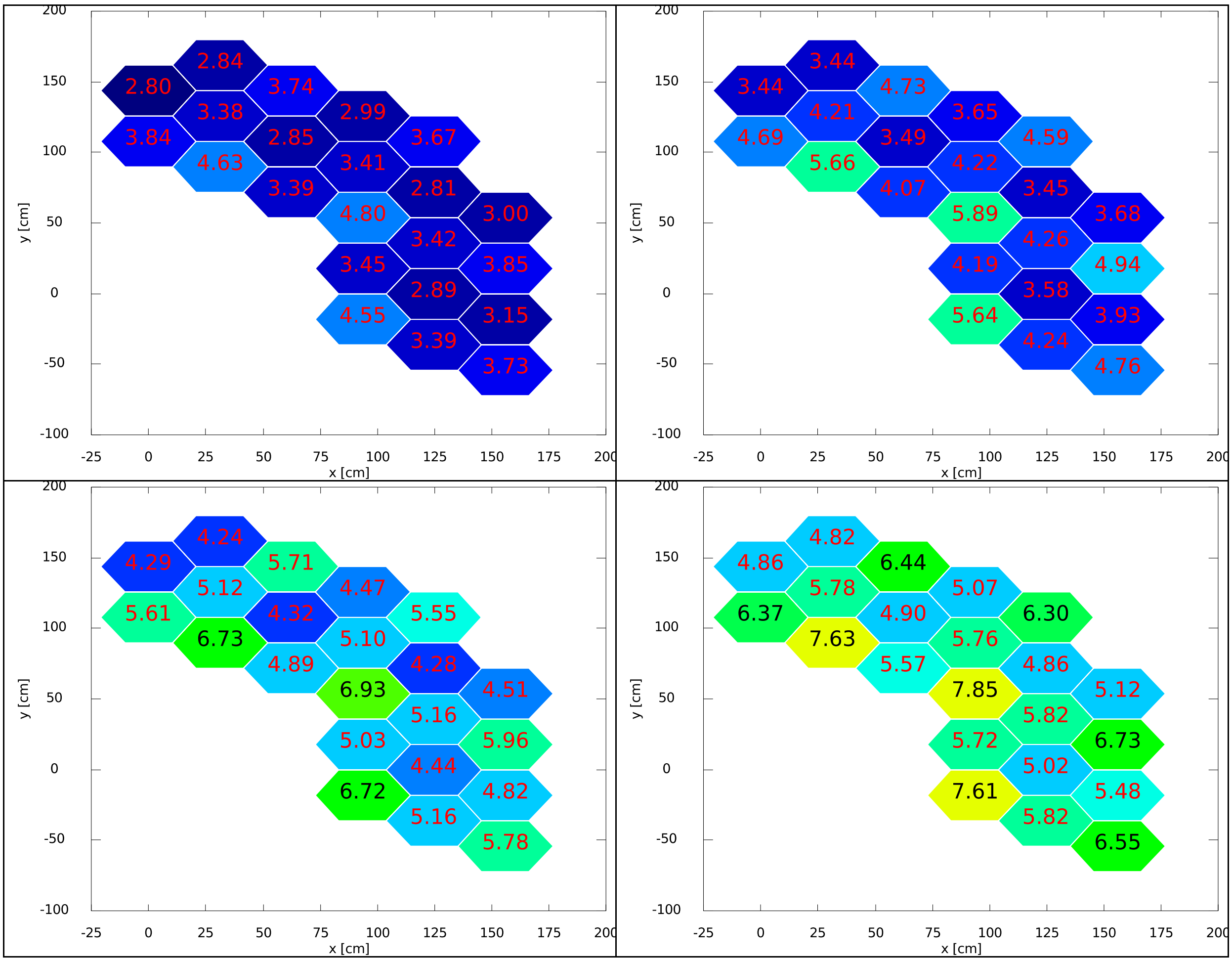

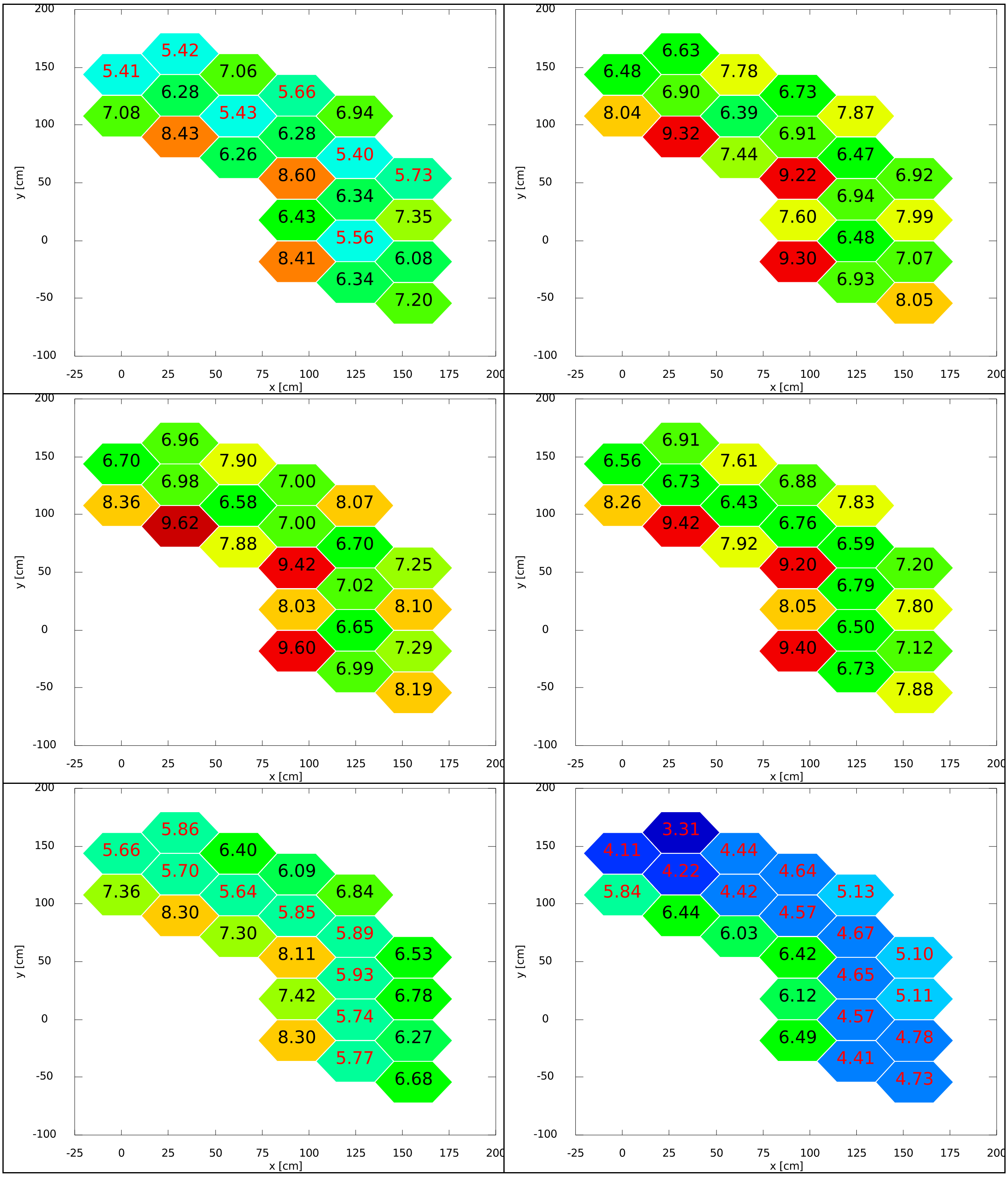

Source: OECD/NEA, 2020.

Figure B.5: Mean value and RSD for the axially averaged (active core region) fast flux–diffusion solutions

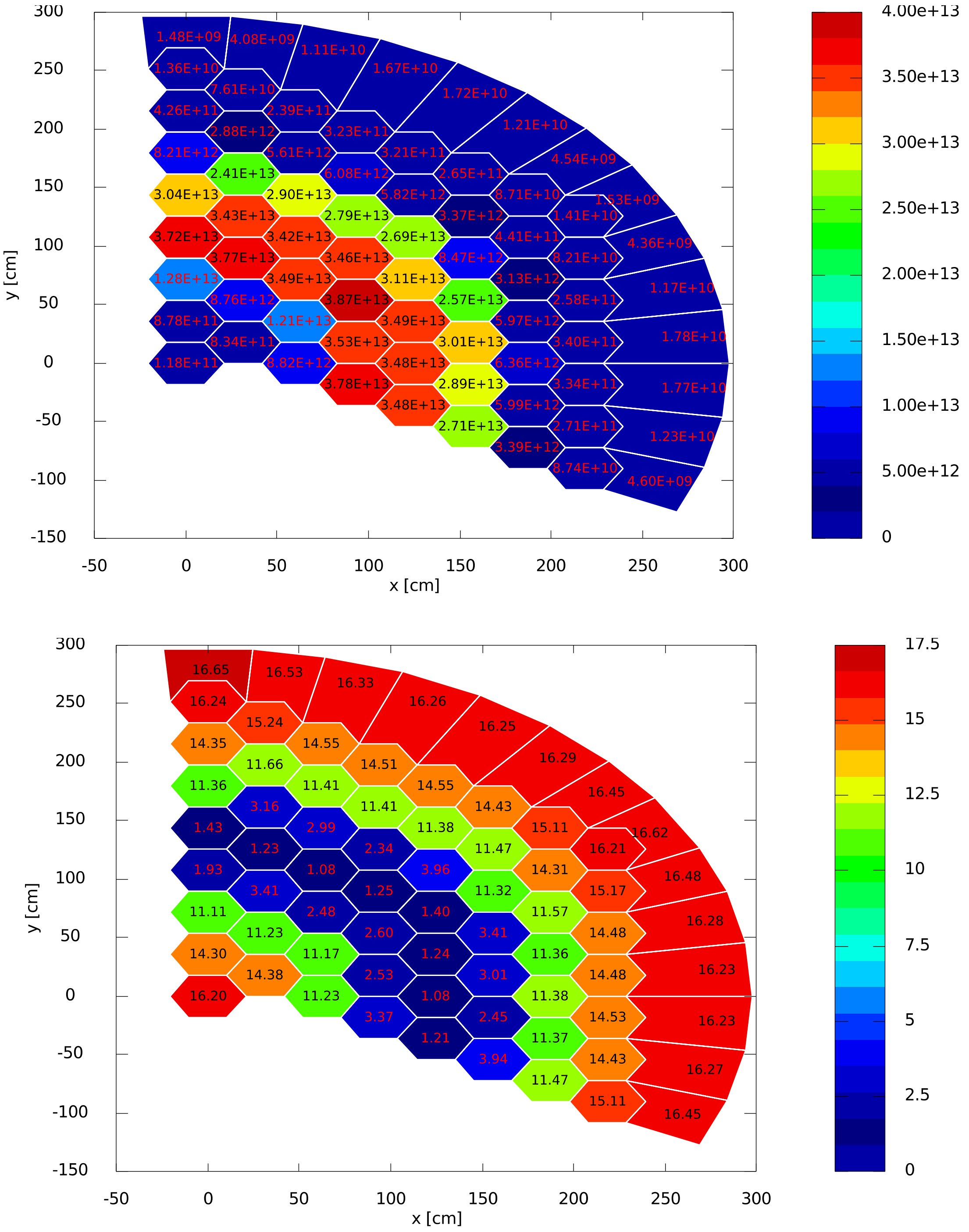

Source: OECD/NEA, 2020.

Figure B.6: Mean value and RSD for the axially averaged (active core region) fast flux–transport solutions

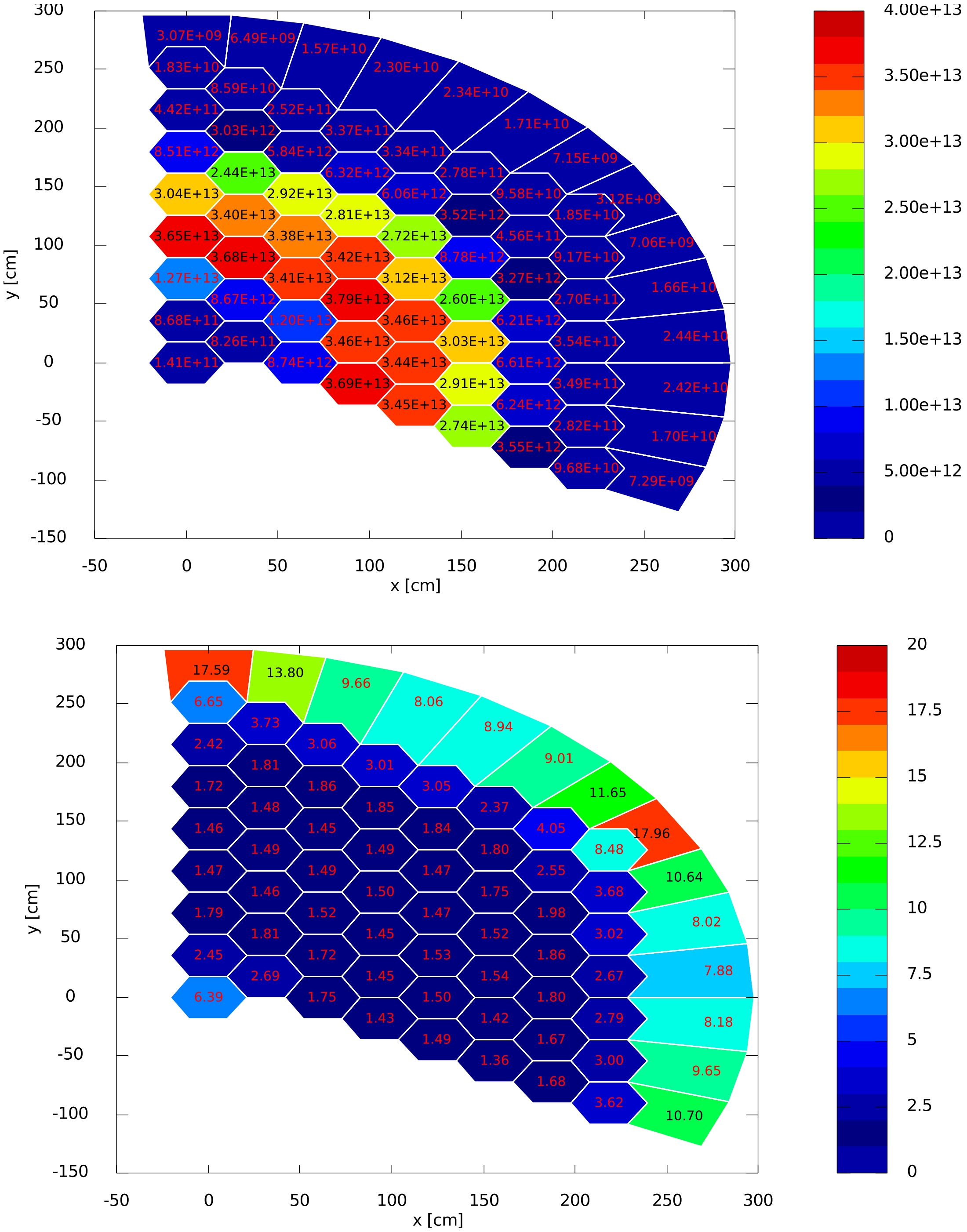

Source: OECD/NEA, 2020.

Figure B.7: Mean value and RSD for the axially averaged (active core region) epithermal flux−diffusion solutions

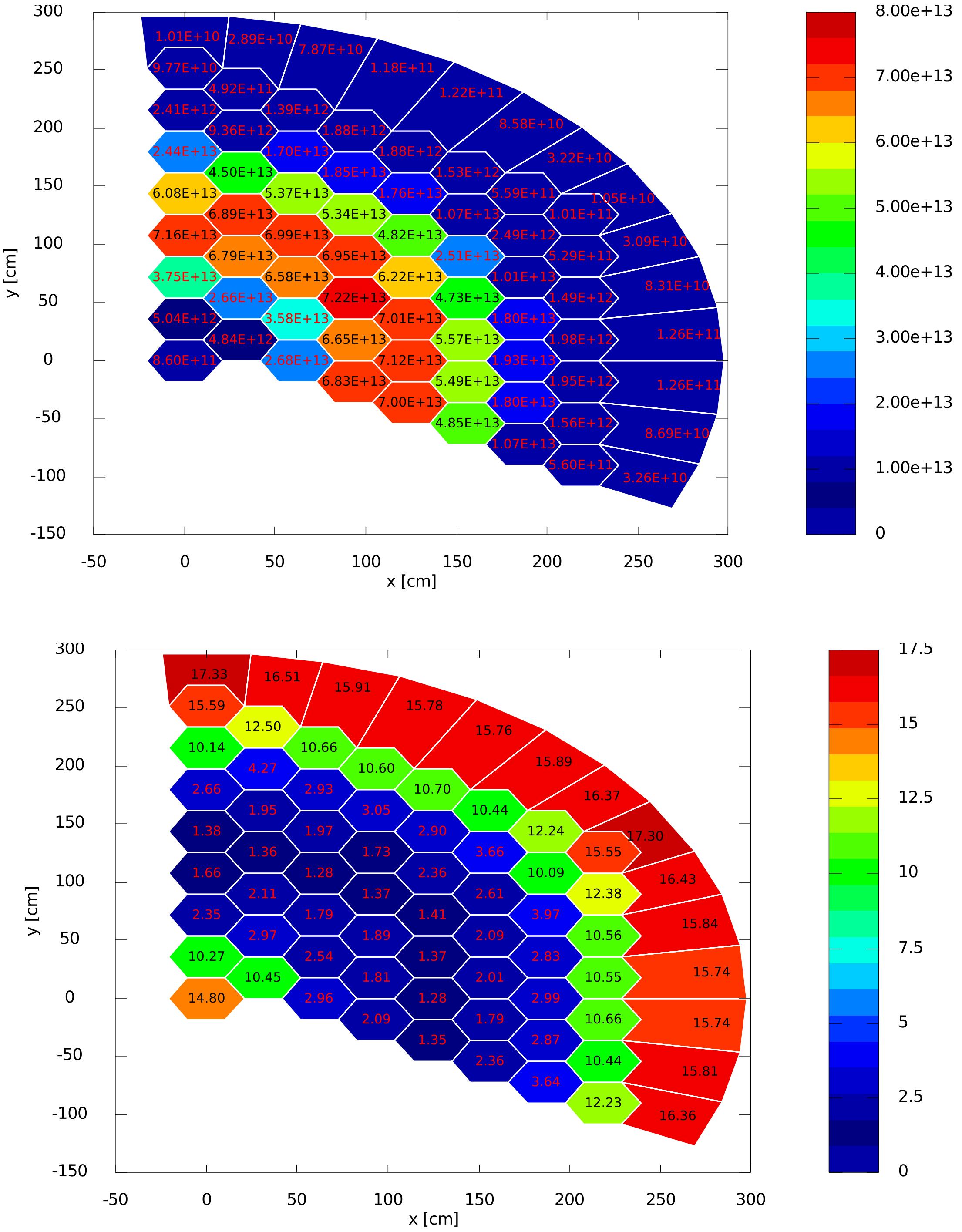

Source: OECD/NEA, 2020.

Figure B.8: Mean value and RSD for the axially averaged (active core region) epithermal flux–transport solutions

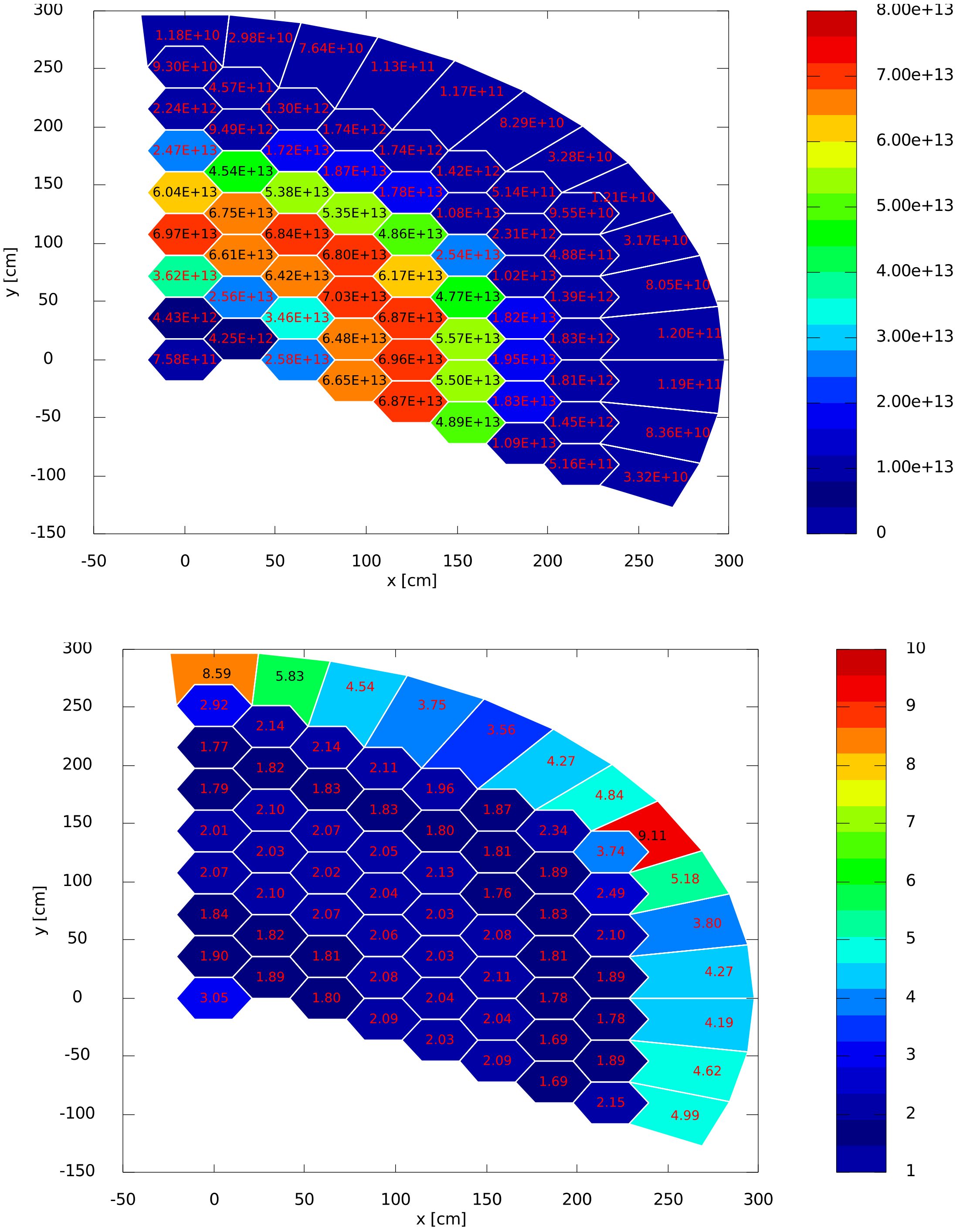

Source: OECD/NEA, 2020.

Figure B.9: Mean value and RSD for the axially averaged (active core region) thermal flux−diffusion solutions

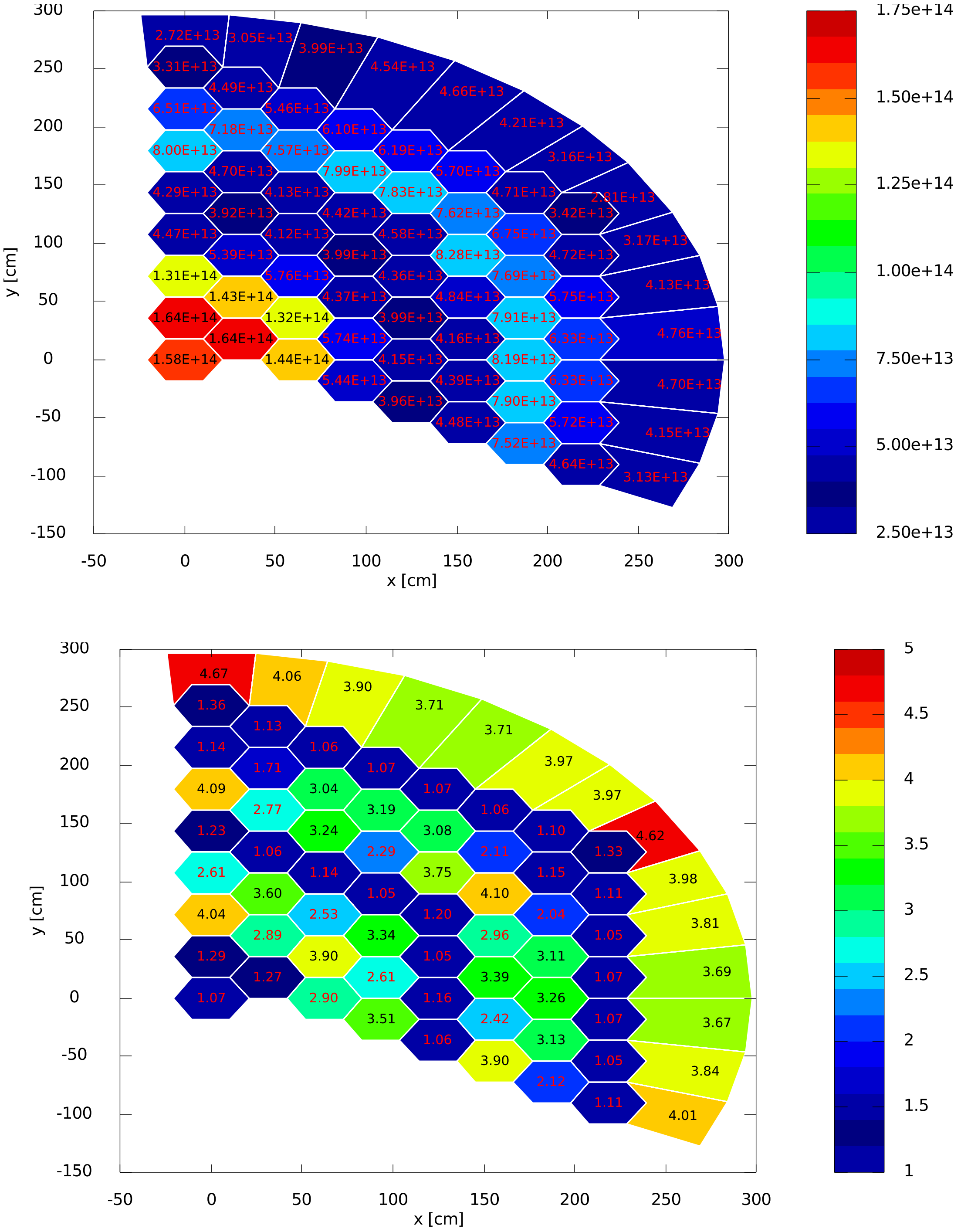

Source: OECD/NEA, 2020.

Figure B.10: Mean value and RSD for the axially averaged (active core region) thermal flux–transport solutions

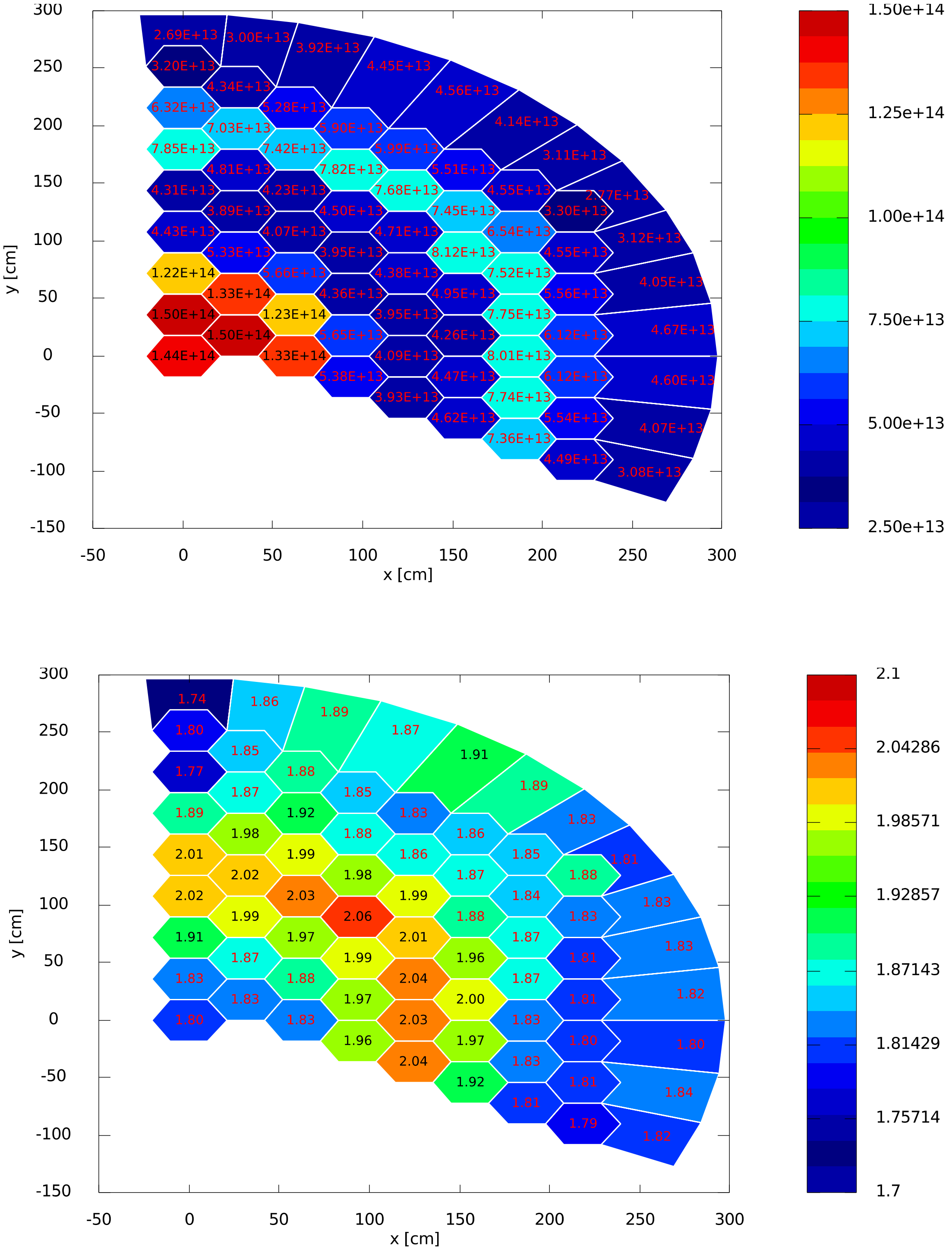

Source: OECD/NEA, 2020.

Annex C: Supporting plots for comparisons of the homogenised control rod

Figure C.1: CR homogenisation effect on the fast flux distribution at various axial levels (per cent difference with one-sixth as reference)

z = 8.12 m

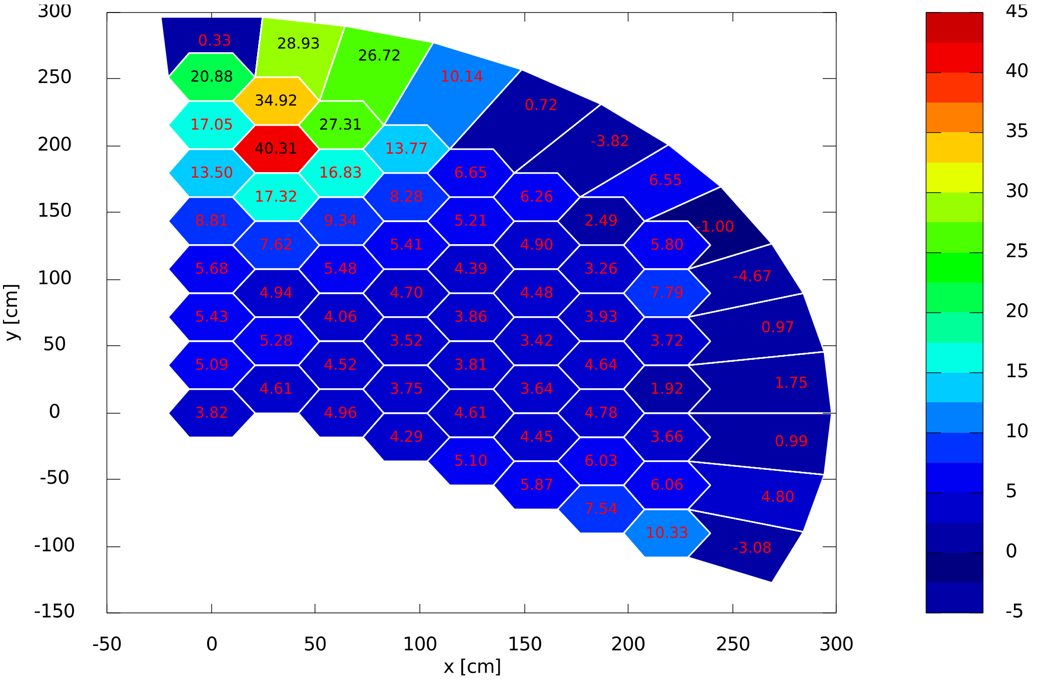

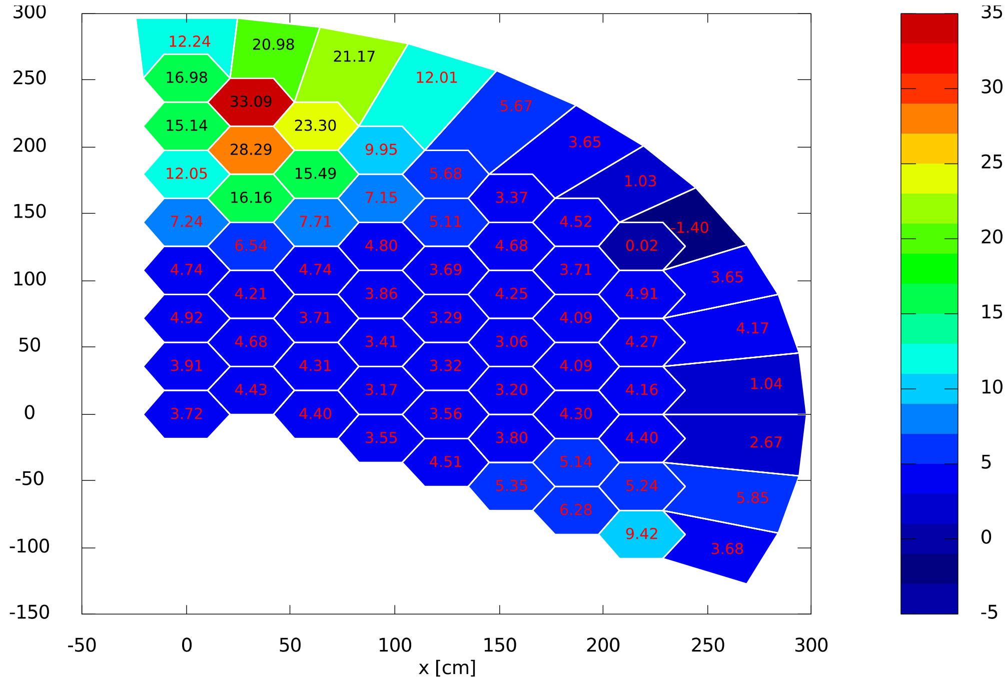
z = 7.53 m

300
250
200
150
100
50
0
-50
-100
-150
y [cm]
-50
0
50
100
150
200
250
300
x [cm]
35
30
25
20
15
10
5
0
-5
12.24
20.98
21.17
16.98
12.01
33.09
5.67
15.14
23.30
3.65
28.29
9.95
12.05
15.49
5.68
1.03
16.16
7.15
3.37
7.24
7.71
5.11
4.52
-1.40
6.54
4.80
4.68
0.02
4.74
4.74
3.69
3.71
3.65
4.21
3.86
4.25
4.91
4.92
3.71
3.29
4.09
4.17
4.68
3.41
3.06
4.27
3.91
4.31
3.32
4.09
1.04
4.43
3.17
3.20
4.16
3.72
4.40
3.56
4.30
3.55
3.80
4.40
2.67
4.51
5.14
5.35
5.24
5.85
6.28
9.42
3.68

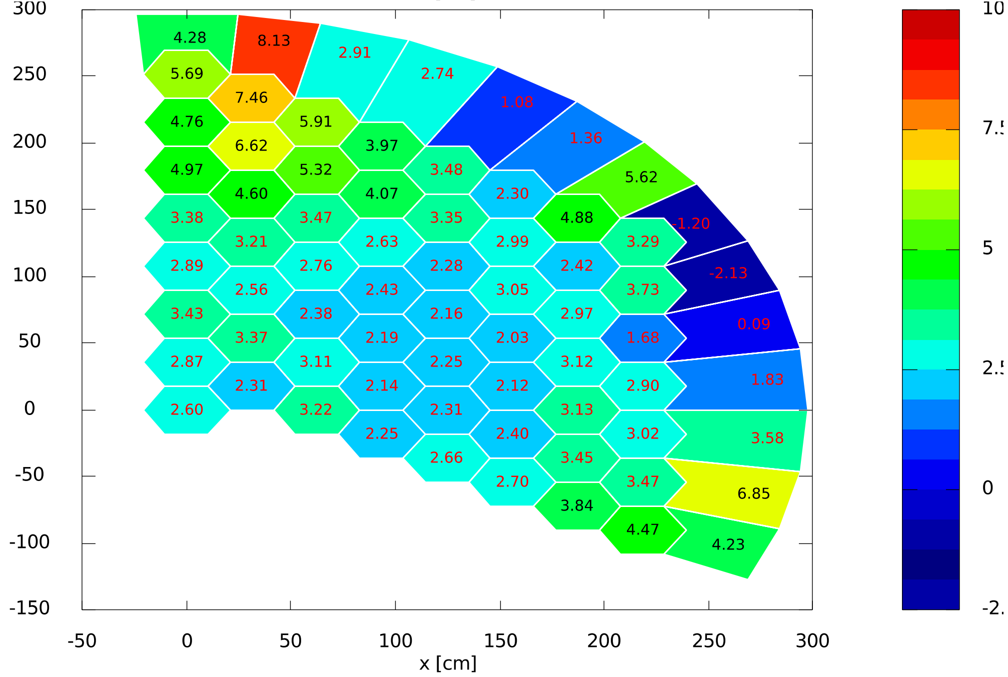
z = 6.74 m

300
250
200
150
100
50
0
-50
-100
-150
y [cm]
-50
0
50
100
150
200
250
300
x [cm]
10
7.
5
2.
0
-2.
4.28
8.13
2.91
5.69
2.74
7.46
1.08
4.76
5.91
1.36
6.62
3.97
4.97
5.32
3.48
5.62
4.60
4.07
2.30
3.38
3.47
3.35
4.88
-1.20
3.21
2.63
2.99
3.29
2.89
2.76
2.28
2.42
-2.13
2.56
2.43
3.05
3.73
3.43
2.38
2.16
2.97
0.09
3.37
2.19
2.03
1.68
2.87
3.11
2.25
3.12
1.83
2.31
2.14
2.12
2.90
2.60
3.22
2.31
3.13
2.25
2.40
3.02
3.58
2.66
3.45
2.70
3.47
6.85
3.84
4.47
4.23

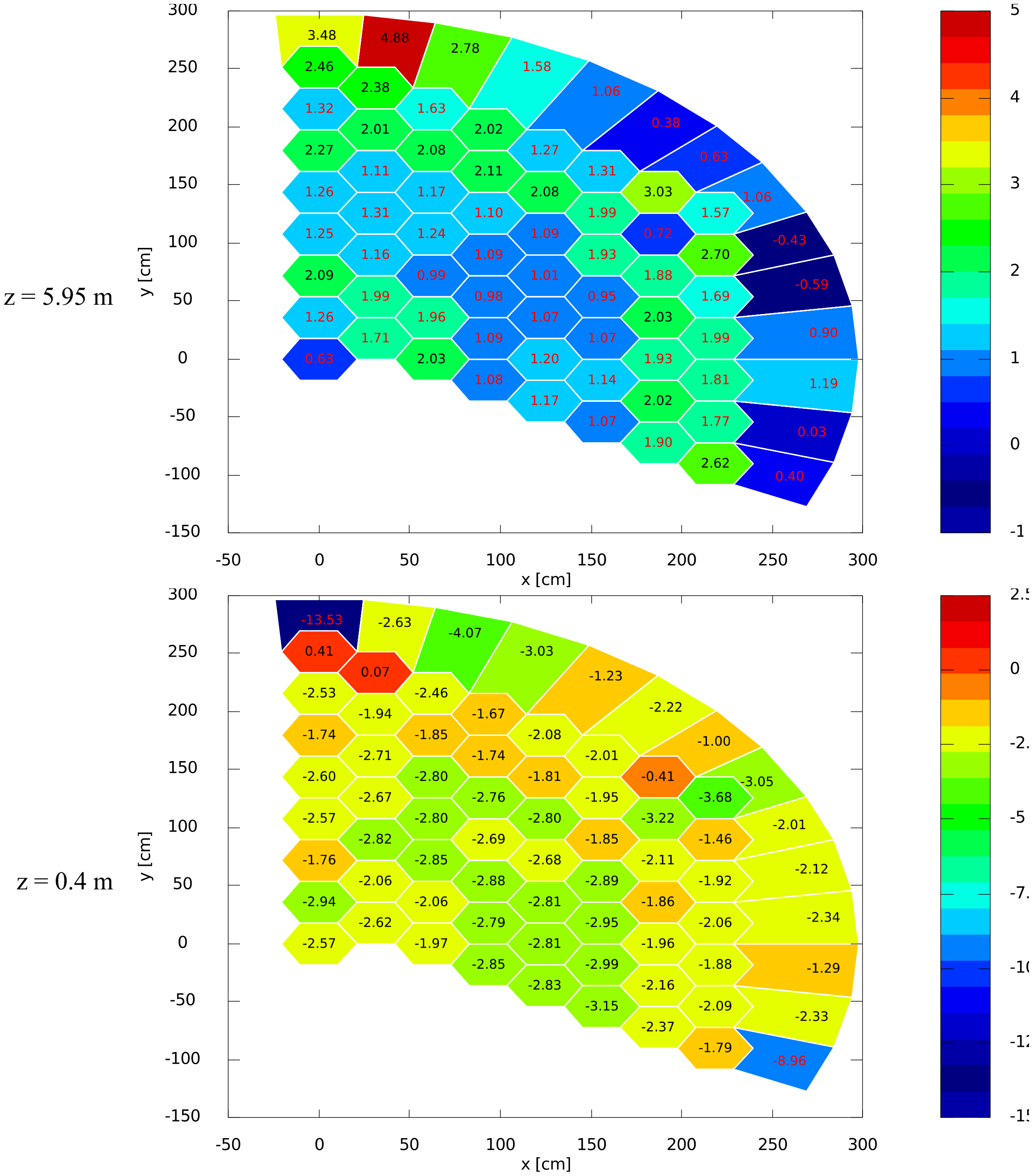

Source: OECD/NEA, 2020.

Figure C.2: CR homogenisation effect on the epithermal flux distribution at various axial levels (per cent difference with one-sixth as reference)

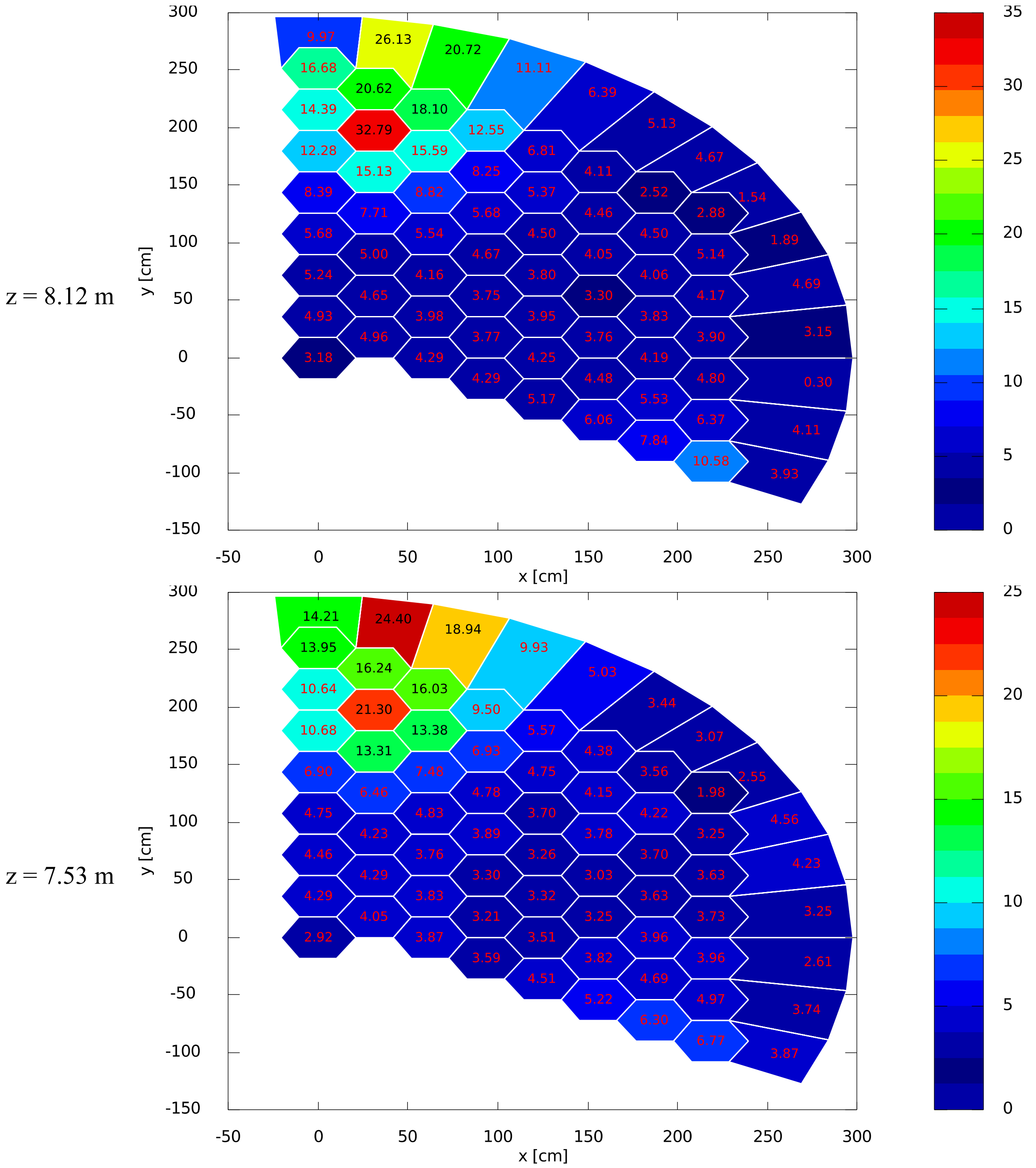

z = 6.74 m

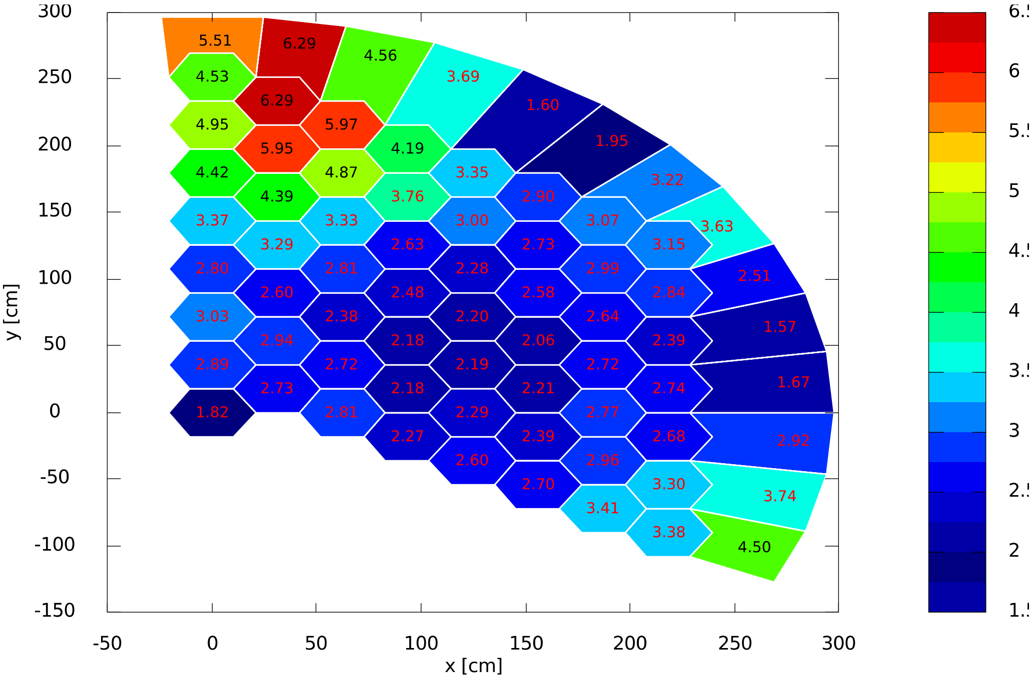
5.51
6.29
4.56
4.53
3.69
6.29
1.60
4.95
5.97
1.95
5.95
4.19
4.42
4.87
3.35
3.22
4.39
3.76
2.90
3.37
3.33
3.00
3.07
3.63
3.29
2.63
2.73
3.15
2.80
2.81
2.28
2.99
2.51
2.60
2.48
2.58
2.84
3.03
2.38
2.20
2.64
1.57
2.94
2.18
2.06
2.39
2.89
2.72
2.19
2.72
1.67
2.73
2.18
2.21
2.74
1.82
2.81
2.29
2.77
2.27
2.39
2.68
2.92
2.60
2.96
2.70
3.30
3.74
3.41
3.38
4.50
y [cm]
300
250
200
150
100
50
0
-50
-100
-150
-50
0
50
100
150
200
250
300
x [cm]
6.
6
5.
5
4.
4
3.
3
2.
2
1.

z = 5.95 m

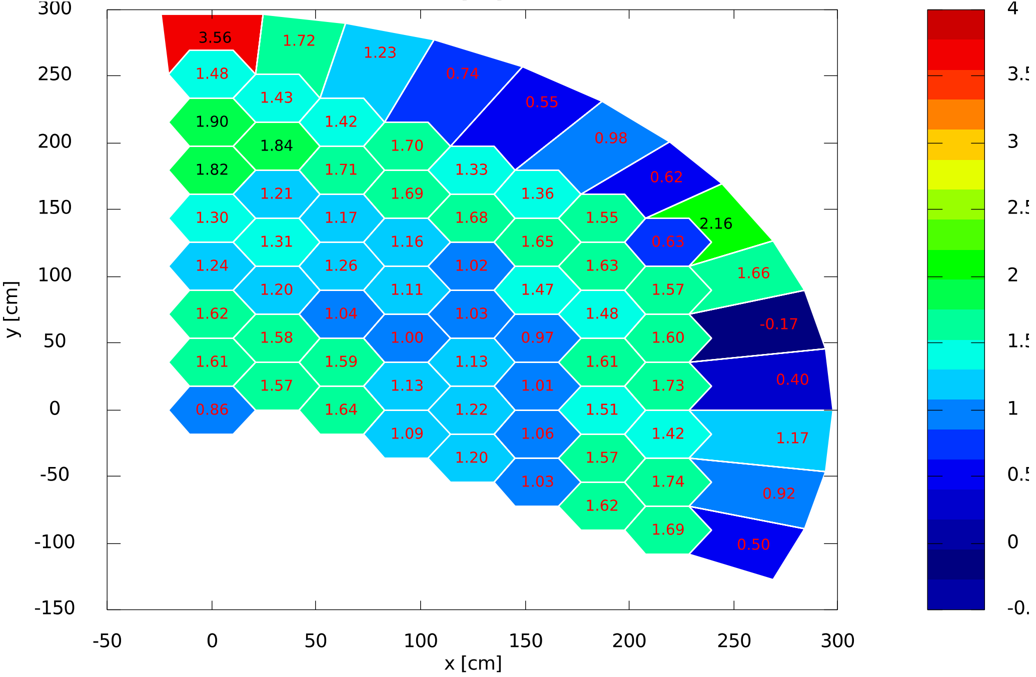
3.56
1.72
1.23
0.74
1.48
0.55
1.43
1.90
1.42
0.98
1.84
1.70
1.82
1.71
1.33
0.62
1.21
1.69
1.36
1.30
1.17
1.68
1.55
2.16
1.31
1.16
1.65
0.63
1.24
1.26
1.02
1.63
1.66
1.20
1.11
1.47
1.57
1.62
1.04
1.03
1.48
-0.17
1.58
1.00
0.97
1.60
1.61
1.59
1.13
1.61
0.40
1.57
1.13
1.01
1.73
0.86
1.64
1.22
1.51
1.42
1.17
1.09
1.06
1.20
1.57
1.03
1.74
0.92
1.62
1.69
0.50
y [cm]
300
250
200
150
100
50
0
-50
-100
-150
-50
0
50
100
150
200
250
300
x [cm]
4
3.
3
2.
2
1.
1
0.
0
-0.

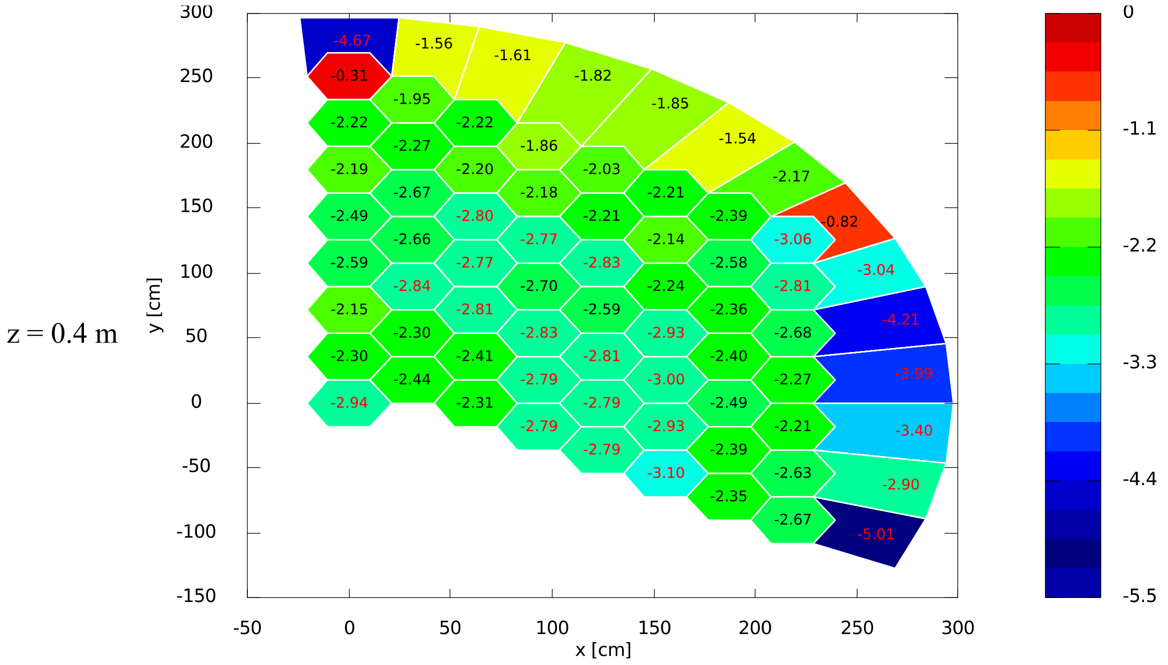

Source: OECD/NEA, 2020.

Figure C.3: CR homogenisation effect on the thermal flux distribution at various axial levels (per cent difference with one-sixth as reference)

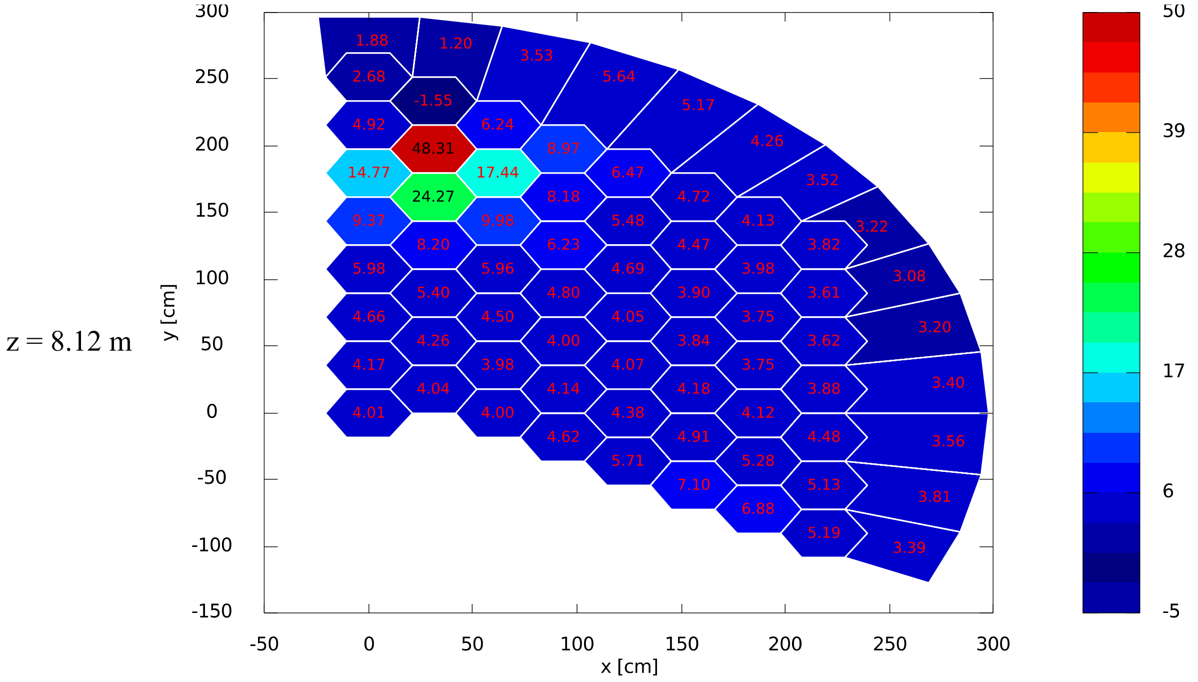

z = 7.53 m

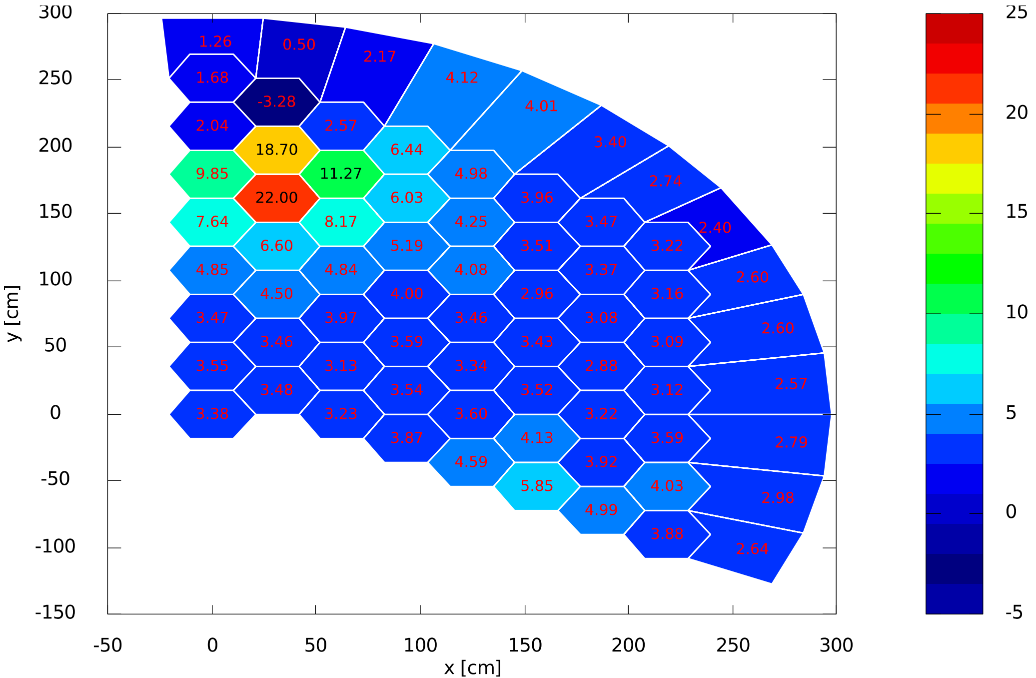
300
250
200
150
100
50
0
-50
-100
-150
y [cm]
-50
0
50
100
150
200
250
300
x [cm]
25
20
15
10
5
0
-5
1.26
0.50
2.17
1.68
4.12
-3.28
4.01
2.04
2.57
3.40
18.70
6.44
9.85
11.27
4.98
2.74
22.00
6.03
3.96
7.64
8.17
4.25
3.47
2.40
6.60
5.19
3.51
3.22
4.85
4.84
4.08
3.37
2.60
4.50
4.00
2.96
3.16
3.47
3.97
3.46
3.08
2.60
3.46
3.59
3.43
3.09
3.55
3.13
3.34
2.88
2.57
3.48
3.54
3.52
3.12
3.38
3.23
3.60
3.22
3.87
4.13
3.59
2.79
4.59
3.92
5.85
4.03
2.98
4.99
3.88
2.64

z = 6.74 m

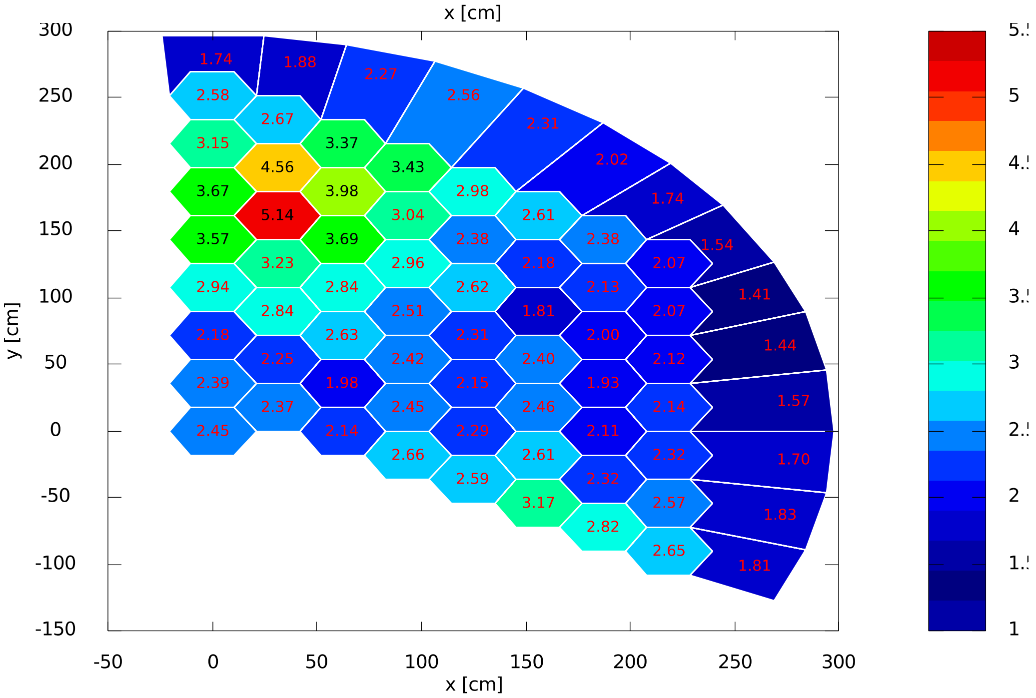
300
250
200
150
100
50
0
-50
-100
-150
y [cm]
-50
0
50
100
150
200
250
300
x [cm]
5.
5
4.
4
3.
3
2.
2
1.
1
1.74
1.88
2.27
2.58
2.56
2.67
2.31
3.15
3.37
4.56
3.43
2.02
3.67
3.98
2.98
5.14
3.04
2.61
1.74
3.57
3.69
2.38
2.38
1.54
3.23
2.96
2.18
2.07
2.94
2.84
2.62
2.13
1.41
2.84
2.51
1.81
2.07
2.18
2.63
2.31
2.00
1.44
2.25
2.42
2.40
2.12
2.39
1.98
2.15
1.93
1.57
2.37
2.45
2.46
2.14
2.45
2.14
2.29
2.11
2.66
2.61
2.32
1.70
2.59
2.32
3.17
2.57
1.83
2.82
2.65
1.81

z = 5.95 m

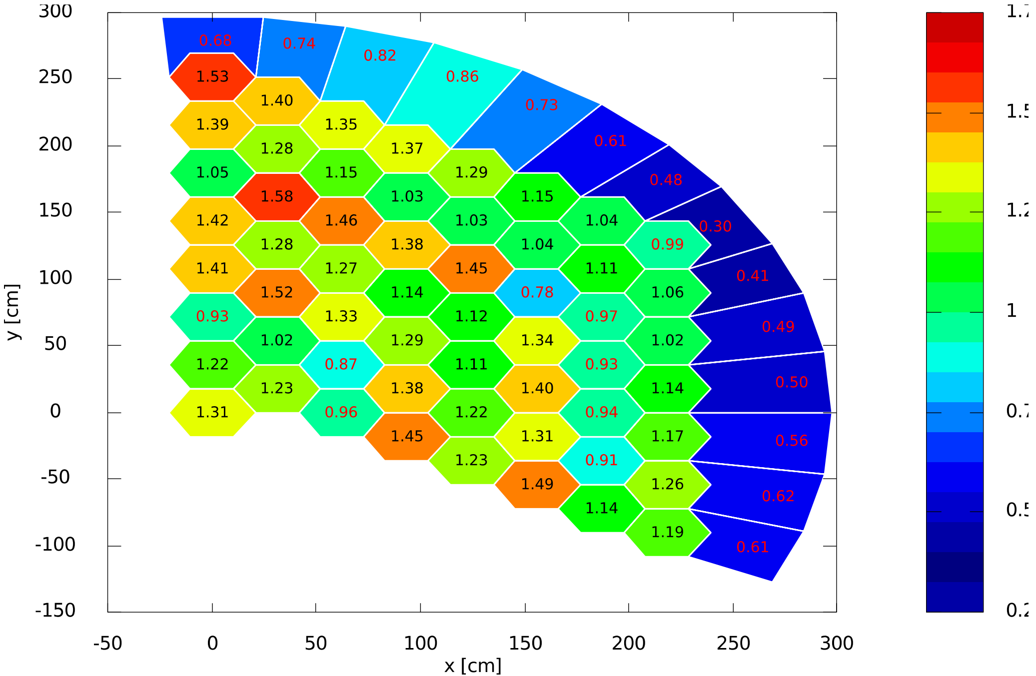

z = 0.4 m

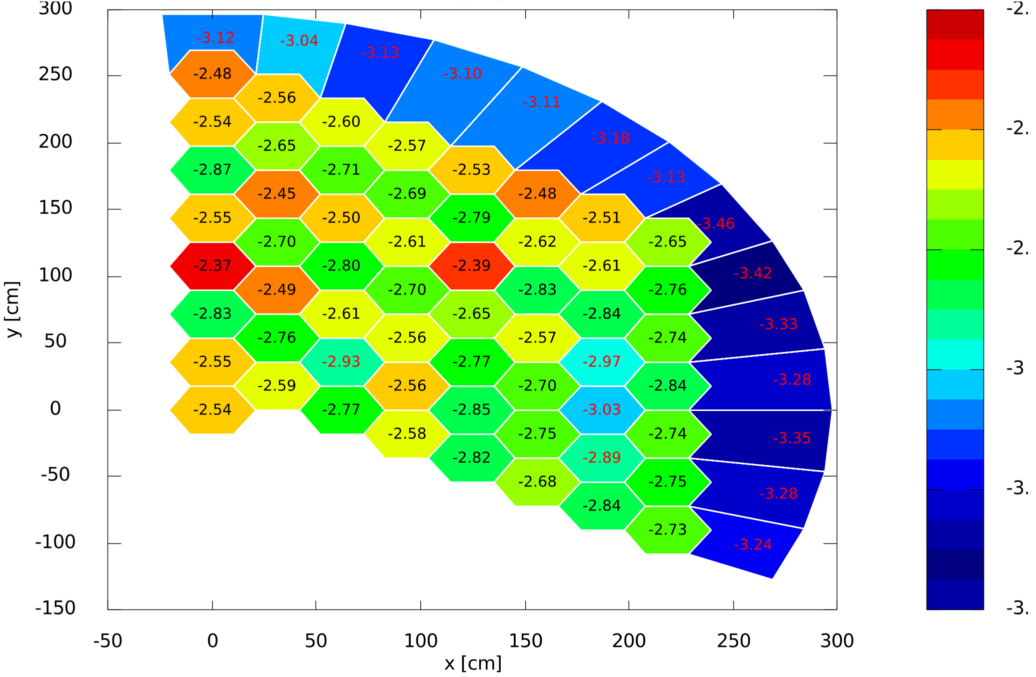

Source: OECD/NEA, 2020.

Annex D: List of participants

1. **Idaho National Laboratory (INL), United States**
   Participant: Javier Ortensi
   Code(s): Rattlesnake, INSTANT

2. **University of Michigan (UMICH), United States**
   Participant: Volkan Seker
   Code(s): PARCS

3. **Korea Atomic Energy Research Institute (KAERI), Korea**
   Participant: Hyun Chul Lee
   Code(s): CAPP

4. **Seoul National University (SNU), Korea**
   Participant: Hyung Jin Shim
   Code(s): McCARD

5. **Ulsan National Institute of Science and Technology (UNIST), Korea**
   Participant: Deokjung Lee
   Code(s): MCS

6. **Gesellschaft für Anlagen- und Reaktorsicherheit (GRS), Germany**
   Participant: Armin Seubert
   Code(s): PARCS, DIF3D

7. **Helmholtz-Zentrum Dresden-Rossendorf (HZDR), Germany**
   Participants: Yurii Bilodid, Emil Fridman
   Code(s): DYN3D